DOCTOR OF PHILOSOPHY

Development of strongly nonlinear shallow-water two-layer models for the numerical simulation of aluminium reduction cells

Politis, Gerasimos

Award date:
2020

Awarding institution:
Coventry University

Coventry University

Doctoral Thesis

Development of strongly nonlinear shallow-water two-layer models for the numerical simulation of aluminium reduction cells

---

Author:
Gerasimos Politis

Director of study:
Dr. Janis Priede

Supervisor:
Dr. Alex Pedcenko

A thesis submitted in fulfilment of the requirements for the degree of Doctor of Philosophy

in the

Faculty of Engineering, Environment and Computing,
Coventry University

28th September 2020

Content removed on data protection grounds

Certificate of Ethical Approval

Applicant:

Gerasimos Politis

Project Title:

Development of strongly nonlinear two-layer shallow-water models for the numerical simulation of aluminium reduction cells.

This is to certify that the above named applicant has completed the Coventry University Ethical Approval process and their project has been confirmed and approved as Low Risk

Date of approval:

22 November 2019

Project Reference Number:

P97926

Abstract

The present work is concerned with the numerical modelling of large-amplitude interfacial waves produced by metal pad roll instability in the aluminium reduction cells. A semi-conservative two-layer shallow-water model containing a novel, fully non-linear equation for electric potential is developed and solved using an original finite difference scheme. The latter is based on the two-dimensional Lax-Wendroff-Richtmyer scheme, which is adopted and extended to the two-layer system containing interfacial pressure. Two-dimensional Poisson-type equations for pressure and electric potential are solved using an original highly-efficient algorithm based on the combination of the tridiagonal matrix factorisation (Thomas algorithm) and the fast discrete cosine transform.

The development of the model and numerical schemes is started by considering purely hydrodynamic one-dimensional two-layer system and various conservative forms of shallow-water equations describing conservation of circulation or momentum in addition to that of mass. Using the method of characteristics, a novel analytical solution is found to the so-called lock-exchange problem. This exact solution is used to validate the ability of various numerical schemes to handle hydraulic shocks which are expected to develop in the shallow-water approximation. The one-dimensional solution is further used to validate two-dimensional numerical code by considering one-dimensional initial interface perturbations along two perpendicular sides of the rectangular container.

In addition, linear stability analysis of various basic models of aluminium reduction cells is revisited and extended to rectangular geometries. Linear stability analysis shows that in the case of negligible viscous friction, the cells with aspect ratios squared equal to the ratio of two odd numbers are inherently unstable and can be destabilised by arbitrary weak electromagnetic effect. The growth rates of small-amplitude electromagnetically destabilised interfacial waves produced by the numerical simulation agree very well with the linear stability results. Numerical results show that the growth rate decreases as the amplitude of unstable rolling interfacial disturbance grows with the time. A large-amplitude quasi-equilibrium state is reached without the interface touching the upper electrode. In this strongly nonlinear stage, the wave amplitude still keeps growing, however the growth rate is much slower than during the linear instability stage. At the same time, the nonlinear streaming effect produced by the large-amplitude rotating interfacial wave induces a global counter-circulation in the top and bottom layers. Numerical results indicate that the increase of the shear velocity above the critical value results in the Kelvin-Helmholtz type of instability which eventually causes the interface to break down.

Acknowledgements

Foremost, I would like to express my sincere gratitude to my director of studies Dr. Janis Priede for the continuous support of my study and research, for his patience, motivation, enthusiasm, and immense knowledge. His guidance helped me in all the time of study and writing of this thesis. I would also like to thank my second advisor Dr. Alex Pedcenko for his continuous support and motivation throughout my PhD. In addition, I wish to acknowledge the contribution of Dr. Sergei Molokov for setting the research problem and supervising me over a significant period of my PhD studies.

My gratitude also goes to Anthony Rouquier for proofreading my thesis and the invaluable discussions on physics and computational techniques. I had the chance to work with lovely people from Coventry with whom I discussed physics and all other matters of the world during all these years. I would like to thank my PhD fellows from Coventry who were supportive all the time: Sanjay Singh, Ravinder Kumar, Petro Sarkanyach, Argyro Mainou and Michail Akritidis. I am especially grateful for the continuous encouragement and support to my partner Vasiliki Georgopoulou without whom it would not have been possible to complete this work. I am also thankful to my parents Vasilis Politis and Natalia Marolla for supporting me during my PhD.

Contents

List of Figures

Introduction

The process of aluminium reduction consists of two superimposed layers of electrically conducting fluids. Through these layers of aluminium and cryolite, an intense electric current is supplied from the anodes, dissolving the alumina in the bath of molten cryolite by means of Joule-heating, before exiting from the cathode. This method of reducing aluminium was discovered independently by Charles Hall and Paul L.T. Héroult in 1886 when they revolutionised commercial production of aluminium with the electrolytic process of reducing alumina which little has changed till today. Typical sizes for the cells of aluminium reduction are 4-5m by 10-16m each, while the thicknesses of aluminium and cryolite are approximately 20-30cm and 4-5cm (Davidson, 2000). A historical overview in the development of the aluminium reduction Hall-Héroult cells (HHCs) can be found in Davidson (2001) and Batchelor et al. (2000), while detailed discussion of the electrochemical and material processing is carried out in Grjotheim and Kvande (1993) . The time-efficiency as well as monetary implications associated with improving the process are discussed in Davidson (2000) and Grjotheim and Kvande (1993), and it is highlighted that in this multi-billion industry, which consumes 2% of the electricity generated worldwide, any improvement would lead to immense economic benefits.

In order to reduce the electric energy consumption owing to Ohmic heating of the cryolite, which is of much poorer conductivity than aluminium, the reduction of its thickness is desired. The efficiency of aluminium reduction relies upon the controlled Magneto-Hydro-Dynamic (MHD) interaction of interfacial waves with the electromagnetic field. The development of interface instabilities may disrupt the process if either the cryolite's thickness or the supplied current are not carefully adjusted.

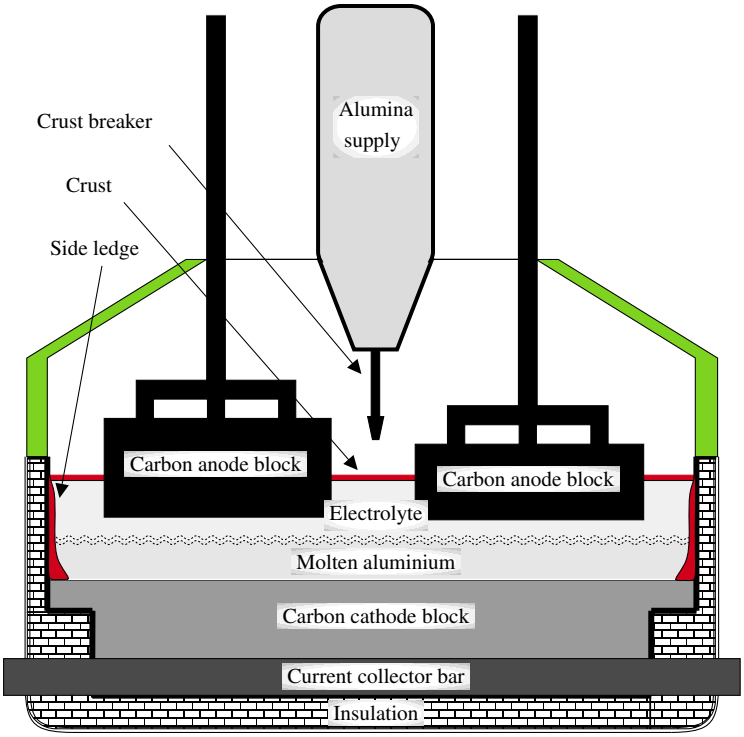

FIGURE 1: Schematic representation of Hall-Héroult cells.

Linear stability analysis (Bojarevics and Romerio, 1994; Sneyd and Wang, 1994; Lukyanov et al., 2001) is capable of detecting growth mechanisms and identifying dominant disturbances, however, investigation of nonlinear effects once a cell has become unstable may still provide insight of stabilising mechanisms and the manner by which the cell fails. Nonlinear models have been investigated by Zikanov et al. (2000), Sun et al. (2004) and Bojarevics and Pericleous (2008) which, owing to the shallow-water approximation, present a fast and efficient method for modelling the underlying mechanisms.

In recent years the ever increasing energy storage requirements, as a result of the rapidly developing renewable energy technologies, resprung and intensified the study of liquid-metal-batteries (LMB) which consist of two stably stratified liquid metals separated by a layer of molten salt. The nonlinear evolution of the rotational interfacial motion which has been, in the context of HHCs, identified as the primary source of instability is nevertheless, applicable in LMBs. Alas, due to the increased complexity of the system, large scale commercial applications are still not viable as further investigation is required. An extensive review of literature associated with LMBs is given in (Weier et al., 2017; Weber et al., 2017; Horstmann et al., 2018; Herreman et al., 2019).

This dissertation aims to develop a strongly non-linear 2D MHD model for

the numerical investigation of interfacial instabilities that arise in two layer flows, with a rigid lid, under the influence of an electromagnetic field. In order to tackle this problem a series of steps were required which are described in the succeeding paragraphs.

In the shallow-water approximation the waves are known to develop sharp fronts over time. To this end, a benchmark was required in order to test the effectiveness of the numerical scheme as well as a suitable set of equations capable of accurately encapsulating strongly non-linear motion. The 1D two-layer shallow water model was analytically solved under the approximation of small density difference, for the lock-exchange problem, and thus, offering valuable insight into the interfacial motion in the presence of an initially discontinuous interface. The analytic results were in turn contrasted with the numerical results obtained using the 1D Lax-Wendroff scheme which proved adept in accurately simulating the dynamics of motion in the vicinity of a discontinuous interface.

The numerical investigation of the 2D two-layer system bounded by a rigid lid compelled the construction of an efficient Poisson solver for the electric potential and pressure equations. Employing a combination of discrete cosine transforms and tridiagonal matrix algorithms, a new fast and accurate solver was developed. For the numerical integration of the shallow-water equations, an efficient 2D Lax-Wendroff scheme was developed, chosen for its second order accuracy in space and time as well as its low dispersion.

The Lorentz force arising as part of the MHD problem requires the solution of the Poisson equation for the electric potential. A novel fully non-linear 2D equation was derived for the electric potential. Furthermore, the linear stability analysis of the MHD problem elucidated the dependence of stability on the aspect ratios of rectangular cells.

This dissertation is organised as follows. In §1 a literature review covering the three main topical areas is presented. Namely, the magnetohydrodynamics of liquid metals, the shallow-water theory and numerical methods. In §2 an overview of the basic theoretical concepts underlying this work are presented, with the main focus on the fundamental principles pertaining to hydrodynamics, shallow-water (SW) approximation and electromagnetics (EM). In §2.6 the single-layer shallow-water equations are presented. These are extended to two layers, in §2.7, with a 2D nonlinear equation accounting for the interfacial pressure and electric potential. The relevant parameters used in the nondimensionalisation of these equations are also discussed therein. The simplifying assumptions for

aluminium reduction cells are presented in §2.5 where also a fully nonlinear 2D equation for the electric potential was derived.

The linear stability analysis of electromagnetically modified interfacial waves is carried out in §6, where models with increasing geometrical complexity are considered. Results of the half plane and the channel geometries are revisited before proceeding to the rectangular geometry where the stability threshold depending on the aspect ratio of rectangular cells is analysed.

In §2.9 the 1D Lax-Wendroff scheme has been presented, while its 2D extension by Richtmyer is further described in §3.1. The latter is used to develop a new modified scheme which utilises the finite volume formulation on the staggered rhombic grids, thus eliminating the uncoupled part of the solution present in the original scheme. Furthermore, a new highly-efficient Poisson solver is developed, combining the discrete cosine transforms and the tridiagonal matrix Thomas algorithm.

A two-layer 1D model is considered in §4 with the use of a conservative set of equations. The lock-exchange problem with strong interfacial discontinuities is solved analytically in the Boussinesq approximation. The analytical solution is then used to validate the 1D Lax-Wendroff scheme which is found to be in excellent agreement with the former.

In §7 the efficiency of the two-layer hydrodynamic 1D Lax-Wendroff scheme is further examined for smooth initial states and compared with the results produced by the 2D scheme for the analogous cases. The chapter is concluded with the presentation of the two-layer magnetohydrodynamic results, obtained with the 2D scheme, where a discussion of the instabilities leading to the break down of interface is presented.

Chapter 1

Literature review

In this chapter an overview of research developments on the three main topical areas of this thesis are presented, starting with a historical background development of the liquid metal MHD in §1.1. This is followed by the discussion on research pertaining to the lock-exchange problem §1.2 before concluding to a review of schemes for hyperbolic problems in §1.3.

1.1 MHD part of the problem

The field of magnetohydrodynamics spans from thermonuclear fusion and plasma astrophysics to industrial applications. Extensive work has been carried out in the study of fluids under the influence of an electromagnetic field with particular interest in industrial applications; thus giving rise to the field of liquid-metal MHD where the theory pertaining hydrodynamics as well as electrodynamics is exploited with tangible ecological and economic benefits when the consumption of energy and consumable materials is reduced. The incipience of liquid-metal MHD sprang from the benefits found in controlling the liquid metal flow by means of the Lorentz force, with major applications onto metallurgical industries and in specific liquid metal reduction cells.

One of the earliest papers on the instability mechanism in aluminium reduction cells is by Sele (1977) where the transient waves are numerically explored with emphasis on the geometry of the cell and the strength of the electromagnetic interaction. The model is used to determine the stationary flow and interface shape in the electrolytic cells subject to constant magnetic field. The general characteristics of aluminium reduction cells are analysed along with the rolling-pad instability mechanism and the complications that this process is associated with. Additionally, a stability criterion resulting from scaling considerations is

verified against the numerical results. This key nondimensional parameter, commonly referred to as the Sele parameter, is discussed further in §2.7.3 and it is widely used in the field.

Moreau and Evans (1984) introduce simplifications based on physical criteria such as the permeability and the electrical conductivity, along with the shallow-water approximation which is based on the assumption of small depth-to-length ratio. These considerations lead to the approximation of small magnetic Reynolds number which holds because the magnetic diffusion time through the cell is small compared to the characteristic hydrodynamic time scale. The electromagnetic force was examined to both first and second order of the shallowness parameter, where the latter was concluded to be insignificant. Although the two-layer fluid system concerns an ideal case, the analysis reveals dependence of the dynamics on the geometry of the anode channels and on the electric current distribution. The model of Moreau and Evans (1984) is extended by Moreau and Ziegler (1988) who model the effect of viscosity via a linear friction term using the same numerical scheme as Lympany et al. (1982). Moreau and Ziegler (1988) analyse the influence of the small channels between the anode blocks but do not find any significant effect. These papers are relevant to the present work mostly because of the shallow-water approximation, and the linear friction model introduced by Lympany et al. (1982). Lastly, based on the results of aforementioned papers, a flat rigid-lid is assumed on the top boundary where no spacing among the anode blocks is considered.

Sneyd (1985) considers a very basic aluminium reduction cell model by making a range of simplifying assumptions such as the uniform normal current, no fluid flow in the unperturbed state and no lateral boundaries. The magnetic field is assumed to be purely coplanar consisting of an induced and an external component. The former is generated by the electric current passing through the system and is found to be always stabilising, contributing to the gravitational restoring force. The far field component may give rise to unstable interfacial disturbances that grow exponentially in time. Special attention is drawn to the external electric currents which can affect the stability of interface by altering the magnetic field in the reduction cell. The discussion of the instability dependance on the wavelength and cryolite layer depth leads to the conclusion that only longer waves can be destabilised by MHD effects. In the analysis conducted by Moreau and Evans (1984), Sneyd (1985) as well as Moreau and Ziegler (1988), the effects of lateral boundaries were neglected, the importance of which however is later shown to be pivotal for the system's stability. The subsequent analysis of Sneyd (1992)

is extended to account for the horizontal current component, vertical magnetic field and vertical field gradients. The stabilising effect of gravity and surface tension on the Kelvin-Helmholtz instability are investigated. The contribution of the electromagnetic effects is found to be destabilising for wavelengths greater than one meter, with the main destabilising factors, dependent solely on the vertical component of the background current, being the vertical gradients of the horizontal magnetic field. Although, the current is assumed uniform, in reality the disturbance current may change direction depending on the direction of the horizontal currents. The effects of this convention are thought detrimental, as the main contributor to the instability is known to be the vertical component of the electric field which is constant. Moreover, the linear variation of the magnetic field –imposing a linear variation on the wave-induced flow– may have serious stability consequences as it affects the boundaries of the cell.

Sneyd and Wang (1994) analyse the instabilities at the interface of two-layers in a rectangular tank under the influence of a vertical uniform current and a linearly varying magnetic field in the plane transverse to the current. Similarly to Sele (1977) a stability parameter and an estimate of the stability threshold are derived. The perturbations under consideration are combinations of the normal gravity-wave modes. Unlike analyses which consider a channel, it is shown that the cell becomes more unstable as the external field increases with the most dangerous component being the vertical one. In the same train of thought, Bojarevics and Romerio (1994) provide a rigorously derived linearised system for the study of the interface instability of the fluid layers, through perturbation expansions in parameters of the depth aspect ratios, the maximum amplitude and the conductivities of the respective layers. A generalisation of the Sele parameter under the shallow-water approximation is derived, which demonstrates the importance of the aspect ratio in addition to the vertical component of the magnetic field. Later, Bojarevics (1998) extends the analysis by considering nonlinear waves with linear dissipation terms. The effect of the aspect ratio, of a rectangular cell, on the stability is further studied in §6.

Davidson and Lindsay (1998) point out the advantages of the explicit expression of the Lorentz forces versus the model developed by Urata (1985) where an implicit formulation is considered. In contrast to Sneyd (1985) and Moreau and Ziegler (1988), who considered travelling-wave instabilities in non-uniform magnetic fields, Sneyd and Wang (1994) and Davidson and Lindsay (1998) study the instabilities which can occur in a uniform magnetic field. For standing waves in a finite domain, an energy criterion is developed indicating that certain types

of motion such as a rotating, tilted interface, may gain energy. Their analysis shows that it is not necessarily the interaction of the closest gravitational modes which causes instability and that unstable modes can arise from merging of two stable eigenmodes. This is complemented by the fact that few modes interact but the uncoupled ones cannot become unstable. Lastly, for rectangular domains the results are confirmed to agree with the ones of Sneyd and Wang (1994), while for a circular domain a simple form of instability is found.

Lukyanov et al. (2001) investigate the basic mechanism of instability for the two-layer system under the influence of a uniform magnetic field. Linearised shallow-water equations are used as in the previous studies. The attention is focused at the effects of the wave reflection from the walls on the stability of two models: a plane wall and a circular domain. It is shown that with an increase of the interaction parameter, which controls the ratio of the electromagnetic (EM) to gravity forces, the interfacial stability is dictated by the wave reflection from the wall. The work of Lukyanov et al. (2001) is extended by Molokov et al. (2011) who consider the instability at high values of the electromagnetic interaction parameters, for different geometries. A distinction is made between unstable travelling waves localised at the wall modes and non-local Sele modes, which are gravity wave modes with the wavenumber spectrum modified by the electromagnetic reflection condition. The former are argued to be amplified by the MHD-modified reflection of waves from the side walls. The latter are stable or slowly growing.

Kurenkov et al. (2004) carry out a linear stability analysis of the interface in two-layer shallow water model in an infinite channel. The instability mechanisms considered are those of the Kelvin-Helmholtz and Sele. These mechanisms are initially analysed separately and then compared to the general case. Little interaction exists between those two destabilising mechanisms, with practically no effect on the stability threshold. The stability investigation is focused on its dependence on the width of the channel and the Sele parameter. Concerning the stability, it is found that narrow channels are more stable. The linear stability analysis of semi-infinite and channel geometries are reviewed in §6 before proceeding into the study of the rectangular geometry.

The interfacial stability of two liquids is investigated numerically by Zikanov et al. (2000) using a nonlinear 2D shallow-water model in a rectangular geometry. Assumptions used in this model are the same as those introduced by Sele (1977) and Urata (1985) and the reasoning for the electromagnetic force in the upper(cryolite) layer is based on the analysis of Davidson and Lindsay (1998).

It is found that the horizontal current perturbation plays a pivotal role in the stability. The background flow driven by the Lorentz force can lead to strong distortion of the interface. The authors highlight that in linear stability analysis, the eigenvalues describing interfacial wave instabilities are calculated by ignoring the stationary background flow which only afterwards is substituted into the analysis. Shortcomings of this approach lie on omitting nonlinear effects which may produce background flows. This eigenvalue analysis may be, computationally, costly. Lastly, the assumption of a time invariant basic state is always true. The main advantage of this model over linear stability analysis is due to the combination of the background flow and instability which permits nonlinear interface perturbation of large amplitude. Sun et al. (2004) expand the shallow-water model of Zikanov et al. (2000) to investigate the impact of the nonlinear terms omitted in the MHD models used by Bojarevics and Romerio (1994), Sneyd and Wang (1994) and Davidson and Lindsay (1998). The effect of the horizontal components of the magnetic field on the Lorentz force were found only significant in the destabilisation of the system when the system obtains large interface deformation and strong nonlinearities are involved which are further amplified by the Lorentz forces.

1.2 Hydrodynamic part of the problem

The development of a scheme for the simulation of a strongly nonlinear shallow-water model for two layers necessitated the investigation of conservation laws which are required in the presence of strong discontinuities. This led to a comprehensive review of the known theory pertaining to one- and two-layer shallow-water models, with particular interest into the topic of the two-layer lock-exchange (LE) problem. Cardinal publications that formed the fundamental basis for the theoretical analysis of single layer flows released from rest, when a wall is instantaneously released, can be found in Barré de Saint-Venant (1871) followed by the solution provided by Ritter (1892) which used the shallow-water approximation and the method of characteristics to study the gravity driven current over a horizontal or sloped ground. This classic solution, commonly known as the dam-break problem, which can be found in more detail in Courant and Friedrichs (1948), Stoker (1957), Whitham (1975) (and references therein), is an important example in the study of nonlinear flows reproduced in laboratory experiments and used as a benchmark in the development of schemes.

One of the inherent features of the shallow-water approximation is the unlimited steepening of the wave fronts. The single layer formulation of the shallow-water approximation and the analogous description in gas dynamics have been thoroughly discussed in Stoker (1957, Chapter 10). The evolution of steep fronts leads to breaking of the waves which are commonly referred to as hydraulic-jumps, bores or shocks. From a mathematical perspective, this is the behaviour under which the system of PDEs produces a discontinuous solution, thus ceases to be directly applicable. As highlighted in Whitham (1975), Stoker (1957), and LeVeque (2002, Chapter 1.1.2) the relevant physics represented by the relevant conservation laws can still be applicable to discontinuous solutions. These conservation laws are represented by the so-called Rankine-Hugoniot (RK) conditions which can describe the propagation of shocks. The direct relevance of this theory to a two-layer system as well as the necessity for appropriate conservation laws for its description will become evident in §4.

In single-layer shallow-water flows it has been shown by Benney (2006) and Miura (1974) that an infinite number of locally conserved quantities exist. The more complex problem of superimposed fluids, where a heavier fluid in a horizontal channel is initially separated by a vertical lock from a lighter fluid, has been extensively studied over the past century owing to its widespread use in oceanography, metereology and engineering applications (Yih, 1947; Long, 1954; Keulegan, 1957; Yih, 1965; Armi, 1986; Simpson and Britter, 1979; Klemp et al., 1994; Shin et al., 2004). In two-layer flows with an unbounded upper surface only six linearly independent local conservation laws exist (Ovsyannikov, 1979; Montgomery and Moodie, 2001; Barros, 2006). For two-layer system bounded by a rigid lid, the first rigorous derivation of shallow-water equations is due to Long (1956a) where a unified system with the use of the mass and circulation (vorticity) conservation is presented. The existence of an infinite number of locally conserved quantities in this system has been first noted by Ovsyannikov (1979). However, only the aforementioned two are generally known.

The primary conserved quantity that governs the dynamics of bores in single fluid layers is momentum. To our knowledge no analogue shallow-water conservation law is known for the case of a two-layer system. This has led to the consensus that such a system containing internal bores is inherently non-conservative (Abgrall and Karni, 2009), and external closure relations are required based upon dimensional arguments (Abbott, 1961) or derived using various semi-empirical and approximate integral models (Baines, 1995).

One of the earliest mathematical models of hydraulic jumps in two-layer system

is due to Yih and Guha (1955). In their analysis they used the momentum and mass conservation principle to link the flow states across the discontinuity. The system was reduced in to a set of ordinary differential equations that allowed the authors to identify the conjugate states connected by a discontinuity.

Long (1956a) is the first to derive the two-layer shallow-water equations under a rigid-lid by elimination of the longitudinal pressure gradient. Long (1956a) also obtains explicit expressions for Riemann invariants which can be used to solve certain initial problems for strongly nonlinear interfacial waves analytically. Such exact analytical solutions are useful for validating numerical algorithms. The paper investigates, with the method of characteristics, how the advancement of an interface elevation leads to the steepening of the waves, but does not consider how to tackle discontinuous solutions. For the same system, Ovsyannikov (1979) examines three different models: that of a free upper layer, the two-layer system bounded by a rigid-lid significant density difference and the limiting case of the two-layer model where the density of the two layers is almost equal. Similarly to Long (1956a) the Riemann invariants and the characteristic speed were utilised to establish the domain of hyperbolicity.

Benjamin (1968) applied hydraulic theory, based on the Bernoulli's equation, in a channel where an air-cavity flow displaces the heavier fluid at the bottom. The main result of this study on steady gravity currents is a front condition relating the velocity of propagation with the layer depth of the bottom which was compared with the experimental results of Keulegan (1957), Yih (1965). This is one of the classic hydraulic conditions which is widely used to describe gravity currents.

Rottman and Simpson (1983) utilise a unified two-layer model, similar to Long (1956a), where the front condition of Benjamin (1968) is incorporated in the region where the equations resulted in discontinuous solutions, which results in the current front being treated similarly to hydraulic jumps. This empirical front condition involved an adjustable parameter to be defined by experiments. This class of hydraulic-type models (Benjamin, 1968; Huppert and Simpson, 1980; Rottman and Simpson, 1983; Shin et al., 2004) and approximate ad-hoc solutions (Keller and Chyou, 1991; Lowe et al., 2005) have been commonly proposed for the lock-exchange problem where the thought absence of a momentum conservation law led to the chase of empirical or semi-empirical front conditions dependent on energy conservation considerations being preserved on the upper- (Klemp et al., 1994; Klemp et al., 1997), or lower-layer (Wood and Simpson, 1984; Huppert and Simpson, 1980). So far only a numerical solution of this problem has been

carried out by Klemp et al. (1994) using a characteristics-type approach suggested by Rottman and Simpson (1983). A more direct numerical solution of the lock exchange problem has been attempted by Ungarish (2009, Sec. 2.4) using a non-conservative form of two-layer shallow-water equations.

Milewski and Tabak (2015) use two-layer shallow-water conservation laws for circulation and energy, and a rather advanced finite-volume scheme for numerical modelling of the lock-exchange problem with entrainment. They also consider an analytical solution to the lock-exchange problem with the conservation of either mass or energy besides that of circulation. However, their approach differs from the standard simple-wave method (Whitham, 1975, Sec. 6.8) pursued in this study. Recently, the lock-exchange problem for Boussinesq fluids was solved numerically by Esler and Pearce (2011) using a higher-order weakly non-hydrostatic shallow-water approximation in which dispersion prevents the formation of sharp wave fronts.

1.3 Numerical schemes for hyperbolic problems

The dam-break problem has been thoroughly analysed theoretically and serves as a benchmark in the development of numerical schemes to validate one- and two-dimensional numerical models. An analytic methodology originating in the affiliated topic of gas dynamics is the Riemann problem, that permits the reduction of PDEs into a system of ODEs which offer similarity solutions. These consist of a finite set of wave solutions that propagate from the origin, with constant wave speeds (Godunov, 1959). The drawback of the numerical implementation developed in Godunov (1959), lies in the piecewise linear reconstruction that leads to strong diffusion. Being an exact solver, Godunov's scheme can be computationally expensive for nonlinear problems. Consequently, this lead to the development of numerical schemes which make use of approximate Riemann solvers.

The property of monotonicity, introduced by Godunov (1959), provides the means for the systematic analysis of the stability conditions for non-oscillatory behaviour required by schemes. This was further complemented by the criterion of Total-Variation-Non-Increasing (TVNI) (or Total-Variation-Diminishing (TVD)), solutions introduced by Harten (1983) and Harten (1984). This concept ensures that in the numerical solution of nonlinear equations, unwanted oscillations are not generated.

A large number of schemes have been developed in order to tackle the dam-break problem, aiming to encapsulate the rise of discontinuous solutions, whilst overcoming the strongly oscillatory behaviour that is encountered in the study of hyperbolic equations. Owing to the fact they are first-order accurate, the schemes detailed in Engquist and Osher (1981), where the direction of the flux is defined by the eigenvalue's sign, in Roe (1981), where an average from either side of the Riemann problem is used, or Harten (1983) which defines the maximum/minimum wave speeds arising in the Riemann solution, are usually not employed due to their inherent low accuracy.

Despite the necessity of a monotone scheme where the solution is discontinuous, higher order schemes can be used in regions where the solution is smooth, by means of controlling their gradients. This was the idea proposed by (Boris and Book, 1973; Boris and Book, 1976), (Van Leer, 1973; Van Leer, 1974). Consequently, schemes such as the *Monotonic Upwind Scheme for Conservation Laws* (MUSCL) (Van Leer, 1979) which is a Godunov-type of scheme, or *Essentially Non-Oscillatory* (ENO) type of schemes (Harten and Osher, 1987), were developed permitting higher accuracy. Whereas the former relaxes its accuracy in the presence of a discontinuity, in the latter an nth-order polynomial is heuristically constructed ensuring the smoothness. In both examples, second-order accuracy in space and time is achieved for smooth solutions but lowered in the presence of shocks to ensure that oscillations are not produced.

Extensive studies have been carried out on flux-limiters analysing their stability properties. Typical examples found in LeVeque (2002), and Hirsch (2007) analyse the various possible, linear and nonlinear, limiters example of which are:

- The *MinMod* introduced by Roe (1986) is a special case of Chakravarthy and Osher (1983), where the upwind and downwind slopes are compared and the one with the smaller magnitude is chosen.
- The *Superbee* Roe (1985), where each one-sided gradient is compared with twice the opposite one-sided gradient and finally the one with the larger modulus is chosen.
- The *MC* (Monotonised-Central difference limiter) Van Leer (1977), where the centered difference is compared against twice the upwind and downwind differences.

This discussion goes alongside with the evaluation of schemes such as the Lax-Wendroff (LW) (Lax and Wendroff, 1960) and MacCormack (MacCormack, 1969)

which are of second order accuracy. The LW scheme can straightforwardly be obtained from a Taylor series expansion to second order terms. It is more practical though, to refer to the Richtmyer-Lax-Wendroff (RLW) two-step formulation, first introduced in Richtmyer (1962), which eliminated the necessity for the calculation of the Jacobian and consists of a first-order (Lax-Friedrich) spatial discretisation and a leapfrog central difference in time. The idea of the MacCormack scheme can be considered to fall from the RLW scheme and it equivalently consists of a predictor-corrector model coupled with using forward differencing initially, followed by backward differencing to achieve the second order accuracy. It is worth noticing that for the constant coefficient linear advection problem, both of those schemes are identical to each other. This is no longer the case in extending to nonlinear problems where they overlap in their second-order accuracy in space and time but their merits do not tip the scale in favour of either of them.

Regardless of the numerical scheme used, the form the equations are expressed in, affects both the algorithm stability as well as correctness of the solution. Smooth solutions aside, nonconservative methods cannot be expected to converge to the correct solution. This can be better understood in considering the integral formulation, as opposed to the differential equation, which forms the mathematical basis in deriving the Rankine-Hugoniot conditions that govern the correct description and propagation of shock waves. Lax (1954) as well as LeVeque (2002) and Hirsch (2007) emphasised and demonstrated the necessity of the conservative form of equations in order to obtain the correct jump relations in discontinuous solutions.

Chapter 2

Theoretical background

2.1 Overview

In this chapter, an introduction is presented into fluid mechanics and the equations describing their macroscopic mechanics along with the coupling involved in the presence of an electromagnetic field acting on a conductive fluid. The assumptions leading to the shallow water approximation are explored, gradually building-up towards the mathematical description of the two-layer system which will be studied in both its magnetohydrodynamic as well as purely hydrodynamic description.

2.2 Basic hydrodynamic equations

Macroscopic fluid flow is described by the velocity $\mathbf{u} = (u, v, w)$, density ϱ and pressure p. These are functions of time t and the position $\mathbf{r} = (x, y, z)$. Consider a fixed fluid volume $\mathcal{V}$ with mass $\int \varrho \, d\mathcal{V}$. The rate of variation of this mass is equal to the mass flux through the enclosing surface $\mathcal{S}$:

$$\frac{d}{dt} \iiint_{\mathcal{V}} \varrho \; d\mathcal{V} = - \oiint_{\mathcal{S}} \varrho \; \mathbf{u} \cdot \mathbf{n} \; d\mathcal{S}.$$

Using the divergence theorem, we have:

$$\iiint_{\mathcal{V}} \left(\frac{\partial \varrho}{\partial t} + \nabla \cdot (\varrho \mathbf{u}) \right) d\mathcal{V} = 0.$$

To be applicable to any fixed volume $\mathcal{V}$, a zero integrand is required: $\frac{\partial \varrho}{\partial t} + \nabla \cdot (\varrho \mathbf{u}) = 0$, which describes local mass conservation. In terms of the material derivative[1] it reads as:

$$\frac{D\varrho}{Dt} + \varrho \nabla \cdot \mathbf{u} = 0.$$

[1] $\frac{D}{Dt} \equiv \frac{\partial}{\partial t} + \mathbf{u} \cdot \nabla$

For an incompressible fluid we have $\frac{D\varrho}{Dt} = 0$, which yields:

$$\nabla \cdot \mathbf{u} = 0. \tag{2.1}$$

Newton's second law defines the rate of change of the momentum which must equal to the total net force, comprised of short-ranged surface and long-ranged body force, acting on the fluid volume. Therefore, formulating Newton's law for a fluid, Cauchy's momentum equation is obtained in the following form

$$\frac{D(\varrho \mathbf{u})}{Dt} = \nabla \cdot \tau + \mathbf{f}, \tag{2.2}$$

where τ is the stress tensor and $\mathbf{f}$ is the density of body forces applied to the fluid. These body forces encompass forces per unit mass - external gravity force: $\mathbf{f}_g = -\varrho\ \mathbf{g}$ - as well as forces per unit volume, such as electromagnetic forces, which will be later defined in §2.4. For an isotropic fluid the stress tensor equals $\tau = -p\mathbf{I}+\mathbf{T}$, where p is the pressure, $\mathbf{I}$ is the identity tensor and $\mathbf{T}$ is the deviatoric stress tensor. For an incompressible viscous fluid, the latter yields the viscosity term: $\mathbf{T} = \mu\left(\nabla\mathbf{u} + (\nabla\mathbf{u})^T\right)$, where μ is the dynamic viscosity coefficient.This stress tensor describes the stresses acting on a surface due to pressure and viscosity. Hence, the no-stress conditions at the surface are given by:

$$\tau = 0 \text{ on } \Gamma, \tag{2.3}$$

At the solid boundary wall two alternative conditions can be considered. The first condition applied at the boundary of a solid surface writes as:

$$\mathbf{u} = 0 \text{ on } \Gamma, \tag{2.4}$$

This condition, commonly referred to as the no-slip condition, means that the normal component as well as the tangential components assume zero velocity relative to the stationary boundary

An alternative formulation permitting the velocity to be expressed in terms of the tangential component of the stress reads as

$$\mathbf{u} \cdot n = 0, \qquad (\mathbf{T} \cdot n)_\tau + \gamma\mathbf{u} = 0. \tag{2.5}$$

where $(\mathbf{T} \cdot n)_\tau = n \times (\mathbf{T} \cdot n) \times n$ expresses the tangential to the bottom components and defines that the tangential stress is proportional to the tangential velocity of the fluid and γ is the frictious parameter. This is the Navier wall law where the slip-with-friction boundary condition defines stagnant layer of fluid close to the wall allowing a fluid to slip. Additionally, it requires the tangential, to the boundary, component of the strain tensor to be proportional to the tangential component of the fluid velocity.

A crucial simplification is imposed when in addition to the incompressibility condition, a homogeneous fluid is considered, which requires that $\varrho \equiv constant$. Consequently, using the material derivative[1] onto Eq. (2.2), the equation is recast in to the incompressible Navier-Stokes equation:

$$\varrho \left(\frac{\partial \mathbf{u}}{\partial t} + (\mathbf{u} \cdot \nabla)\, \mathbf{u} \right) = -\nabla p + \mu \nabla^2 \mathbf{u} + \varrho\, \mathbf{g} + \mathbf{f}. \tag{2.6}$$

If viscous effects are negligible then Euler's equation is recovered:

$$\varrho \left(\frac{\partial \mathbf{u}}{\partial t} + (\mathbf{u} \cdot \nabla)\, \mathbf{u} \right) = -\nabla p + \varrho\, \mathbf{g} + \mathbf{f}. \tag{2.7}$$

The no-penetration boundary condition supplements the equations of motion by requiring that $\mathbf{u} \cdot n = 0$. In the more general setting of a moving surface this defines that the velocity and pressure distribution across a surface must be equal.

2.3 Maxwell's equations

The equations governing time-dependent electric and magnetic fields were first found by (Maxwell, 1861; Maxwell, 1865). The Maxwell-Ampère equation, with Maxwell's displacement current correction $\mathbf{j} + \partial_t \mathbf{D}$, accounting for the induction of a magnetic field $\mathbf{H}$ generated by a varying electric field, is found in:

$$\partial_t \mathbf{D} + \mathbf{j} = \nabla \times \mathbf{H}, \tag{2.8}$$

where $\mathbf{D}$ is the electric induction and $\mathbf{j}$ the current density. This correction is crucial for the description of rapidly fluctuating fields and complements the pre-Maxwell equations which, Faraday's law excluded, were derived based on steady-state observations:

Ampère's law	$\nabla \times \mathbf{H} = \mathbf{j},$	(2.9)
Coulomb's law	$\nabla \cdot \mathbf{D} = q,$	(2.10)
No monopoles	$\nabla \cdot \mathbf{B} = 0,$	(2.11)
Faraday's law	$\nabla \times \mathbf{E} + \partial_t \mathbf{B} = 0,$	(2.12)

where q is the charge density[2], $\mathbf{E}$ is the electric field and $\mathbf{B}$ is the magnetic induction.

[2]The notation q rather than ρ is used here to avoid confusion with the fluid density ϱ.

The expressions relating **D**, **E**, **H** and **B** in the vacuum are:

$$\begin{cases} \mathbf{D} = \epsilon_0 \mathbf{E}, \\ \mathbf{H} = \mu_0^{-1} \mathbf{B}, \end{cases} \tag{2.13}$$

where ϵ_0 and μ_0 define the speed of light $c^2 = (\epsilon_0 \mu_0)^{-1}$. Maxwell's equations for the vacuum then read as:

$$\begin{cases} \partial_t (\epsilon_0 \mathbf{E}) = \mu_0^{-1} \nabla \times \mathbf{B} - \mathbf{j}, & \text{(2.14a)} \\ \nabla \cdot \mathbf{E} = \epsilon_0^{-1} q, & \text{(2.14b)} \\ \partial_t \mathbf{B} + \nabla \times \mathbf{E} = 0, & \text{(2.14c)} \\ \nabla \cdot \mathbf{B} = 0. & \text{(2.14d)} \end{cases}$$

Taking the divergence of Eq. (2.14a) and combining it with Eq. (2.14b) one obtains the conservation of electric charges:

$$\partial_t q + \nabla \cdot \mathbf{j} = 0, \tag{2.15}$$

relating the temporal rate of charge variation q to its flow across the surface of a volume.

2.4 Governing MHD equations

Similarly to Eq. (2.13) **D**, **E**, **H** and **B** in medium are related by:

$$\begin{cases} \mathbf{D} = \epsilon \mathbf{E}, \\ \mathbf{H} = \mu^{-1} \mathbf{B}, \end{cases} \tag{2.16}$$

where μ is the magnetic permeability and ϵ is the electric permittivity of the medium which are defined relative to the vacuum values by:

$$\begin{cases} \epsilon = \epsilon_r \epsilon_0, \\ \mu = \mu_r \mu_0, \end{cases} \tag{2.17}$$

where the parameters ϵ_r and μ_r are respectively the relative permittivity and permeability of the material. For an isotropic electrically conducting liquid the permittivity and the permeability are usually equal to the vacuum values (Moreau, 1990; Gerbeau, Le Bris et al., 2006). Consequently, following Eq. (2.14) for a perfect dielectric (i.e. no external current) medium Maxwell's equations become:

$$\begin{cases} \partial_t (\epsilon \mathbf{E}) = \mu^{-1} \nabla \times \mathbf{B} - \mathbf{j}, & (2.18a) \\ \nabla \cdot \mathbf{E} = \epsilon^{-1} q, & (2.18b) \\ \partial_t \mathbf{B} + \nabla \times \mathbf{E} = 0, & (2.18c) \\ \nabla \cdot \mathbf{B} = 0. & (2.18d) \end{cases}$$

Furthermore, Ohm's constitutive law provides the link connecting $\mathbf{j}$ and $\mathbf{E}$, where in a conducting medium $\mathbf{j}$ is proportional to the local electric field experienced by the moving particle:

$$\mathbf{j} = \sigma (\mathbf{E} + \mathbf{u} \times \mathbf{B}) . \tag{2.19}$$

Here σ is the electrical conductivity and the term $\mathbf{u} \times \mathbf{B}$ takes in to consideration the field induced by the motion.

In the definition of Euler's equation Eq. (2.7), in absence of any additional volumetric force $\mathbf{f}$ the purely hydrodynamic limit is recovered. Conversely, the influence of an electromagnetic field acting on a conducting fluid, gives rise to the MHD coupling. At macroscopic scale, passing through fluid in the presence of a current, the magnetic field generates a Lorentz force:

$$\mathbf{f} = \mathbf{j} \times \mathbf{B}. \tag{2.20}$$

This stems from the coupling of Maxwell's equations and fluid mechanics which enter the system via the Lorentz force. The magnetohydrodynamic set of equations in the more general form then reads as follows:

$$\begin{cases} \varrho \left(\dfrac{\partial \mathbf{u}}{\partial t} + (\mathbf{u} \cdot \nabla) \, \mathbf{u} \right) = -\nabla p + \varrho \, \mathbf{g} + \mathbf{j} \times \mathbf{B}, \\ \partial_t \mathbf{B} + \nabla \times \mathbf{E} = 0, \\ \partial_t (\epsilon \mathbf{E}) = \mu^{-1} \nabla \times \mathbf{B} - \mathbf{j}, \\ \nabla \cdot \mathbf{E} = \epsilon^{-1} q, \\ \mathbf{j} = \sigma (\mathbf{E} + \mathbf{u} \times \mathbf{B}) \end{cases} \tag{2.21}$$

2.5 Basic assumptions for aluminium reduction cells

Since its inception HHCs have been known to suffer from instabilities. Under certain circumstances the perturbation arising may grow to an extent which disrupts the operation the cell. Implications resulting from this mechanism entail

increased cost and longer production times.

The configuration of aluminium reduction cells consists of a high intensity electric current passing sequentially through the carbon anodes, the electrolyte layer which reduces the alumina, the molten aluminium layer and the carbon cathode where the current is collected, while the boundary walls of the cell are assumed to be perfectly insulating (Grjotheim and Kvande, 1993). The respective electrical conductivities are:

$$\sigma_- \equiv \sigma_{\text{electrolyte}} \ll \sigma_{\text{carbon}} \ll \sigma_{\text{aluminium}} \equiv \sigma_+,$$

where $\sigma_+ = 3.3 \cdot 10^6\,(\Omega \cdot \text{m})^{-1}$, $\sigma_- = 2.5 \cdot 10^2\,(\Omega \cdot \text{m})^{-1}$ (Gerbeau, Le Bris et al., 2006) and $\sigma_{\text{carbon}} = 2 \cdot 10^4\,(\Omega \cdot \text{m})^{-1}$ (Molokov et al., 2011).

An immediate consequence of the electrolyte layer's poor conductivity is an increased energy consumption owing to its conversion into Ohmic heating. Straightforwardly, thinner layer would result in an increased energy efficiency.

The physical set-up of a rectangular cell of size $L_x \times L_y$ consists of shallow but broad electrolyte-alumina layers ($H \ll L$). This framework renders the system an ideal candidate for the application of the shallow water approximation where the characteristic longitudinal length scale of the perturbation, L, is much larger than the layers depth, H. The two-layer system is subject to a downward gravity force with the free fall acceleration g. The velocity of each layer is considered uniform and vertically invariant; i.e the vertical velocity, w, has a relatively small magnitude $\sim H/L = \varepsilon \ll 1$, which means that the associated fluid flow is predominantly horizontal with the velocity $\mathbf{u} = u\mathbf{e}_x + v\mathbf{e}_y$.

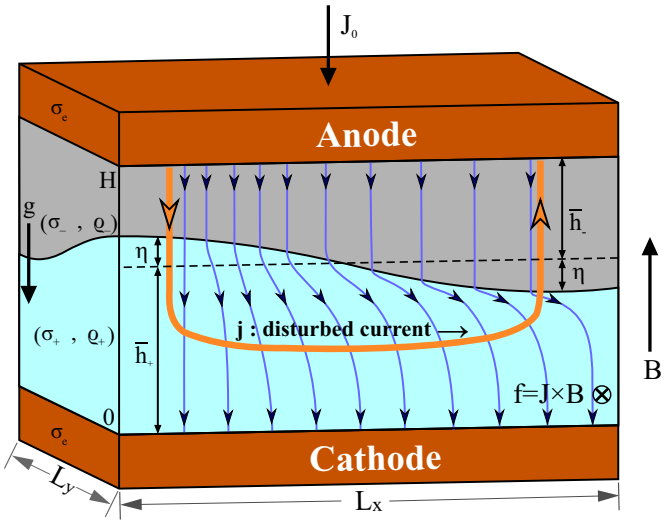

FIGURE 2.1: Schematic representation of the aluminium smelting process, with a vertical component of the magnetic field and a perturbation at the interface.

The magnitude of difference in the layers' specific conductivities lays the premises for the interface between the aluminium and cryolite layers as well as the interface between the carbon anode and cryolite to be approximately considered as an equipotential surface. Furthermore, the low electric conductivity of cryolite, along with the shallow-layer layout, permits the assumption that, in the long-wavelength, the electric current within the layer take the shortest path between the anode block and aluminium, i.e. they are primarily vertical in the electrolyte (Davidson, 2001, p. 366). Any change in the position of the interface between the two fluids gives rise to a perturbation in the current distribution, as the electrical path in the electrolyte is either decreased or increased. This also means that the Lorentz force exerted on the layer of cryolite is negligible in comparison to that of aluminium. Consequently, the Lorentz force in the upper layer is insignificant and is only considered in the lower layer.

For a material of uniform conductivity with steady current, Eq. (2.15) reduces to:

$$\nabla \cdot \mathbf{j} = 0. \tag{2.22}$$

On the basis, that charges are varying much slower than the speed of light, the pre-Maxwell formulation is recovered, and hence, it can be inferred that:

$$\nabla \times \mathbf{B} = \mu \mathbf{j},$$

whereupon taking the divergence of Eq. (2.18a) and using Gauss' (electrostatic) law it can be shown that the contribution of $\partial_t (\epsilon \mathbf{E})$ is negligible, thus Ampere's circuital law is recovered while omitting Maxwell's correction term. Moreover the magnetic field must satisfy $\nabla \cdot \mathbf{B} = 0$, which is the solenoidal constraint requiring the net magnetic flux of any closed surface to be zero.

At this stage, it is advantageous to separate the magnetic field, into two components. The first is the externally imposed magnetic field $\mathbf{B}_0$ generated by the current supplying the cell, whereas the second part $\mathbf{b}$ is the induced magnetic field. Hence, for $\mathbf{B} = \mathbf{B}_0 + \mathbf{b}$ Ampere's law requires $\nabla \times \mathbf{B}_0 = 0$. In poorly conducting fluids, such the ones found in aluminium reduction cells, the induced magnetic field is much weaker than the externally imposed magnetic field, i.e. $\mu_0 j_0 L \ll B_0$. Hence, a quasi-static approximation $\partial_t \mathbf{B} \approx 0$ can be employed, where $\mathbf{B} \sim \mathbf{B}_0$, and thus:

$$\nabla \times \mathbf{E} \approx 0,$$

Consequently, for a fixed and uniform magnetic field in the electrostatic approximation the electric field writes as follows:

$$\mathbf{E} = -\nabla\phi,$$

where ϕ is the perturbation of the electric potential.

It has been established that the external current generate strong external, primarily vertical magnetic field $\mathbf{B}_0 = B_0 e_z$. Additionally, the velocity can be assumed to have no influence on the magnetic field (Moreau, 1990), thus $\mathbf{u} \times \mathbf{B}$ is of minor influence, leading to the Lorentz force being written as:

$$\mathbf{f} = \mathbf{j} \times \mathbf{B} = -\sigma\nabla \times (\phi B_0)\,. \tag{2.23}$$

The resulting expression has undergone several layers of simplifications based on the time variation of the flow, and the intensity of the electromagnetic fields. Particular attention should be drawn though, on ignoring the term $\mathbf{u}\times\mathbf{B}$. As noted by Gerbeau, Le Bris et al. (2006) this term corresponds to a worst case scenario in the stability of the system because induced currents can have stabilising effects on the flow.

2.6 Single-layer shallow-water model

Computationally, the three-dimensional system poses onerous difficulties in numerical resolution and discretisation. The shallow-water approximation, when applicable, reduces the complexity of the computational problem from three to two dimensions. The shallow-water approximation is used in meteorology, oceanography and engineering applications such as aluminium reduction cells and liquid metal batteries. The conventions enabling the shallow-water approximation are further detailed in this section.

The shallow-water approximation is based on the assumption that the typical vertical length scale (H) of the system is much smaller than the typical horizontal length scale (L): $\epsilon = \frac{H}{L} \ll 1$. Hence, the vertical acceleration of a fluid during the passage of the wave remains small. The pressure in the fluid layer is considered hydrostatic i.e. $\frac{\partial p}{\partial z} = -\varrho g e_z + \mathcal{O}(\epsilon^2)$, thus enabling the calculation of the local pressure.

It is convenient to reformulate Eq. (2.7) such that the horizontal components are separated from the vertical one:

$$\begin{cases} \nabla \cdot \mathbf{u} + w_z = 0, & \text{(2.24a)} \\ \varrho \left(\mathbf{u}_t + (\mathbf{u} \cdot \nabla) \mathbf{u} + w \mathbf{u}_z \right) + \nabla p = 0, & \text{(2.24b)} \\ \varrho \left(w_t + \mathbf{u} \cdot \nabla w + w w_z \right) + p_z = -\varrho g. & \text{(2.24c)} \end{cases}$$

Henceforth $\mathbf{u} = (u, v)$, subscripts of (x, y, z, t) define partial derivatives in the respective variable and the operator $\nabla = \left(\partial_x, \partial_y\right)$.

In the case of a fluid of uniform density under the influence of a uniform body force due to gravity, the relation between pressure and height is given by integration of Eq. (2.24c) which results in the following linear equation:

$$p = \Pi + \varrho g \left(h - z \right) \tag{2.25}$$

where Π is the constant of integration $\Pi(\mathbf{x}, t) = p(\mathbf{r}, t)|_{z=h}$ and it depends on the boundary conditions or the influence of the overlying fluid. In the case of a free surface, pressure should be continuous, hence, the atmospheric pressure is assumed to be zero above the free surface h: $p = \varrho g \left(h - z \right)$. Then, the horizontal gradient operator with the z-component omitted, results in a depth-invariant expression for pressure:

$$\nabla p = \varrho g \nabla h. \tag{2.26}$$

The kinematic boundary condition of the vertical component of the momentum equations at a flat bottom topography requires no normal flow at the rigid surface i.e. $w(0) = 0$. Upon integration of the continuity equation along the vertical axis, Eq. (2.1) yields:

$$[w]_0^h = h \nabla \cdot \mathbf{u}$$

At the free surface, w is equal by definition to the time derivative of the interface height:

$$w(h) = \frac{Dh}{Dt}.$$

Combination of these two expression above, yield the mass conservation of the shallow-water equations:

$$\frac{\partial h}{\partial t} + \nabla \cdot (h \mathbf{u}) = 0. \tag{2.27}$$

The flow is assumed to be irrotational which in turn requires that in the leading order approximation $\mathbf{u}_z = 0$. Therefore, considering Eq. (2.24b), while multiplying with h in order to recover the commonly found in textbooks expression, the

momentum conservation for the single-layer shallow-water model writes as:

$$\partial_t (h\mathbf{u}) + \nabla \cdot \left(h\mathbf{u}^2\right) + \frac{g}{2}\nabla \left(h^2\right) = 0, \tag{2.28}$$

where presently, the density parameter, being constant, has been omitted from the momentum equation. Hereafter, $\mathbf{u}^2 = \mathbf{u}\mathbf{u}$ denotes the tensorial product.

Finally, the energy conservation for the single layer shallow-water model is derived in multiplying Eq. (2.28) with the velocity $\mathbf{u}$, leading to

$$\frac{\partial}{\partial t}\frac{1}{2}\left(h\|\mathbf{u}\|^2 + gh^2\right) + \nabla \cdot \left(\frac{1}{2}\left(g\mathbf{u}h^2 + \frac{1}{2}h\mathbf{u}\|\mathbf{u}\|^2\right)\right) = 0. \tag{2.29}$$

A more detailed derivation can be found in Johnson (1997, Chapter 1.2.5) and Vallis (2017, Chapter 3.6.2).

2.7 Two-Layer shallow-water model

In contrast to the single-layer model, where interaction with the ambient environment is considered negligible; in stratified models there exists an interdependence. On account of this interaction, the intricacy of the analysis is augmented. Their span of applicability, ranging from atmospheric to oceanic dynamics, is portrayed in more detail in (Pedlosky, 1979; Vreugdenhil, 1994).

A subset of stratified fluid theory is the two-layer model where two fluids of homogeneous but distinct densities ϱ_+ and ϱ_- are examined. An illustration of the two-layer problem is given in figure 2.2. The case of two-layer flows has been briefly examined by various classic textbooks, such as (Tan, 1992; Salmon, 1998; Gill, 1983), in the context of free upper surface or quasi-geostrophic flows where quite frequently the reduced gravity (or one-and-a-half layer) approximation Salmon (1998, Chapter 2) is employed, where horizontal pressure gradients are replaced by the fluid interaction in their gravity terms. This approximation is based on the buoyancy effects of the upper layer altering the gravitational restoring force of the lower layer. This translates to a fluid adjustment, corresponding to a reduced gravitational constant, owing to surface displacement being of smaller magnitude than the interior interface displacement. In oceanography this commonly used simplification has been named rigid-lid approximation.

Discarding any assumption for the scale of the upper surface elevation, the rigid-lid approximation introduces a pressure force acting on the fluids confined under it. The reference height at which pressure is defined depends on the application and individual preference. In contrast to common approach, where the pressure at the top boundary is used as a reference pressure(Vallis, 2017,

Chapter 3.2.1), it is beneficial to use the interfacial pressure for this purpose. On account of a continuous pressure distribution at the interface, this choice leads to a symmetric form of the momentum equations. Therefore, the horizontal gradient of pressure is given by:

$$\nabla p = \pm \varrho_{\pm} \nabla h_{\pm} + \nabla \Pi \tag{2.30}$$

in the respective layers.

Bearing in mind that the normal components of velocity at the interface must be the same for the two fluids the mass conservation for each layer writes as:

$$\frac{\partial h_{\pm}}{\partial t} + \nabla \cdot (h_{\pm} \mathbf{u}_{\pm}) = 0, \tag{2.31}$$

where subscript $\pm$ indicates the lower or upper layer respectively; and as seen in figure 2.2, each height component is split into an initial thickness and a perturbed part, i.e. $h_{\pm} = \bar{h}_{\pm} \pm \eta$.

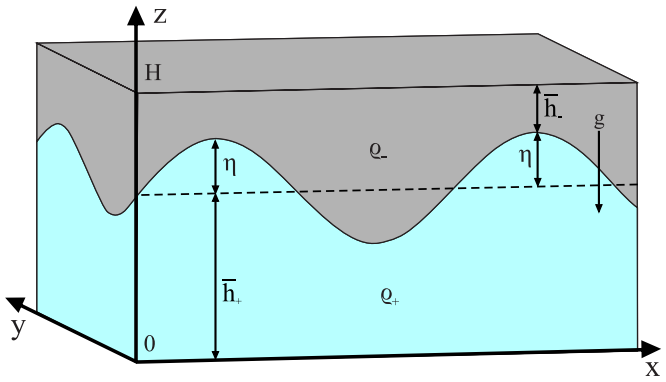

FIGURE 2.2: Sketch of the fluid domain.

On account of the rigid-lid approximation, the total height of the system is $h_+ + h_- = H = constant$. Therefore, the volume conservation across the layers is:

$$\nabla \cdot (h_+ \mathbf{u}_+ + h_- \mathbf{u}_-) = 0. \tag{2.32}$$

Starting from Eq. (2.24) while keeping note of the shallow-water approximation, the momentum equations for the two layers write as

$$\varrho_{\pm} \Big((\mathbf{u}_{\pm})_t + (\mathbf{u}_{\pm} \cdot \nabla) \mathbf{u}_{\pm} \pm g \nabla h_{\pm} \Big) = -\nabla \Pi, \tag{2.33}$$

where a simplification can be achieved by employing the expression $h_{\pm} = \bar{h}_{\pm} \pm \eta$ which leads to:

$$\varrho_{\pm} \Big((\mathbf{u}_{\pm})_t + (\mathbf{u}_{\pm} \cdot \nabla) \mathbf{u}_{\pm} + g \nabla \eta \Big) = -\nabla \Pi, \tag{2.34}$$

and the gravity term is subtracted on either side of the equation such that:

$$\varrho_{\pm}\Big((\mathbf{u}_{\pm})_t + (\mathbf{u}_{\pm}\cdot\nabla)\,\mathbf{u}_{\pm}\Big) + \varrho_{\pm} g\nabla(\eta) - \bar{\varrho} g\nabla\eta = -\nabla\Pi - \bar{\varrho} g\nabla\eta,$$

where $\bar{\varrho} = \frac{(\varrho_- + \varrho_+)}{2} = \frac{\{\varrho\}}{2}$ is used, which expresses an average of the fluid densities and the $\{\}$ denoted summation of the enclosed quantity. Likewise, it is convenient to introduce $[f] \coloneqq f_+ - f_-$, in which the square brackets denote the difference of the enclosed quantities.

The interfacial pressure can be redefined such that:

$$\tilde{\Pi} = \Pi - \bar{\varrho} g\eta,$$

which permits a symmetric description of the two-layer equations and it is advantageous in eliminating the density in the gravity terms in the Boussinesq approximation as considered in §2.7.2. Subsequently, the hydrodynamic equations take the following form:

$$\varrho_{\pm}\Big((\mathbf{u}_{\pm})_t + (\mathbf{u}_{\pm}\cdot\nabla)\,\mathbf{u}_{\pm}\Big) \pm \frac{g\,[\varrho]}{2}\nabla\eta = -\nabla\tilde{\Pi}.$$

As a last step, the height term $h_{\pm}$ is reinstated and the interfacial displacement η in the gravity term is replaced by:

$$\varrho_{\pm}\Big((\mathbf{u}_{\pm})_t + (\mathbf{u}_{\pm}\cdot\nabla)\,\mathbf{u}_{\pm}\Big) + \frac{g\,[\varrho]}{2}\nabla h_{\pm} = -\nabla\tilde{\Pi}. \tag{2.35}$$

Similarly to Eq. (2.28), upon multiplication with the respective layer height, the two-layer momentum equation Eq. (2.35) writes as:

$$\varrho\Big((h\mathbf{u})_t + \nabla\cdot\left(h\mathbf{u}^2\right)\Big) + \frac{g\,[\varrho]}{4}\nabla\left(h^2\right) = -h\nabla\tilde{\Pi}, \tag{2.36}$$

where for the sake of clarity $\mathbf{u} \equiv \mathbf{u}_{\pm}$, $\varrho \equiv \varrho_{\pm}$.

The energy equation is obtained by taking a scalar product of the velocity with Eq. (2.36). After few rearrangements this reads as:

$$\varrho\Big(\left(h\|\mathbf{u}\|^2\right)_t + \nabla\cdot\left(\mathbf{u}h\|\mathbf{u}\|^2\right)\Big) + \mathbf{u}h\Big(g\,[\varrho]\,\nabla(h)\Big) = -2\mathbf{u}h\nabla\tilde{\Pi},$$

where for both layers $\mathbf{u}h\cdot\nabla h = \nabla\cdot\left(\mathbf{u}h^2\right) - h\nabla\cdot(\mathbf{u}h)$ and likewise for the pressure term. Hence, employing the mass conservation Eq. (2.31) the total energy obtained by summation over the two layers, after few rearrangements, reads as follows:

$$\left\{\varrho h\|\mathbf{u}\|^2 + \frac{g\,[\varrho]}{2}h^2\right\}_t + \nabla\cdot\left\{\mathbf{u}\left(\varrho h\|\mathbf{u}\|^2 + g\,[\varrho]\,h^2\right)\right\} = -2\nabla\cdot\left\{\mathbf{u}h\tilde{\Pi}\right\}, \tag{2.37}$$

Laslty, the equation for pressure is given by taking the divergence of the sum of the two layers which upon recalling the incompressibility condition Eq. (2.32)

leads to an elliptic equation of the form:

$$\nabla \cdot \left(\left\{ \frac{h}{\varrho} \right\} \nabla \tilde{\Pi} \right) = -\nabla \cdot \left(\nabla \left\{ h\mathbf{u}^2 \right\} - \frac{g\,[\varrho]}{4} \nabla \left\{ \frac{h^2}{\varrho} \right\} \right). \tag{2.38}$$

2.7.1 Nondimensionalisation

The choice of scaling parameters used in this work deviates form the ones encountered in other studies (Bojarevics and Romerio, 1994) where height is scaled with $\frac{\bar{h}_+\bar{h}_-}{\bar{h}_+ + \bar{h}_-}$ and the wave propagation speed with the root of $g\,[\varrho] \left\{ \frac{\varrho}{\bar{h}} \right\}^{-1}$. The choice of these parameters is based on the argument of large amplitude waves where the aforementioned alternative expressions would become irrelevant.

The characteristic scales used to nondimensionalise the equations are given in the following table.

Description	**Quantity**	**Scaling**
Horizontal dimensions:	L_x, L_y	$L = \sqrt{L_x L_y}$
Vertical dimension:	$h_\pm, \eta$	H
Density	ϱ	$\bar{\varrho} = \frac{\varrho_+ + \varrho_-}{2}$
Velocity:	$\mathbf{u}$	$C = \sqrt{2g \frac{[\varrho]}{\{\varrho\}} H}$
Time:	t	$\frac{L}{C}$
Pressure:	$\tilde{\Pi}$	$g\,[\varrho]\,H$
Electric potential:	ϕ	$\frac{I_0}{\sigma_+ H}$

TABLE 2.1: Characteristic scales for normalisation

For the sake of brevity, the same symbols are subsequently used to denote dimensionless quantities. Therefore, the system of Eqs. (2.31), (2.36) and (2.37) in each layer expressed in the nondimensional form reads as:

$$\begin{cases} (h)_t + \nabla \cdot (h\mathbf{u}) = 0, & \text{(2.39a)} \\ \varrho \Big((h\mathbf{u})_t + \nabla \cdot \left(h\mathbf{u}^2 \right) \Big) + \frac{\{\varrho\}}{8} \nabla \left(h^2 \right) = -h \nabla \tilde{\Pi}, & \text{(2.39b)} \\ \left\{ \varrho h \|\mathbf{u}\|^2 + \frac{\{\varrho\}}{4} h^2 \right\}_t + \nabla \cdot \left\{ \mathbf{u} \left(\varrho h \|\mathbf{u}\|^2 + \frac{\{\varrho\}}{2} h^2 \right) \right\} = -2\nabla \cdot \left\{ \mathbf{u} h \tilde{\Pi} \right\}. & \text{(2.39c)} \end{cases}$$

2.7.2 The Boussinesq approximation

A significant simplification is possible in gravity-driven flows when density does not depart significantly from a mean reference value $\bar{\varrho}$. Thus, on the premises that relative -spatial and temporal- variations of density are non-consequential compared with the velocity field, it can be postulated that $\varrho_+ \simeq \varrho_-$. Nonetheless, gravity is, comparatively, potent enough to make the specific weight considerably different between the two fluids, and thus remains relevant only in the gravity terms of the momentum equations as seen in Eq. (2.39). Thus, Eqs. (2.39b) and (2.39c) simplify into:

$$\begin{cases} (h\mathbf{u})_t + \nabla \cdot \left(h\mathbf{u}^2\right) + \dfrac{1}{4}\nabla\left(h^2\right) = -h\nabla\tilde{\Pi}, & \text{(2.40a)} \\ \left\{h\|\mathbf{u}\|^2 + \dfrac{1}{2}h^2\right\}_t + \nabla \cdot \left\{\mathbf{u}\left(h\|\mathbf{u}\|^2 + h^2\right)\right\} = -2\nabla \cdot \left\{\mathbf{u}h\tilde{\Pi}\right\}, & \text{(2.40b)} \end{cases}$$

Owing to the rigid-lid condition as well as the Boussinesq approximation, the non-dimensional form of Eq. (2.38) simplifies into a Poisson equation which reads as:

$$\nabla^2\tilde{\Pi} = -\nabla \cdot \left(\nabla\left\{h\mathbf{u}^2\right\} - \frac{1}{4}\nabla\left\{h^2\right\}\right). \tag{2.41}$$

2.7.3 The Sele parameter

In the preceding chapter the model with uniform vertical magnetic field was introduced while defining the stability of the system. The electromagnetically-driven rotating motion of the interface was first identified by Sele (1977), who introduced a parameter characterising this instability. This nondimensional parameter defines the relative magnitude of the electromagnetic and gravity forces. Following Gerbeau, Le Bris et al. (2006), Davidson and Lindsay (1998) and Molokov et al. (2011), the Sele nondimensional parameter can be writen as:

$$\beta = \frac{I_0 B_0}{g\left(\varrho_+ - \varrho_-\right)\bar{h}_+\bar{h}_-}. \tag{2.42}$$

Depending on physical parameters and the geometry of the cell, there is a critical value of this parameter by exceeding which the system becomes unstable to a rotating interface tilt.

With the normalisation described in Table (2.1), and the Boussinesq approximation and recalling that the electromagnetic force is effective only in to the lower layer the equation for the bottom fluid is:

$$\frac{\bar{\varrho}C^2H}{L}\left((h\mathbf{u})_t + \nabla \cdot \left(h\mathbf{u}^2\right) + \frac{1}{4}\nabla\left(h^2\right) + h\nabla\tilde{\Pi}\right) = -\frac{HB_0\phi_0\sigma}{L}h\left(e_z \times \nabla\phi\right).$$

Therefore, the ratio of electromagnetic forces to gravity forces, writes as

$$\beta = \frac{B_0 \phi_0 \sigma_+}{\bar{\varrho} C^2} = \frac{B_0 I_0}{\bar{\varrho} C^2 H} = \frac{B_0 I_0}{g\,[\varrho]\,H^2}. \tag{2.43}$$

Due to the scaling used in this work the resulting key dimensionless parameter differs from that of Eq. (2.42) by a factor of $H^2/(\bar{h}_+\bar{h}_-)$. In using Eq. (2.43) the non-dimensional momentum equation in the Boussinesq approximation writes as:

$$(h\mathbf{u})_t + \nabla \cdot \left(h\mathbf{u}^2\right) + \frac{1}{4}\nabla\left(h^2\right) = -h\left(\nabla\tilde{\Pi} + \beta\; e_z \times \nabla\phi\right). \tag{2.44}$$

2.7.4 Linear friction

Although viscous effects have been thus far omitted from the shallow-water model description, oceanographic and engineering oriented approaches require the inclusion of dissipative terms that permit a more realistic description of physical phenomena. The resultant depth averaged viscous parameter coming from Eq. (2.6), has been meticulously derived and included in the description of shallow-water model in various classic textbooks such as (Tan, 1992; Pedlosky, 1979); however it is most often a friction parameter on the bottom corresponding to a wall-law similar to Navier friction which is employed under the shallow-water approximation. A review of such friction laws can be found in Tan (1992) and Pedlosky (1979). Concerning the 1D case, models featuring a viscous shallow-water approximation are derived in Gerbeau and Perthame (2001) and Audusse (2005) to first and second order of the shallowness parameter, offering a rigorous derivation of the viscous parameters, which though do not distinguish between the bottom and lateral friction. Marche (2007) offers the analogous derivation in 2D wherein a distinction is made between the laminar (linear with respect to the mean velocity) and turbulent viscous parameters.

In the context of MHD, an approximation first introduced by Lympany et al. (1982), and used thereafter in (Moreau and Evans, 1984; Bojarevics, 1998; Zikanov et al., 2000; Bojarevics and Pericleous, 2008), entails a simple linear friction term. As pointed out in Zikanov et al. (2000) "*... all the effects of turbulent-energy dissipation near the rigid walls and within the layers are incorporated into the linear-friction terms with the empirical friction coefficients...*". This rudimental implementation is preferred over more elaborate expressions for its simplicity which does not obscure the instability mechanism of the two-layer MHD system and the contribution of each parameter.

Therefore, the MHD two-layer system of equations including all friction effects, internal viscous and turbulent dissipation as well as the friction at rigid walls,

have been appended into a single expression in the following equations:

$$(h\mathbf{u})_t + \nabla \cdot \left(h\mathbf{u}^2\right) + \frac{1}{4}\nabla\left(h^2\right) = -h\left(\nabla\tilde{\Pi} + \beta\ e_z \times \nabla\phi\right) - \gamma\mathbf{u}, \tag{2.45}$$

where γ is the nondimensional linear friction coefficient for the respective layer.

2.8 Finite Volume Method

In this section the concept of conservation laws is introduced, which serves as the foundation for the numerical methods employed. The continuous description of time-dependent hyperbolic system of PDEs is recast into a finite set of discrete values which enable their spatio-temporal discretisation by a relevant algorithm. In anticipation of the discontinuities that inherently arise in the shallow-water approximation, the discretisation is performed on the basis of an integral formulation representing a conservation law. Following the discussion of §2.2, the evolution of q in a control volume is determined by the balance of net fluxes entering and leaving the volume, i.e. $\partial_t \int_{\mathcal{V}} q\ d\mathcal{V} = \int_{\mathcal{V}} \nabla \cdot \mathbf{Q}\ d\mathcal{V}$. Owing to the integral formulation of the governing equation, the conservation of the physical quantity is ensured also for discontinuous solutions.

In its numerical approximation, the PDE is solved via the finite-volume-method (FVM) where the conserved quantity enclosed within a finite volume-cell is calculated by taking the integral over the volume element. Following the path of the cell centre, it is assumed that the solution of q^n_Ω is known on the control cell Ω at timestep t^n. Considering its evolution over a subsequent step Δt, the solution q^{n+1}_Ω at $t^{n+1} = t^n + \Delta t$ is obtained by integrating over $\Omega \times \left[t^n, t^{n+1}\right]$:

$$\int_\Omega \int_{t^n}^{t^{n+1}} \partial_t q\ dt d\Omega = \int_\Omega \int_{t^n}^{t^{n+1}} \nabla \cdot \mathbf{Q}\ dt d\Omega\,,$$

and the solution to q^n_Ω is prescribed by the average of q over the control volume Ω (Godlewski and Raviart, 2013):

$$q^n_\Omega = \frac{1}{|\Omega|}\int_\Omega q\ d\Omega\,, \quad \text{where} \quad |\Omega| = \int_\Omega d\Omega\,. \tag{2.46}$$

In admission of this cell-average and using purely explicit fluxes, Eq. (2.8) writes as:

$$q^{n+1}_\Omega = q^n_\Omega - \frac{\Delta t}{|\Omega|}\int_\Omega \nabla \cdot \mathbf{Q}\ d\Omega. \tag{2.47}$$

In a rectangular computational domain $\Omega = [x_L, x_R] \times [y_L, y_R]$ a structured static cell is depicted in figure 2.3:

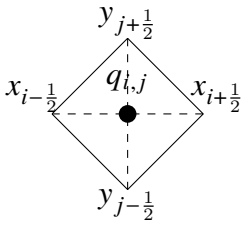

FIGURE 2.3: Control-volume schematic.

where the spatial increment Δx is defined by $\Delta x = x_{i+\frac{1}{2}} - x_{i-\frac{1}{2}}$ -equivalently for Δy- and the domain is considered equispaced throughout. The integral is approximated using a point located at the centre with the fluxes located at the interface of the cell, is interpreted as the average of the surrounding flux node elements. By definition of Eq. (2.46) and Eq. (2.47) one obtains

$$\begin{aligned} q_{i,j}^{n+1} = q_{i,j}^{n} &- \frac{\Delta t}{\Delta x \Delta y} \int_{y_{j-\frac{1}{2}}}^{y_{j+\frac{1}{2}}} \left(F(x_{i+\frac{1}{2}}, y_j, t^n) - F(x_{i-\frac{1}{2}}, y_j, t^n) \right) \, dy \\ &- \frac{\Delta t}{\Delta x \Delta y} \int_{x_{i-\frac{1}{2}}}^{x_{i+\frac{1}{2}}} \partial_y \left(G(x_i, y_{j+\frac{1}{2}}, t^n) - G(x_i, y_{j-\frac{1}{2}}, t^n) \right) \, dx \end{aligned} \tag{2.48}$$

where the divergence is $\nabla \cdot \mathbf{Q} = \partial_x F + \partial_y G$. Successively, the numerical fluxes are defined as:

$$\begin{aligned} F_{i+\frac{1}{2},j}^{n} &= \frac{1}{\Delta y} \int_{y_{j-\frac{1}{2}}}^{y_{j+\frac{1}{2}}} F(x_{i+\frac{1}{2}}, y_j, t^n) \, dy \\ G_{i,j+\frac{1}{2}}^{n} &= \frac{1}{\Delta x} \int_{x_{i-\frac{1}{2}}}^{x_{i+\frac{1}{2}}} G(x_i, y_{j+\frac{1}{2}}, t^n) \, dx \end{aligned} \tag{2.49}$$

which rewrites Eq. (2.48) to express the 2D geometry as:

$$q_{i,j}^{n+1} = q_{i,j}^{n} - \frac{\Delta t}{\Delta x} \left(F_{i-\frac{1}{2},j}^{n} - F_{i+\frac{1}{2},j}^{n} \right) - \frac{\Delta t}{\Delta y} \left(G_{i,j+\frac{1}{2}}^{n} - G_{i,j-\frac{1}{2}}^{n} \right) \tag{2.50}$$

In the case of a uniform Cartesian grid, the FVM may be related to the finite-differences (FD) method. However, the advantage held over the former is that the element located at the centre is not affected by the the boundary conditions applied onto the fluxes. The advantages of the FVM method are more pronounced for non-uniform meshes as well as in two-or-higher- dimensions whence curvature is more naturally dealt with the FVM due to the integral nature of the equations used. Indeed, FD method uses a pointwise approximation at the node of the cell where the corresponding derivatives are approximated by finite differences. In general such methods tend to be numerically unstable and break down near discontinuities. However, it is convenient to consider the finite difference interpretation when computing the local truncation error via a Taylor series expansion at a point.

2.9 1D Lax-Wendroff scheme

In this section the Lax-Wendroff scheme is presented in one-spatial dimension. Consider a system of conservation laws in one space dimension:

$$\partial_t \mathbf{U} + \partial_x \mathbf{F}(\mathbf{U}) = 0, \tag{2.51}$$

where $\mathbf{U}$ is a vector of the conserved quantities per unit volume and $\mathbf{F}$ is the flux rate per unit area.

The scheme introduced by (Lax and Wendroff, 1960) was constructed for solving 1D systems of conservation laws of the form Eq. (2.51) and falls from consideration of a Taylor's expansion

$$\mathbf{U}_i^{n+1} = \mathbf{U}_i^n + \Delta t \left(\partial_t \mathbf{U}\right)_i^n + \frac{(\Delta t)^2}{2} \left(\partial_t^2 \mathbf{U}\right)_i^n + O((\Delta t)^3). \tag{2.52}$$

Subsequently, substituting Eq. (2.51) in Eq. (2.52), the spatial derivatives replace the temporal derivatives. For the second-order term in Taylor's expansion, the Jacobian matrix $A = A(\mathbf{U}) = \frac{\partial \mathbf{F}}{\partial \mathbf{U}}$ is considered, leading to the single-step Lax-Wendroff scheme:

$$\mathbf{U}_i^{n+1} = \mathbf{U}_i^n + \Delta t \left(\partial_x \mathbf{F}\right)_i^n + \frac{(\Delta t)^2}{2} \left(\partial_x \left(A \partial_x \mathbf{F}\right)\right)_i^n + O((\Delta t)^3). \tag{2.53}$$

The system is hyperbolic if the Jacobian A is diagonalizable and admits real eigenvalues and a complete set of independent eigenvalues, such that

$$A = R \Lambda R^{-1}, \tag{2.54}$$

where R is the matrix of right eigenvectors and Λ the set of eigenvalues.

The single-step Lax-Wendroff scheme can be discretised using a FD method with second order accuracy in time and space. However, for nonlinear problems the substitution carried out in the temporal derivatives is neither unique nor straightforward. Furthermore, the single-step Lax-Wendroff is not well suited for FVM methods. Solutions to systems described by Eq. (2.51) contain discontinuities even if the initial data is smooth. On the theoretical analysis of hyperbolic conservation laws (Lax and Wendroff, 1960; Hou and LeFloch, 1994) complement each other. It is shown that numerical solutions of such systems, in the presence of shocks, if convergent they will converge to the weak solution, while non-conservative methods will converge to an unphysical solution. It thus becomes apparent that for problems where discontinuities can arise, conservation laws and schemes are decisive in obtaining a physically correct solution.

In a technical report, Richtmyer (1962) presents the two-step Lax-Wendroff

method which, compared to its counterpart, eliminated the necessity of the explicit calculation of the Jacobian matrix. In a centred difference approach, illustrated in figure 2.4, this takes the form:

$$\begin{cases} U_{i+\frac{1}{2}}^{n+\frac{1}{2}} = \frac{1}{2}\left(U_{i+1}^{n} + U_{i-1}^{n}\right) - \frac{\Delta t}{2\Delta x}\left[F(U_{i+1}^{n}) - F(U_{i-1}^{n})\right], \\ U_{i}^{n+1} = U_{i}^{n} - \frac{\Delta t}{\Delta x}\left[F(U_{i+\frac{1}{2}}^{n+\frac{1}{2}}) - F(U_{i-\frac{1}{2}}^{n+\frac{1}{2}})\right]. \end{cases} \tag{2.55}$$

which represents the numerical approximation of Eq. (2.51) in one-space-dimension.

The intermediate time step $n+\frac{1}{2}$ evaluated at the grid points $i+\frac{1}{2}$, is calculated by a Lax-Friedrich spatial discretisation which is first-order accurate. A leapfrog central-difference-in-time is applied in the second step, with which second-order accuracy is achieved by updating the value using data from the n^{th} and the $n+\frac{1}{2}$ steps. Therefore, a time- and space-centred integration formula is obtained in the full step of the calculation.

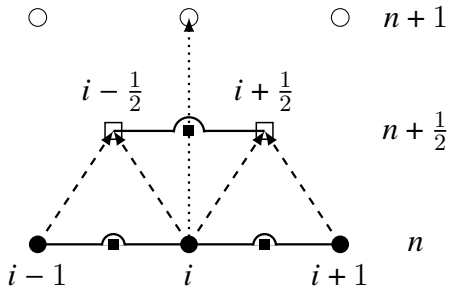

FIGURE 2.4: One-dimensional spatio-temporal mesh for the Lax-Wendroff scheme.

2.9.1 Stability

The measure of stability established therein is given in terms of the Courant-Friedrich-Lewy (CFL) condition which imposes a physical restriction on the propagation of information advected with the fluid.

$$\lambda_{max}\frac{\Delta t}{\Delta x} \leq 1 \tag{2.56}$$

where the $\lambda_{max} = \max_{m}(|\lambda^{m}|)$ defines the maximum wave propagation speed (eigenvalue). This falls from consideration of the von-Neumann stability analysis where for a Fourier mode $\exp(ik\Delta x)$ the amplification matrix defined by Eq. (2.55) is (Richtmyer and Morton, 1967):

$$\mathcal{G} = I - i\frac{\Delta t}{\Delta x}A\sin(k\Delta x) - \left(\frac{\Delta t}{\Delta x}A\right)^{2}(1-\cos(k\Delta x)).$$

Then, with λ being an eigenvalue of A, the corresponding eigenvalue of $\mathcal{G}$ is

$$g = 1 - ia\sin(k\Delta x) - a^2(1 - \cos(k\Delta x)),$$

where $a = \lambda\frac{\Delta t}{\Delta x}$. Hence, the magnitude of the amplification factor in the complex plain is given by

$$|g|^2 = 1 - a^2(1 - a^2)(1 - \cos(k\Delta x)).$$

It is now clearly seen that for the two-step Lax-Wendroff method the von-Neumann condition will be satisfied for all wavenumbers k when $a^2 \leq 1$. In relation to the FVM the CFL number ensures that the information propagated through in one time step does not exceed one grid cell, which otherwise would correspond to unphysical speeds and the rise of numerical instabilities. As highlighted by LeVeque (2002, p. 69) and Durran (2010, pp. 98–100) the CFL condition dictates the interdependence of the numerical domain with the associated PDE. Although CFL is a necessary condition for stability the sufficient conditions for stability may be more restrictive and one should refer back to the von Neumann stability analysis.

2.9.2 TVD schemes and the oscillatory behaviour near shocks

The two-step Lax-Wendroff method developed by Richtmyer (1962) and Richtmyer and Morton (1967) and further demonstrated by Potter (1973) and Vesely (2001), is tested in terms of its stability and compared against various schemes for hyperbolic problems by Toro (2001), LeVeque (2002) and Durran (2010). In specific, the discussion is focused around discontinuous solutions. First, an overview of first-order accuracy schemes is carried out where it is shown that schemes such as Godunov's or Lax-Friedrich's introduce numerical diffusion, resulting in poor accuracy. For smooth solutions good accuracy can be achieved with the use of second-order schemes such as the Lax-Wendroff, the Beam-Warming or Fromm's method which though, being dispersive, produce spurious oscillations to discontinuities. Techniques introduced to improve these oscillations are flux- and slope-limiters or MUSCL (Monotone Upstream-centred Scheme for Conservation Laws) -type of schemes. The class of flux-limiter schemes aims to combine features of the first- and second-order accuracy schemes by means of lowering the numerical accuracy in regions where shocks develop but retaining second-order in smooth parts of the solution. The MUSCL schemes aim to mimic the exact solutions of conservation laws by reconstructing the data in the shock vicinity so as to avoid spurious oscillations. Convergence of both methods is analysed examining their TVD (or TVNI) properties (Harten, 1983), which ensures that

independently of the data reconstruction technique employed, the scheme preserves monotonicity.

Utilising flux-limiter or polynomial-reconstruction-limiter can be advantageous for the numerical approximations of problems ensuring convergence even in the presence of shocks or discontinuous solutions. Nevertheless, use of these techniques can significantly hinder solutions to smooth extrema introducing errors to the computation as they degenerate to first-order accuracy at extremal points. Moreover, all limiter approaches impair the computational efficiency. Consequently, it stands to reason that whence limiters are not essential for the correct simulation of the underlying physics, to be avoided. A synopsis of such methods has been given in §2.9, and can be found in more detail in (Zhang et al., 2015; Toro, 2001; LeVeque, 2002) but are generally beyond the scope of this thesis.

As mentioned above, although the Lax-Wendroff method exhibits oscillations near shocks, it still captures accurately their steepness. Adjusting the CFL condition (i.e. the temporal- and/or the spatial-step) one can regulate the oscillations minimising the dispersion effects displayed (Potter, 1973, p. 269). Such an example can be seen in Hesthaven (2017, p. 119) where the CFL is adjusted in terms of its temporal discretisation. In fact, it is indicated in LeVeque (2002) that it owes to work best when the CFL equals unity.

Chapter 3

Numerical schemes and solvers

This chapter reviews the 2D Lax-Wendroff-Richtmyer scheme before proceeding to present a new and improved spatiotemporal integration scheme used for the evolution of the system of equations. The latter is coupled with a highly-efficient Poisson solver employing the tridiagonal matrix algorithm and fast discrete cosine transform used in solving the interfacial pressure and electric potential equations.

3.1 2D Lax-Wendroff scheme

The Richtmyer-Lax-Wendroff scheme is presented in two-spatial dimensions before developing the new two-dimensional scheme utilising the rhombic structure of the grids. In the latter parts of this chapter, an efficient fast Poisson solver for the 2D finite-difference elliptic equations is developed, which is applied in the numerical resolution of the 2D two-layer pressure, as well as the electric potential equation.

In two-spatial dimensions, a conservative hyperbolic equation can be written as:

$$\partial_t \mathbf{U} + \partial_x \mathbf{F}(\mathbf{U}) + \partial_y \mathbf{G}(\mathbf{U}) = 0. \tag{3.1}$$

where $\mathbf{F}(\mathbf{U})$ and $\mathbf{G}(\mathbf{U})$ are the fluxes of the quantity $\mathbf{U}$ in the x and y direction respectively. In presenting the numerical scheme, in two-dimensional spatial-variables, the index notation will be temporarily altered from that of §2.9 to accommodate the needs for the description of the scheme as per Richtmyer (1962) and Richtmyer and Morton (1967). As such, the fractional indices are replaced by integer indices; $t = (n+1)\Delta t$ refers to the predictor step whereas $t = (n+2)\Delta t$ to the corrector step and the following scheme is applied on all $(i, j) : i, j \in \mathbb{Z}$ nodes.

$$\begin{cases} U_{i,j}^{n+1} = \hat{U}_{i,j}^{n} - \dfrac{\Delta t}{2\Delta x}\left[F(U_{i+1,j}^{n}) - F(U_{i-1,j}^{n})\right] - \dfrac{\Delta t}{2\Delta y}\left[G(U_{i,j+1}^{n}) - G(U_{i,j-1}^{n})\right], & \text{(3.2a)} \\ \qquad \text{where } \hat{U}_{i,j}^{n} = \dfrac{1}{4}\left(U_{i+1,j}^{n} + U_{i-1,j}^{n} + U_{i,j+1}^{n} + U_{i,j-1}^{n}\right) \\ U_{i,j}^{n+2} = U_{i,j}^{n} - \dfrac{\Delta t}{\Delta x}\left[F(U_{i+1,j}^{n+1}) - F(U_{i-1,j}^{n+1})\right] - \dfrac{\Delta t}{\Delta y}\left[G(U_{i,j+1}^{n+1}) - G(U_{i,j-1}^{n+1})\right]. & \text{(3.2b)} \end{cases}$$

In the implementation of the Richtmyer two-step Lax-Wendroff scheme, the nine-point-stencil used is portrayed in figure 3.1a whereas the spatial grid considered is presented in figure 3.1b.

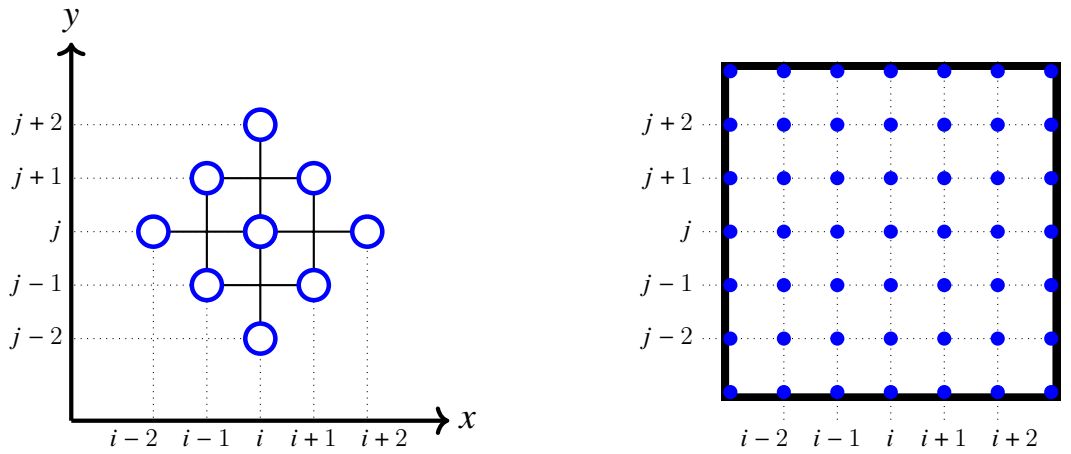

(a) 2D Lax-Wendroff stencil.

(b) Spatial grid points.

FIGURE 3.1: The nine-point stencil 3.1a and the grid 3.1b for the Lax-Wendroff scheme

As mentioned by Richtmyer and Morton (1967), in application of Eq. (3.2) on figure 3.1b the set of points with $n + i + j$ being even and the set having odd values are decoupled which induces a "drift" in the solution, between the two stencils, over time as mentioned by Vesely (2001). It has been suggested by Vesely (2001) and Potter (1973) that a diffusion term in the equations or one artificially implemented would mutually couple the grids.

The decoupling in Richtmyer's implementation can be better understood in application of the nine-point stencil on the grid for two neighbouring points. At this stage, it is also advantageous to return to the fractional notation, in both Eq. (3.2) and figure 3.1, for comparison with the scheme naturally following from Richtmyer's scheme. Hence, the grid, illustrated in figure 3.1b, with the nine-point stencils applied takes the following form:

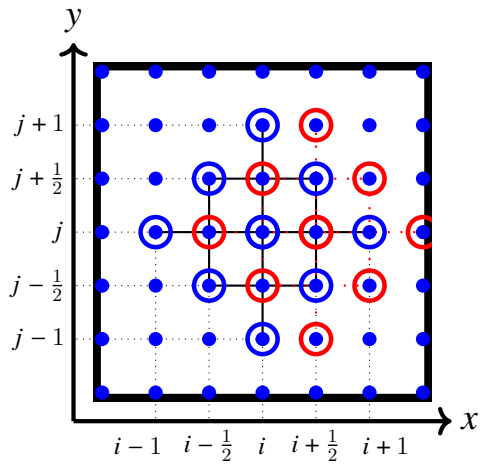

FIGURE 3.2: Grid with two neighbouring points' stencil.

In this thesis, no diffusion term is considered and since the solutions on the two grids are decoupled they thus are mutually independent. Therefore, it is possible to define two conjugate grids as shown in figure 3.3.

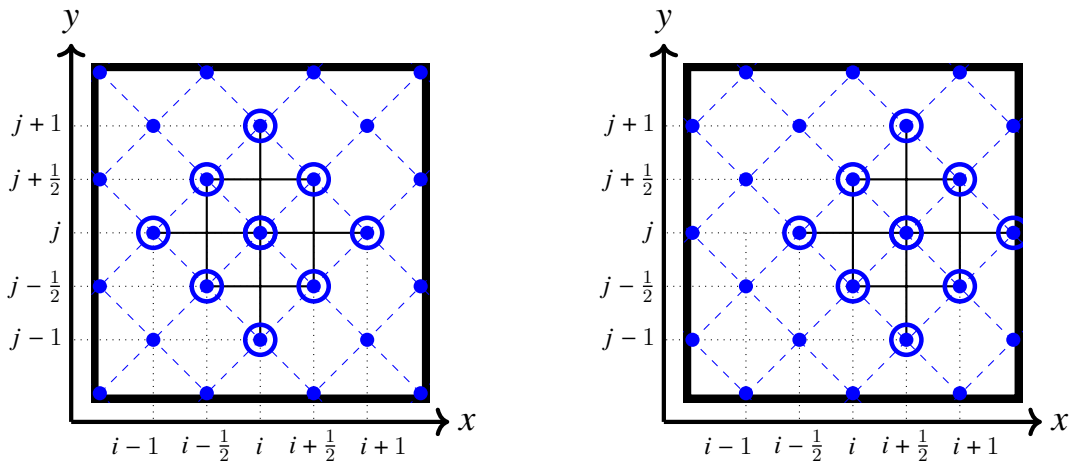

(a) Staggered grid (b) Conjugate staggered grid

FIGURE 3.3: Two configurations of the rhombic staggered grid

In these two configurations, let $\mathcal{V}_1$ be the graph indicated in figure 3.3a whereas $\mathcal{V}_2$ the graph of figure 3.3b, where the vertices of the corresponding graphs write as:

$$\begin{cases} \mathcal{V}_1 := \left\{ \left(i + \dfrac{\sigma}{2}, j + \dfrac{\sigma'}{2} \right) : (\forall\, i, j \in \mathcal{Z}) \wedge (\forall\, \sigma, \sigma' \in \{0,1\}) : \sigma + \sigma' \in \{0,2\} \right\}, & \text{(3.3a)} \\ \mathcal{V}_2 := \left\{ \left(i + \dfrac{\sigma}{2}, j + \dfrac{1-\sigma}{2} \right) : (\forall\, i, j \in \mathcal{Z}) \wedge \sigma\, \{0,1\} \right\}. & \text{(3.3b)} \end{cases}$$

As it can be seen in the computational domain under consideration, the resulting uniformly spaced quadrangle elements form rhombic ("diamond"-shaped) elements. This particular choice of representation lies in the accurate interpretation of the control-volumes. The orientation of the quadrangles allow no overlapping spaces which otherwise would arise as a result of rectangular quadrangles i.e. the rhombic-shaped elements rotated by 45°.

For the numerical integration of the cell-vertex quadratures, the Newton-Cotes formulas are used. The whole volume is described as $\Omega = \bigcup_{i=1}^{4} \Omega_i$ where each quadrature is $|\Omega_i| = \frac{|\Omega|}{4}$ for $i = 1 \dots 4$ and they are not overlapping i.e. $\Omega_i \bigcap \Omega_j = \emptyset,\ \forall i \neq j$. The centre position q is $q = \frac{\mathbf{x}_1+\mathbf{x}_2+\mathbf{x}_3+\mathbf{x}_4}{4}$ and an approximation of the integral over the domain Ω is obtained via the Newton-Cotes formula as:

$$\int_{\Omega} f(\mathbf{x}) d\Omega \approx \sum_{i=1}^{4} \Omega_i f(x_i) \approx |\Omega|\ q$$

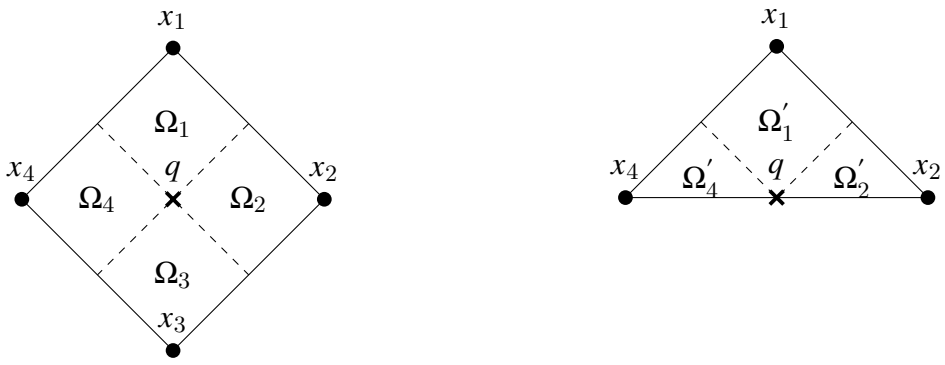

(a) Volume (b) Volume at the boundary

FIGURE 3.4: Cell-vertex FV

At the boundary: $|\Omega_1^{'}| = |\Omega_1|$ and $|\Omega_{2,4}^{'}| = \frac{|\Omega_1^{'}|}{2} = \frac{|\Omega_{2,4}|}{2}$. Therefore, Newton-Cotes formula reads as:

$$\int_{\Omega'} f(\mathbf{x}) d\Omega^{'} \approx |\Omega_1^{'}|\mathbf{x}_1 + |\Omega_2^{'}|\mathbf{x}_2 + |\Omega_4^{'}|\mathbf{x}_4 = \frac{2|\Omega_1|\mathbf{x}_1 + |\Omega_2|\mathbf{x}_2 + |\Omega_4|\mathbf{x}_4}{2} = \frac{|\Omega|}{4}\frac{2\mathbf{x}_1 + \mathbf{x}_2 + \mathbf{x}_4}{2}$$

Hence, in relation to the inner volume it can be seen that $|\Omega^{'}| = \frac{|\Omega|}{2}$, thus the point q is defined as $q = \frac{2\mathbf{x}_1+\mathbf{x}_2+\mathbf{x}_4}{4}$ on Γ. In review of Eqs. (2.46) and (2.50) and retrieving the fractional notation, Richtmyer's two-step scheme, applied on figure 3.3a with vertices defined by Eq. (3.3a), can be represented as:

$$\begin{cases} U^{n+\frac{1}{2}}_{i,j+\frac{1}{2}} = \hat{U}^{n}_{i,j+\frac{1}{2}} - \dfrac{\Delta t}{2\Delta x}\left[F(U^{n}_{i+1,j}) - F(U^{n}_{i-1,j})\right] - \dfrac{\Delta t}{2\Delta y}\left[G(U^{n}_{i,j+1}) - G(U^{n}_{i,j-1})\right], & \text{(3.4a)} \\ \qquad\qquad \text{where } \hat{U}^{n}_{i,j+\frac{1}{2}} = \dfrac{1}{4}\left(U^{n}_{i+1,j} + U^{n}_{i-1,j} + U^{n}_{i,j+1} + U^{n}_{i,j-1}\right) \\ U^{n+1}_{i,j} = U^{n}_{i,j} - \dfrac{\Delta t}{\Delta x}\left[F(U^{n+1}_{i+\frac{1}{2},j}) - F(U^{n+1}_{i-\frac{1}{2},j})\right] - \dfrac{\Delta t}{\Delta y}\left[G(U^{n+1}_{i,j+\frac{1}{2}}) - G(U^{n+1}_{i,j-\frac{1}{2}})\right]. & \text{(3.4b)} \end{cases}$$

where the corrector step Eq. (3.4b) applies to the nodes represented by the blue dots and the predictor step Eq. (3.4a) to the red crosses which are the nodes of $\mathcal{V}_2$ on the conjugate grid. The grids formed by circles and crosses in figure 3.5, indicate the spatial configuration of the time-discretisation of the half time step Eq. (3.4a) and the full time step Eq. (3.4b) points, respectively. The new computational grid encompasses two staggered subgrids, which comprise a numerical analogue of the finite volume scheme where every element (conserved quantity) is being enclosed at the centre of the computational cell, and requires four grids (two for each step) to be computed.

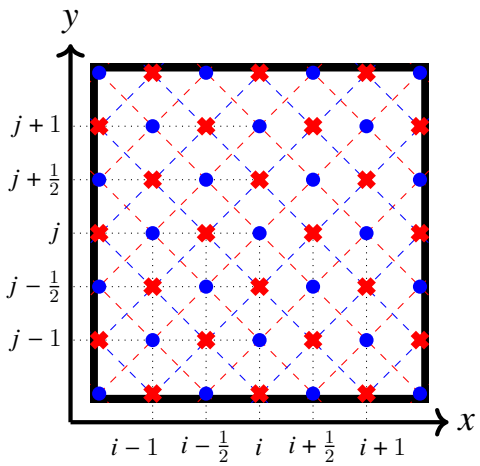

FIGURE 3.5: Dual-rhombic computational grid. Half-step: (✖). Full-step: (●)

According to the stability analysis carried out by Richtmyer and Morton (1967) the stability conditions of this scheme is:

$$\lambda_{max}\frac{\Delta t}{\Delta x} \leq \frac{1}{\sqrt{2}},$$

where λ_{max} is the norm of the maximum eigenvalues in both directions where equal discretisation ($\Delta x = \Delta y$) has been considered. A thorough stability analysis of both the two- and three-dimensional Richtmyer-type schemes is also carried out by Wilson (1972). Detailed discussions of alternative discretisations can be found also in Burstein (1967), Zwas (1972) and Eilon et al. (1972) from which it is understood that arrangement of nodes in space and time may significantly affect the computational accuracy and the stability conditions.

3.2 Development of a highly-efficient Poisson solver

For two-layer systems with electromagnetic effects, additional terms arise on the RHS of the governing equation. Numerical evaluation of these terms requires the computation of elliptic equations which are not present when solving incompressible hydrodynamic single-fluid flows for which the aforementioned Lax-Wendroff scheme is sufficient for the study of the problem. Numerical modelling of the two-layer shallow-water MHD system of equations necessitates at every time step the resolution of elliptic equations describing the pressure at the interface between the fluid layers as well as the electric potential distributions. In both cases the solution of diagonally dominant tridiagonal linear systems of equations is required. The challenge is then to acquire a solver which is computationally efficient and second-order accurate.

As shown in §2.7, the rigid-lid condition gives rise to an elliptic pressure equation, Eq. (2.41), for interfacial pressure which in the Boussinesq approximation reduces to a Poisson equation. In the case of a second-order finite difference approximation of the Laplacian, this results in a system of linear equations with a constant-coefficient matrix of coefficients, within which the boundary conditions are incorporated.

However, Eq. (5.7) associated with the electromagnetic part of the problem, as seen in §5, is essentially nonlinear and requires particular attention as a time varying height term is involved on the LHS. Aiming towards a memory efficient and computationally-fast direct solver, a methodology similar to Chorin's projection scheme (Chorin, 1968) was employed where at each time step an effectively linear constant-coefficient problem is formulated. The method is described in the succeeding section.

3.2.1 Time-splitting projection method

As mentioned in the introduction, similarly to the Navier-Stokes equation, for which Chorin's projection method was originally developed, several Poisson equations must be solved numerically at each time step which is computationally expensive. Consequently, considerable research has been devoted to the development of direct fast Poisson solvers, based on the Fast Fourier Transforms (FFT) in combination with the Gaussian elimination.

Notwithstanding the efficiency brought by fast Poisson solvers the solution from time t^n to t^{n+1} of Eq. (5.7) involves time dependent coefficients which preclude the direct use of fast Poisson solvers. In order to solve a variable coefficient

equation as in Eq. (5.7), iterative multigrid methods are commonly used. The main disadvantage of iterative methods is their high computational inefficiency, especially in comparison to the fast Poisson solvers which though, are limited to constant-coefficient equations.

Dong and Shen (2012), have developed a projection method that reduces the elliptic equation into a constant-coefficient equation. Whereas their implementation is applied on a variable-coefficient pressure-gradient with variable density; adopting this approach it is possible to split the variable-coefficient potential-gradient term into a constant term and a variable term, and then treat the constant term implicitly and the variable term explicitly. The flux in Eq. (5.7) can be split approximately as:

$$\bar{h}\nabla\phi^{n+1} + \left(h^{n+1} - \bar{h}\right)\nabla\hat{\phi}\,,$$

where $\hat{\phi}$ defines an extrapolation of the potential to the time-step $n+1$. Dong and Shen (2012) define this term as:

$$\hat{\phi} = \begin{cases} \phi^{n}. & \text{(3.5a)} \\ 2\phi^{n} - \phi^{n-1}. & \text{(3.5b)} \end{cases}$$

where Eq. (3.5a) and Eq. (3.5b) define a constant and linear extrapolation resulting in a first and second order accurate approximations. For the Lax-Wendroff scheme, flux can be split as:

- Half-step: $O(\tau)$

$$h^{n+\frac{1}{2}}\nabla\phi^{n+\frac{1}{2}} = \left(\bar{h} + \left(h^{n+\frac{1}{2}} - \bar{h}\right)\right)\nabla\phi^{n+\frac{1}{2}} = \bar{h}\nabla\phi^{n+\frac{1}{2}} + \left(h^{n+\frac{1}{2}} - \bar{h}\right)\nabla\phi^{n}. \quad (3.6)$$

- Full-step: $O(\tau^2)$

$$h^{n+1}\nabla\phi^{n+1} = \bar{h}\nabla\phi^{n+1} + \left(h^{n+1} - \bar{h}\right)\nabla\left(2\phi^{n+\frac{1}{2}} - \phi^{n}\right). \quad (3.7)$$

Since after the splitting all nonlinear terms are defined on the previous time steps and thus moved to the RHS of the equation, the finite-difference potential equation effectively reduces to a Poisson equation which is solvable by a fast algorithm.

3.2.2 The DCT and TDMA algorithms

Approximating the Poisson equation in one-dimension with the second order finite difference:

$$\frac{\partial^2 w}{\partial x^2} \approx \frac{w_{i+1} - 2w_i + w_{i-1}}{\Delta x^2},$$

results in a set of linear algebraic equations of the form

$$Aw = f, \tag{3.8}$$

with the matrix A defined by:

$$\begin{bmatrix} -d_i\ w_i & +b\ w_{i+1} & \\ w_{i-1} & -d_i w_i & +w_{i+1} \\ & b\ w_{i-1} & -d\ w_i \end{bmatrix} = \begin{bmatrix} \vdots \\ f_i \\ \vdots \end{bmatrix} \begin{matrix} \\ i = 1, N-1, \\ \end{matrix} \begin{matrix} i = 0, \\ \\ i = N. \end{matrix} \tag{3.9}$$

where first and last equations approximate Neumann boundary conditions which in general are defined by the coefficients $[d, b]$. These coefficients depend on the grid as defined in the following figures.

(a) Grid 0. (b) Grid 1.

FIGURE 3.6: Two different 1D grids with midpoints: (✖) and nodes: (●)

The two natural choices falling from the second order FD approximation of the Neumann boundary condition

$$\partial_n w_{|\Gamma} = 0,$$

define symmetry around a meshpoint fig. 3.6a, or around a midpoint fig. 3.6b and formulate the coefficients of Eq. (3.9) as $\left[d_{1,N} = 2, b = 2\right]$ or $\left[d_{1,N} = 1, b = 1\right]$, respectively.

The Discrete Cosine Transform

The discrete cosine transform (DCT) is a form of the discrete Fourier transform, first defined by Ahmed et al. (1974). It transforms the matrix from the spatial domain to the frequency domain into spectral sub-bands of differing importance.

Equation (3.9) can be solved using a DCT the type of which depends on the location of the boundary. Let $\hat{w}_j$ denote the DCT whereas w_i is the inverse DCT. Then, for the case which $\left[d_{1,N} = 2, b = 2\right]$ corresponding to figure 3.6a, the one-dimensional DCT commonly referred to as DCT-I is:

$$\hat{w}_j = \left(\frac{2}{N}\right)^{\frac{1}{2}} \sum_{i=0}^{N} \frac{(1 + \delta_{i0} + \delta_{iN})^{-\frac{1}{2}}}{(1 + \delta_{j0} + \delta_{jN})^{\frac{1}{2}}} \cos\left(\frac{\pi j i}{N}\right) f_i, \quad \text{for} \quad 0 \le i, j \le N, \tag{3.10}$$

Application of the DCT onto the discrete Poisson system Eq. (3.9) results to eigenvalues, the form of which depends on the boundary conditions. The corresponding eigenvalues in application of DCT-I are:

$$\lambda_j = 2\left(\cos\left(\frac{\pi j}{N}\right) - 1\right) = -4\sin^2\left(\frac{\pi j}{2N}\right). \tag{3.11}$$

The associated inverse DCT w_i is defined by a similar expression, replacing f_i with $\hat{w}_j$ and summing over the index j.

The analogous Fourier transform for figure 3.6b with coefficients $\left[d_{1,N} = 1, b = 1\right]$ is DCT-II which reads as:

$$\hat{w}_j = \left(\frac{2}{N}\right)^{\frac{1}{2}} \sum_{i=0}^{N} \frac{1}{\sqrt{1+\delta_{j0}}} \cos\left(\frac{\pi i\left(j+\frac{1}{2}\right)}{N+1}\right) f_i, \quad \text{for} \quad 0 \le i, j \le N, \tag{3.12}$$

with the corresponding eigenvalues being given by:

$$\lambda_j = 2\left(\cos\left(\frac{\pi j}{N+1}\right) - 1\right) = -4\sin^2\left(\frac{\pi j}{2\left(N+1\right)}\right). \tag{3.13}$$

The respective inverse of DCT-II (IDCT-II) is equivalent to DCT-III. That is:

$$w_i = \left(\frac{2}{N}\right)^{\frac{1}{2}} \sum_{j=0}^{N} \frac{1}{\sqrt{1+\delta_{i0}}} \cos\left(\frac{\pi i\left(j+\frac{1}{2}\right)}{N+1}\right) \hat{w}_j, \quad \text{for} \quad 0 \le i, j \le N. \tag{3.14}$$

Tridiagonal Matrix Algorithm (Thomas Algorithm)

The Tridiagonal Matrix Algorithm (TDMA), first described by Thomas (1949), is commonly referred to as the Thomas algorithm. Thomas algorithm is a simple and efficient form of Gaussian elimination which makes use of the tridiagonal banded structure of matrix systems to solve N equations using $O(N)$ operations. In this tridiagonal structure, all matrix elements other than the central-, the super- and the sub-diagonal, are zero. The Thomas algorithm reduces the system of equations to upper triangular form, by eliminating recursively terms in each of the equations, followed by backward substitution starting with the last equation as follows:

$$\begin{cases} w_{i+1} = a_i w_i + c_i \,, & \text{(3.15a)} \\ w_i = a_i^{-1}\left(w_{i+1} - c_i\right). & \text{(3.15b)} \end{cases}$$

For Eq. (3.9), the forward sweep for $i = 0$ yields:

$$a_0 = \frac{d_0}{b_0} \qquad \text{and} \qquad c_0 = \frac{f_0}{b_0}.$$

Accordingly, for $i = 1, \ldots, N-1$ the recurrence relations falling from the use of Eq. (3.15) are

$$a_i = d_i - a_{i-1}^{-1} \qquad \text{and} \qquad c_i = a_{i-1}^{-1} c_{i-1} + f_i.$$

The resulting upper bidiagonal matrix is now solved starting from the last element $i = N$ for which

$$w_N = \frac{b_n}{d_N} w_{N-1} - \frac{f_n}{d_N},$$

where using Eq. (3.15b) it rewrites into

$$w_N = \frac{b_n}{d_N} a_{N-1}^{-1} \left(w_N - c_{N-1}\right) - \frac{f_n}{d_N} = -\frac{a_{N-1}^{-1} c_{N-1} + \frac{f_N}{b_N}}{\frac{d_N}{b_N} - a_{N-1}^{-1}} = -\frac{c_N}{a_N}.$$

Implementation of the Neumann boundary conditions in the tridiagonal system results into a singular matrix which in turn affects the solution with the use of the Thomas algorithm. This problem is overcome by setting $a_N = 1$ which embodies the solvability condition.

In this work, the Thomas algorithm is used with two sets of coefficients $\left[d_{1,N} = 1,\ b = 1\right]$ and $\left[d_{1,N} = 2,\ b = 2\right]$ and will be referred to as TDMA-I and TDMA-II respectively.

3.2.3 The DCT-TDMA algorithm

The proposed scheme is akin to the idea of the Fourier-analysis-cyclic-reduction (FACR) algorithm described by Swarztrauber (1977) and Press et al. (2007), which uses the 1D discrete Fourier transform to separate the original system of linear equations into tridiagonal systems for each Fourier mode. Furthermore, Wilhelmson and Ericksen (1977), Swarztrauber (1977) and Swarztrauber (1986) studied the FACR algorithm for staggered and nonstaggered grids with the respective Neumann as well as Dirichlet boundary conditions.

The *DCT-TDMA* method consists of a combination of the Discrete Cosine Transform and the Tridiagonal Matrix (Thomas) Algorithm, where the two-dimensional Poisson equation is transformed into the Fourier space along the y-direction, resulting in a tridiagonal system for each y-Fourier mode along the x-direction. Although the implementation of the scheme is much simpler than that of other Poisson solvers, the only instance in literature where such a scheme is mentioned is Hasbestan and Senocak (2018) and Hasbestan and Senocak (2019) in which the study pertains numerical solution to the three-dimensional Poisson equation as well as comparisons with the cyclic-reduction algorithm. Counter to

the proposed scheme in this thesis, only one grid configuration is considered for the Neumann boundary condition.

The computational efficiency of the Thomas versus cyclic-reduction algorithm is shown to be comparable by (Hasbestan and Senocak, 2019). Assuming a constant-coefficient problem, the overall efficiency could further be improved, reducing the necessary operations per time step by calculating the Thomas algorithm coefficients once at the beginning. The resulting algorithm requires $4(N-1)+1$ operations per time-step as opposed to $6(N-1)+4$ (see pseudo-algorithms in A).

The Poisson equation is solved by application of the eigenfunction expansion method on the 2D system $Aw = f$. Let Q denote the matrix consisting of eigenvectors of A and thus the diagonal matrix comprised of eigenvalues being given by $Q^{-1}AQ = \mathrm{diag}(\lambda_i)$ where λ_i depend on the boundary conditions which are satisfied in each basis function. Then, defining the Fourier transform $\hat{w} = Q^{-1}w$ and computing $\hat{f} = Q^{-1}f$ the eigendecomposition of the discrete Laplacian operator yields:

$$\hat{w}_{i-1,j} - Q^{-1}AQ\hat{w}_{i,j} + \hat{w}_{i+1,j} = \hat{f}_{i,j}.$$

where $i,\ j$ indicate the j^{th} component of the i^{th} eigenvector. Bearing in mind that the eigenfunctions $\psi_{i,j}$ applied to the system

$$\left(\hat{w}, \hat{f}\right)_j = \sum_{i=0}^{N} (w, f)_i \, \psi_{i,j}$$

are composed of sine and cosine functions the system is then recast as:

$$(\lambda_i \mathbf{I} - A)\, \hat{w}_{i,j} = \hat{f}_{i,j},$$

which is a tridiagonal system of linear equations solved with the use of the Thomas algorithm. Lastly the solution of w is obtained by the inverse Fourier transform as follows:

$$(w, f)_i = \sum_{j=0}^{N} \left(\hat{w}, \hat{f}\right)_j \psi_{i,j}$$

In application of the DCT the coefficients $(\lambda_i \mathbf{I} - A)$ of the tridiagonal system now take the form:

$$\begin{bmatrix} d'_1 & b \cdots 0 \\ 1 & d'_i & 1 \\ 0 \cdots b & & d'_N \end{bmatrix}.$$

These coefficients, which depend on the boundary conditions, are given by $d'_i = -\left(d_i + \lambda_j \frac{\Delta x^2}{\Delta y^2}\right)$, where d_i is defined as

$$d_i = \begin{cases} b & \text{for} \quad j = 0 \quad \text{and} \quad i = N, & \text{(3.16a)} \\ -2 & \text{for} \quad j = 1, \ldots, N-1, & \text{(3.16b)} \end{cases}$$

and b is defined by the use of the analogous staggered or collocated grid. The corresponding eigenvalues read as:

$$\lambda_j = -4 \sin^2 \theta_j \quad \text{for} \quad j = 0, \ldots, N, \tag{3.17}$$

where

$$\theta_j = \begin{cases} \dfrac{\pi\ j}{2N}, & \text{collocated grid,} & \text{(3.18a)} \\ \dfrac{\pi\ j}{2\,(N+1)}, & \text{staggered grid.} & \text{(3.18b)} \end{cases}$$

The solution of the Poisson equation on the staggered grids presented in §3.1 decouples into four independent solutions on four different sub-grids which require a different combination of the DCTs and TDMAs previously presented.

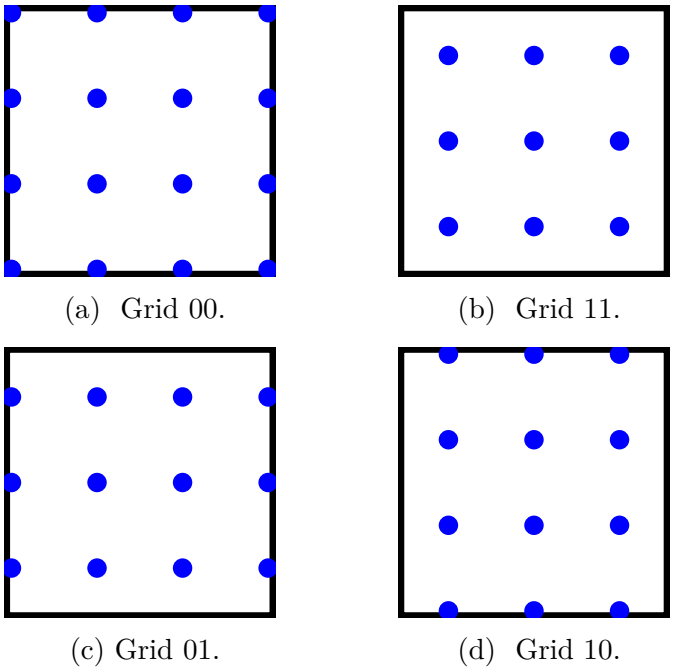

(a) Grid 00. (b) Grid 11.

(c) Grid 01. (d) Grid 10.

FIGURE 3.7: Visual representation of the 2D matrices domain of reference decomposed into different grids.

In the case of the grid presented in figure 3.7a the DCT-II/TDMA-I is required, while the grid presented in figure 3.7b requires application of DCT-I/TDMA-II. In both cases the same type of staggered/collocated conditions are applied in both directions. The other two cases illustrated in figure 3.7c and figure 3.7d require

the use of DCT-II/TDMA-II and DCT-I/TDMA-I, respectively. The subsequent time-cost efficiency in function of the grid size is given in figure 3.8:

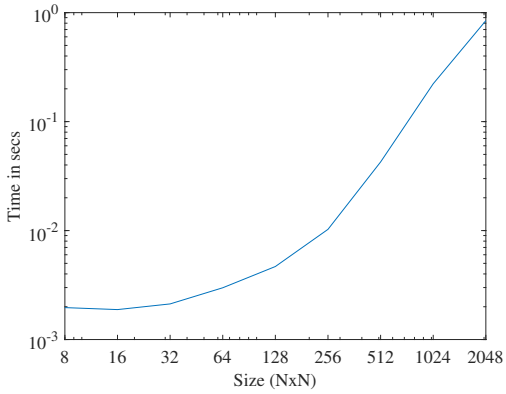

FIGURE 3.8: Illustration of the combined performance of the four types of Poisson solvers against the matrix size.

Chapter 4

1D two-layer SW system bounded by a rigid lid

In this chapter the analysis and numerical modelling of interfacial waves with hydraulic jumps is carried through with the use of a new theoretical framework which was proposed by (Priede, 2018). Bound by a rigid lid, the two-layer shallow-water system is formulated with the use of a completely self-contained conservative form of momentum equation that does not require external closure conditions.

In §4.1 the constituent theory of the two-layer model is reviewed. The Boussinesq lock-exchange problem is closed analytically in §4.2 and validated numerically in §4.2.5 where the new analytic results as well as numerical aspects of the problem are discussed and results are illustrated.

4.1 Conservative shallow-water equations for the 1D system

The objective of §4.1.1 and §4.1.2 is to present a new set of conservative equations for the two-layer system as proposed by Priede (2018). The apparent absence of equations, in the case of a bilayer system, capable of encapsulating discontinuities that inevitably arise under the admission of the shallow-water approximation has lead to the belief that the system is inherently non-conservative and thus unable to describe such solutions without external closure relations. Counter to common belief, Priede (2018) shows that the two-layered system admits to a conservative and self-contained form of the momentum equation which does not require external energy considerations for closure.

4.1.1 Basic equations

As noted in §2.6 and §2.7 the fluid flow is assumed to be predominantly horizontal and has a negligible effect on the vertical pressure distribution. Hence, in the first-order shallow-water approximation, the pressure distribution is purely hydrostatic, i.e.

$$p_{\pm}(x,z,t) = \Pi(x,t) - \rho_{\pm} g(z - h(x,t)).$$

Congruous to §2.7, the plus and minus subscripts refer to the bottom and top layer. In contrast to Baines (1984) and Milewski (2004), and similarly to Long (1956b), Wood and Simpson (1984) and Sandstrom and Quon (1993) the pressure distribution $\Pi(x,t) = p_{\pm}(x,z,t)|_{z=h}$ is defined at the interface. Substituting this pressure distribution into the inviscid fluid flow (Euler) equation for the horizontal velocity component in each layer yields the first shallow-water equation, while the second equation follows from the conservation of mass in each layer Pedlosky (1979)

$$\rho(u_t + uu_x \pm g h_x) = -\Pi_x, \tag{4.1}$$

$$h_t - (uh)_x = 0, \tag{4.2}$$

where ϱ is the density, u the velocity and h the height of the respective layers. Hereafter, subscripts t and x denote the respective temporal and spatial partial derivatives while the plus and minus indices have been dropped for the sake of brevity.

In terms of the flux $U = hu$, Eq. (4.1) is written as:

$$\varrho\left(\frac{U}{h}\right)_t + \frac{\varrho}{2}\left(\frac{U^2}{h^2}\right)_x \pm g\varrho(h)_x = -\Pi_x. \tag{4.3}$$

Lastly, the integral/weak formulation of Eq. (4.1) is obtained by integrating over the depth of the respective layers:

$$\varrho\left(U_t + \left(\frac{U^2}{h}\right)_x \pm \frac{g}{2}\left(h^2\right)_x\right) = -h\Pi_x. \tag{4.4}$$

The system of four shallow-water Eqs. (4.2) and (4.4) contains five unknowns: $u_{\pm}$, $h_{\pm}$ and Π. It is closed by the rigid-lid approximation (fixed total height $h_+ + h_- = H$) condition, which can be used to eliminate the top layer depth.

4.1.2 Circulation and Momentum conservation laws

Two more unknowns can be eliminated from Eqs. (4.1) and (4.4) by virtue of the mass conservation and the laterally closed domain which permit their algebraic

manipulation in order to obtain a set of locally conservative equations. The pressure gradient Π_x can be eliminated by subtracting Eq. (4.3) for the top layer from that for the bottom layer. This leaves only two unknowns, $U \equiv u_+ h_+$ and $h = h_+$, and two equations, which can be written in a locally conservative form as

$$\left(\left\{\frac{\varrho}{h}\right\} U\right)_t + \frac{1}{2}\left(\left[\frac{\varrho}{h^2}\right] U^2\right)_x + g\,[\varrho]\,[h]_x = 0. \tag{4.5}$$

As discussed by Priede (2018), the locally conservative Eq. (4.5) may not be applicable to strong bores. The locally conserved quantity $\left(\left\{\frac{\varrho}{h}\right\} U\right)$ which can be written as $[\varrho u] = \int_H \partial_z(\varrho u)\, dz$, is closely related with the vorticity $\omega = \partial_z u$. As explained by Batchelor (2000, p. 508), vorticity is conserved in two-dimensional flows where vorticity is advected, but in three-dimensional flows $\omega.\nabla u$ can modify the vorticity balance, turning and extending the vortex. As such, jump conditions owing to Eq. (4.5) may not be applicable in hydraulic jumps as the relevant quantities should not only be conserved in one-dimensional flows defined by Eqs. (4.2) and (4.5) but also in the more complex three-dimensional turbulent flows taking place in strong bores.

The mass conservation for both layers leads to $\{uh\} = \Phi(t)$, where $\Phi(t)$ is the total flow rate. In a laterally closed channel $\Phi \equiv 0$ and thus $u_- h_- = -u_+ h_+$. A conservation law that will be conserved across hydraulic jumps is derived through a linear combination of the sum of the two layers of Eq. (4.3) and the respective difference, as seen in Eq. (4.5). Due to Eq. (4.5) being zero one obtains:

$$\left(\left[\frac{\varrho}{h}\right] U\right)_t + \frac{1}{2}\left(\left\{\frac{\varrho}{h^2}\right\} U^2\right)_x + g\{\varrho\}(h_+)_x = -2\Pi_x. \tag{4.6}$$

The summation of the two layers of Eq. (4.4) for both layers results in:

$$[\varrho]\, U_t + \left(\left\{\frac{\varrho}{h}\right\} U^2\right)_x + \frac{g}{2}\left[\varrho h^2\right]_x = -H\Pi_x. \tag{4.7}$$

Substituting the pressure gradient from Eq. (4.6) into Eq. (4.7) the momentum conservation equation is obtained as:

$$\left([\varrho]\, U - \frac{H}{2}\left[\frac{\varrho}{h}\right] U\right)_t + \left(\left\{\frac{\varrho}{h}\right\} U^2 - \frac{H}{4}\left\{\frac{\varrho}{h^2}\right\} U^2\right)_x + \frac{g}{2}\left(\left[\varrho h^2\right] - H\{\varrho\} h_+\right)_x = 0.$$

The last term of this equation can be further simplified using $\left[h^2\right] = H\,(2h_+ - H)$, which leads to:

$$\left([\varrho]\, U - \frac{H}{2}\left[\frac{\varrho}{h}\right] U\right)_t + \left(\left\{\frac{\varrho}{h}\right\} U^2 - \frac{H}{4}\left\{\frac{\varrho}{h^2}\right\} U^2\right)_x + g\frac{[\varrho]}{4}\{h^2\}_x = 0. \tag{4.8}$$

which is the sought locally conservative the momentum equation. This equation can straightforwardly be integrated across hydraulic jumps to obtain jump conditions analogous to the Rankine-Hugoniot relations.

4.1.3 Energy conservation equation

The local energy equation can be obtained using Eqs. (4.2) and (4.4). Hence, to obtain the kinetic energy we multiply throughout by the velocity u, leading to:

$$\varrho u\left((uh)_t + \left(u^2h\right)_x \pm \frac{g}{2}h^2{}_x\right) = -uh\Pi_x,$$

which writes as

$$\varrho\left(\left(u^2h\right)_t - uhu_t + \left(u^3h\right)_x - u^2h\,(u)_x \pm guhh_x\right) = -uh\Pi_x,$$

rewriting it so as to make use of Eq. (4.4)

$$\varrho\left(\left(u^2h\right)_t + \left(u^3h\right)_x - uh\left((uh)_t + \left(u^2h\right)_x \mp gh_x\right)\right) = -uh\Pi_x,$$

leads to

$$\varrho\left(\left(u^2h\right)_t + \left(u^3h\right)_x\right) - uh\left(-\Pi_x \mp 2\varrho gh_x\right) = -uh\Pi_x,$$

which simplifies to:

$$\varrho\left(\left(u^2h\right)_t + \left(u^3h\right)_x\right) \pm 2\varrho guhh_x = -2uh\Pi_x.$$

For the next step, first note that: $uhh_x = \left(uh^2\right)_x - h\,(uh)_x = \left(uh^2\right)_x - h\,(h)_t$ due to the mass conservation equation, moreover, $uhh_x = \left(uh^2\right)_x - \frac{1}{2}\left(h^2\right)_t$. Therefore,

$$\varrho\left(\left(u^2h\right)_t + \left(u^3h\right)_x\right) \pm \varrho g\left(2\left(uh^2\right)_x - \left(h^2\right)_t\right) = -2uh\Pi_x.$$

Rearranging and using $U = hu$ for the respective layers gives:

$$\varrho\left(\left(\frac{U^2}{h}\right)_t \pm g\left(h^2\right)_t + \left(\frac{U^3}{h^2}\right)_x \pm 2g\,(hU)_x\right) = -2uh\Pi_x. \tag{4.9}$$

By taking the average of Eq. (4.9) we obtain:

$$\left(\left\{\frac{\varrho}{h}\right\}U^2 + g\left[\varrho h^2\right]\right)_t + \left(\left[\frac{\varrho}{h^2}\right]U^3 + 2g\left\{\varrho h\right\}U\right)_x = 0. \tag{4.10}$$

The terms of Eq. (4.10) are individually handled and simplified, the purpose of which will become apparent in the following section where the Boussinesq approximation is applied. Hence, the first term writes as:

$$\left(\left\{\frac{\varrho}{h}\right\}U^2\right)_t = \left(\frac{U^2}{\langle h\rangle}\left(\frac{\{\varrho\}}{2}\{h\} + \frac{[\varrho]}{2}[h]\right)\right)_t,$$

whereas the second term reads as:

$$\left(\left[\frac{\varrho}{h^2}\right]U^3\right)_x = \left(\frac{U^3}{\langle h\rangle^2}\left(-\frac{\{\varrho\}}{2}\left[h^2\right] + \frac{[\varrho]}{2}\{h^2\}\right)\right)_x.$$

Lastly, the third term after few rearrangements simplifies to:

$$\left[\varrho h^2\right]_t + (2\{\varrho h\}U)_x = \frac{\{\varrho\}}{2}\left[h^2\right]_t + \frac{[\varrho]}{2}\{h^2\}_t + 2\left(\left(\frac{\{\varrho\}}{2}\{h\} + \frac{[\varrho]}{2}[h]\right)U\right)_x = \\ = \frac{[\varrho]}{4}[h]_t^2 + [\varrho]([h]\,U)_x\,.$$

Hence, the local energy conservation law Eq. (4.10) can be rewritten as:

$$\left(\frac{U^2}{\langle h\rangle}\left(\frac{\{\varrho\}}{2}\{h\} + \frac{[\varrho]}{2}[h]\right) + g\frac{[\varrho]}{4}[h]^2\right)_t + \\ + \left(\frac{U^3}{\langle h\rangle^2}\left(-\frac{\{\varrho\}}{2}\left[h^2\right] + \frac{[\varrho]}{2}\{h^2\}\right) + g\,[\varrho]\,([h]\,U)\right)_x = 0, \tag{4.11}$$

where the angular brackets $\langle\rangle$ denote multiplication of the enclosed quantities. Similarly to Eq. (4.8), it can be integrated across hydraulic jumps to obtain the jump conditions.

4.1.4 Nondimensionalisation

The equations are nondimensionalised using $\frac{L}{C}$ as the time scale where L is the horizontal length scale and C is the characteristic wave speed defined by $C^2 = 2gH\frac{[\varrho]}{\{\varrho\}}$ and used as the velocity scale. Heights are scaled with respect to the total height H and the flux U is respectively scaled with CH. Moreover, densities are scaled with $\bar{\varrho}$ and the layers' densities can be expressed as

$$\varrho_\pm = 1 \pm \delta \tag{4.12}$$

where δ is a measure of the density difference and favours the elegant description of the equations.

A shift in the vertical direction can be performed centring the interface height about $z = 0$ leads to:

$$h_\pm = \frac{1}{2}(1 \pm \eta)\,. \tag{4.13}$$

Therefore, the nondimensional mass conservation reads as:

$$\eta_t + \frac{1}{2}\left(v\left(1-\eta^2\right)\right)_x = 0, \tag{4.14}$$

where $\eta = [h]$ and $v = [u]$ are the differentials of depth and velocity between the layers. In turn, the nondimensionalised momentum equation:

$$\left(\eta v\,(1-\delta\eta)\right)_t + \frac{1}{4}\left(v^2 + \eta^2 - 3\eta^2v^2 + 2\delta\eta^3v^2\right)_x = 0. \tag{4.15}$$

Similarly, the shear velocity Eq. (4.5) in nondimensional form is given by:

$$\left(v\left(1-\delta\eta\right)\right)_t + \frac{1}{4}\left(v^2\delta\left(1+\eta^2\right) + 2\eta\left(1-v^2\right)\right)_x = 0. \tag{4.16}$$

Lastly, the dimensionless energy conservation law corresponding to Eq. (4.11) writes as:

$$\left(v^2\langle h\rangle\left(1+\delta\eta\right) + \frac{\eta^2}{4}\right)_t + \left(v^3\langle h\rangle\left(\delta\left\{h^2\right\} - \eta\right) + \eta v\langle h\rangle\right)_x = 0. \tag{4.17}$$

Equations (4.14)–(4.17) delineate the constitutive 1D two-layer system set of equations for arbitrary densities.

4.2 The Boussinesq lock-exchange problem

Under the Boussinesq approximation it is assumed that the densities differ only slightly from each other i.e.: $\delta \to 0$. This approximation permits the simplification of the equations as well as the analytic study of the problem at hand. As shown by (Milewski and Tabak, 2015), Eqs. (4.14) and (4.16) reduces to a remarkably symmetric form in the Boussinesq approximation. Whereas the mass conservation Eq. (4.14) remains virtually unchanged, the circulation conservation Eq. (4.16) reduces to:

$$v_t + \frac{1}{2}\left(\eta\left(1-v^2\right)\right)_x = 0. \tag{4.18}$$

Accordingly, the momentum conservation equation Eq. (4.15) reads

$$(\eta v)_t + \frac{1}{4}\left(v^2\left(1-3\eta^2\right) + \eta^2\right)_x = 0, \tag{4.19a}$$

where, equivalently, substitution $\eta v = w$ leads to:

$$(w)_t + \frac{1}{4}\left(\left(\frac{w}{\eta}\right)^2\left(1-3\eta^2\right) + \eta^2\right)_x = 0. \tag{4.19b}$$

Finally, the energy conservation Eq. (4.17) under the Boussinesq approximation takes the form:

$$\left(v^2\left(1-\eta^2\right) + \eta^2\right)_t + \left(\eta v\left(1-\eta^2\right)\left(1-v^2\right)\right)_x = 0. \tag{4.20}$$

4.2.1 Characteristic speeds and Riemann invariants

Solutions of a homogeneous system of the form:

$$\mathfrak{U}_t + F_x(\mathfrak{U}) = \mathfrak{U}_t + A\mathfrak{U}_x = 0, \tag{4.21}$$

corresponding to $\mathfrak{U} = [\eta, v]^{\mathrm{T}}$, where $A = \frac{\partial F}{\partial \mathfrak{U}}$ is the Jacobian of Eqs. (4.14) and (4.18) which reads as:

$$\begin{bmatrix} -\eta v & \frac{1}{2}\left(1-\eta^2\right) \\ \frac{1}{2}\left(1-v^2\right) & -\eta v \end{bmatrix},$$

are examined with the simple wave method. The simple-wave method enables the analysis of piecewise solutions to the initial value problem for the propagation of disturbances in the subsequent motion. Simple wave solutions are of the form:

$$\mathfrak{U}(x,t) = W(\mathfrak{r}(x,t)).$$

Substitution of the above expression in to Eq. (4.21) yields:

$$\left(I\mathfrak{r}_t + A\mathfrak{r}_x\right) W'(\mathfrak{r}) = 0,$$

where I is the 2×2 identity matrix and $W'(\mathfrak{r})$ is an eigenvector of A. Non-trivial solutions exist provided that

$$|A - \lambda I| = 0,$$

where λ is the corresponding set of eigenvalues of A. The eigenvalues define the slope

$$\frac{dx}{dt} = -\frac{\mathfrak{r}_t}{\mathfrak{r}_x} = \lambda^{\pm}$$

of the families of characteristic curves $C^{\pm}$ to which there exist two associated linearly independent eigenvectors $\mathbf{R} = (R^{+}, R^{-})^{\mathrm{T}}$ that are solutions of the equations:

$$(A - \lambda I) \cdot \mathbf{R} = 0.$$

Hence, premultiplication of the system Eq. (4.21) with $\mathbf{R}$ yields:

$$\frac{dW}{dt} \cdot \mathbf{R} = 0,$$

that cast in the canonical form reads as

$$\frac{\partial \mathfrak{r}^{\pm}}{\partial t} + \lambda^{\pm}\frac{\partial \mathfrak{r}^{\pm}}{\partial x} = 0, \tag{4.22}$$

integration of which yields the Riemann invariants $\mathfrak{r}(\eta, v)$ that remain constant along their corresponding simple wave solution.

For the two-layer system of equations Eqs. (4.14) and (4.18) as shown by (Long, 1956b; Cavanie, 1969; Ovsyannikov, 1979; Sandstrom and Quon, 1993; Baines, 1995; Milewski and Tabak, 2015; Esler and Pearce, 2011) this corresponds to the characteristic velocities:

$$\lambda^{\pm} = \frac{3}{4}\mathfrak{r}^{\pm} + \frac{1}{4}\mathfrak{r}^{\mp} = -\eta v \pm \frac{1}{2}\sqrt{1-\eta^2}\sqrt{1-v^2} \tag{4.23}$$

and the Riemann invariants

$$\mathfrak{r}^{\pm} = -\eta v \pm \sqrt{(1-\eta^2)(1-v^2)}, \tag{4.24}$$

where the substitutions $\mathfrak{r}^{\pm} = \pm \arccos(\mathfrak{r}^{\pm})$ has been used for the Riemann invariants which are the constants of integration of the characteristic form of Eqs. (4.14) and (4.18):

$$\frac{dv}{d\eta} = \mp\sqrt{\frac{1-v^2}{1-\eta^2}}. \tag{4.25}$$

It is worth highlighting that due to the hyperbolicity condition, it is required that the shear velocity cannot exceed $v^2 \leq 1$; which otherwise would result in a Kelvin-Helmoltz type of instability. Equivalently, it is required that the interface height is constrained between the top and bottom boundaries i.e. $\eta^2 \leq 1$.

4.2.2 Jump conditions

In the context of the shallow-water approximation, shocks are the discontinuities in the wave amplitude, to which the partial differential equations describing the wave propagation cease to apply. However, the relevant physics may still hold, for a hyperbolic system in conservative form, where the integral relationships known as the Rankine-Hugoniot conditions are still capable of encapturing the behaviour across discontinuities Whitham (1975, p. 26).

Considering a conservation law of the form Eq. (4.21), the function $\mathfrak{U}(x,t)$ satisfying the integral relationship

$$\frac{d}{dt}\int_{x_1}^{x_2} \mathfrak{U}(x,t)dx = F\left(\mathfrak{U}(x_1,t)\right) - F\left(\mathfrak{U}(x_2,t)\right), \tag{4.26}$$

is called a weak solution and $x_1 \leq x \leq x_2$ define an interval in which the discontinuity is contained. Suppose that $\mathfrak{U}$ and $F\left(\mathfrak{U}(x,t)\right)$ as well as their respective first derivatives are continuous in the ranges $x_1 \leq x < \xi(t)$ and $\xi(t) < x \leq x_2$ where $\xi(t)$ denotes the location of the discontinuity. According to the Leibniz integral law, Eq. (4.26) reads as:

$$\begin{aligned} F\left(\mathfrak{U}(x_1,t)\right) - F\left(\mathfrak{U}(x_2,t)\right) &= \frac{d}{dt}\left(\int_{x_1}^{\xi(t)} + \int_{\xi(t)}^{x_2}\right)\mathfrak{U}(x,t)dx \\ &= \int_{x_1}^{\xi(t)} \partial_t \mathfrak{U}(x,t)dx + \int_{\xi(t)}^{x_2} \partial_t \mathfrak{U}(x,t)dx + \dot{\xi}(t)\left(\mathfrak{U}_l - \mathfrak{U}_r\right) \end{aligned}$$

where $\dot{\xi}(t) = \frac{d\xi(t)}{dt}$, $\mathfrak{U}_l = \lim_{x\to\xi^-(t)} \mathfrak{U}(x,t)$ and accordingly for $\mathfrak{U}_r$. Since the derivatives of $\mathfrak{U}$ are bounded in each interval, the integrals tend to zero in the limits when

arbitrarily close to the shock. Subsequently, the expression above reads as

$$[\![F(\mathfrak{U})]\!] = \dot{\xi}(t)[\![\mathfrak{U}]\!], \tag{4.27}$$

where $[\![\,]\!]$ denotes the differential of the enclosed quantity across the discontinuity. Then, using Eqs. (4.14), (4.18) and (4.19a) we obtain the Rankine-Hugoniot conditions:

$$\begin{cases} \dot{\xi} = \dfrac{\frac{1}{2}[\![(1-\eta^2)\, v]\!]}{[\![\eta]\!]}, & \text{(4.28a)} \\ \dot{\xi} = \dfrac{\frac{1}{2}[\![(1-v^2)\, \eta]\!]}{[\![v]\!]}, & \text{(4.28b)} \\ \dot{\xi} = \dfrac{\frac{1}{4}[\![v^2\,(1-3\eta^2) + \eta^2]\!]}{[\![\eta v]\!]}, & \text{(4.28c)} \end{cases}$$

across the discontinuous state. These relationships are bridged by the jump propagation speed $\dot{\xi}$, reducing the number of unknowns to the resulting states of η and v after the jump. In the shallow water framework only one conservation law in addition to the mass conservation can be applied Whitham (1975, p. 458). As discussed by Priede (2018) the more appropriate conservation law is the momentum conservation equation which is known to govern continuous as well as discontinuous solutions. Therefore, using Eqs. (4.28a) and (4.28c) these lead to:

$$\dot{\xi} = \frac{\frac{1}{2}[\![(1-\eta^2)\, v]\!]}{[\![\eta]\!]} = \frac{\frac{1}{4}[\![v^2\,(1-3\eta^2) + \eta^2]\!]}{[\![\eta v]\!]} \tag{4.29}$$

An appeal to physical considerations for physically meaningful shocks can be made via examining the Lax entropy condition, Sharma (2010) and Debnath (2011). The Rankine-Hugoniot condition yielded by the energy conservation law Eq. (4.20), defines the energy balance across the discontinuity, and reads as:

$$-\dot{\xi}[\![v^2\,(1-\eta^2) + \eta^2]\!] + [\![\eta v\,(1-\eta^2)\,(1-v^2)]\!] \equiv \dot{\varepsilon}. \tag{4.30}$$

This imposes an additional constraint on the feasible hydraulic jumps where energy can not be generated and thus $\dot{\varepsilon} \leq 0$.

4.2.3 Lock-Exchange problem

The lock-exchange problem is a two-layer analogue of the dam-break problem in single-layer shallow water flows, which can be widely found in literature (Whitham, 1975; Stoker, 1957), has been extensively studied as it provides insight into the motion of shallow water flows and a useful benchmark for the validation of numerical schemes. The general case of two fluids of different (or slightly different)

densities in a closed container that are initially separated by a vertical separating plate(lock) is considered. The separating plate is instantaneously removed and thus initiates the flow. Then the slightly denser fluid penetrates into the lower-density fluid. Figure 4.1 illustrates the lock-exchange problem where the densities are considered to be $\varrho_+ \gtrapprox \varrho_-$.

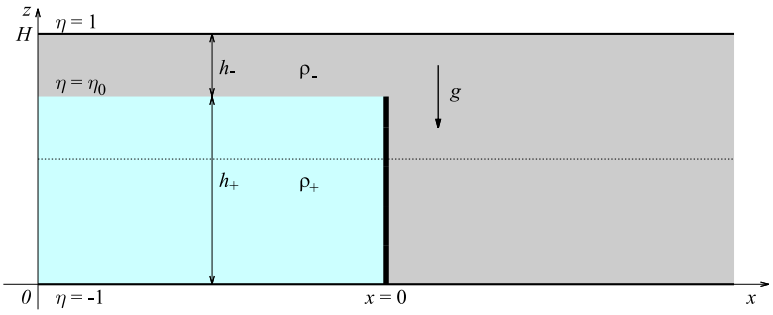

FIGURE 4.1: Partial lock-exchange.

The simple-wave method is applicable to disturbances propagating into an initially homogeneous state and enables the analytic solution of the lock-exchange problem. For the solution of this system we will consider sections of the domain separately with $x = 0$ separating the upstream($x < 0$) and downstream ($x > 0$) direction of the flow. The first step in understanding the behaviour of the lock-exchange problem is to find the slope of characteristics which signify the maximum propagation speed of information in their respective regions.

Upstream flow, x<0

The study of the lock-exchange problem is greatly simplified with the use of the following substitutions: $\eta = \sin(\theta)$ and $v = \sin(\phi)$ which will be interchangeably used with the original variables. These substitutions are permitted on the ground that the corresponding range of validity is the same with the associated physical variables.

Upstream ($x < 0$), the initial state is defined at $\eta^- = \eta_0$ and $v^- = 0$. Substituting $\eta = \sin(\theta)$ and $v = \sin(\phi)$ for the aforementioned states, corresponds to $\theta = \frac{\pi}{2} - \theta_0$ and $\phi = 0$, where $\theta_0 \in [0, \pi]$. The Riemann invariant associated with this state, can be written as:

$$r^+ = \phi + \theta = \frac{\pi}{2} - \theta_0. \tag{4.31a}$$

which yields $\phi = \frac{\pi}{2} - \theta_0 - \theta$. Then the Riemann invariant associated with the C^- characteristics extending upstream from the lock reads as:

$$r^- = \phi - \theta = \frac{\pi}{2} - (\theta_0 + 2\theta), \tag{4.31b}$$

Using Eq. (4.31), the upstream velocity can be written as $v^- = \sin\left(\frac{\pi}{2} - \theta - \theta_0\right) = \cos(\theta + \theta_0)$ where with the use of $\eta_0 = \sin\left(\frac{\pi}{2} - \theta_0\right) = \cos(\theta_0)$, v is expressed as:

$$v^- = \cos(\theta + \theta_0) = \eta_0\sqrt{1-\eta^2} - \eta\sqrt{1-\eta_0^2}. \tag{4.32}$$

Further, using Eq. (4.23) and Eq. (4.31) the characteristic speed can be written as:

$$\lambda^- = -\frac{3}{4}\cos(r^-) + \frac{1}{4}\cos(r^+) = -\frac{3}{4}\sin(\theta_0 + 2\theta) + \frac{1}{4}\sin(\theta_0), \tag{4.33}$$

which is constant along C^-, thus defining straight lines with slope $\lambda^- = \frac{x}{t}$. Similarly, for the C^+ characteristics, we have:

$$\lambda^+ = \frac{3}{4}\cos(r^-) - \frac{1}{4}\cos(r^+) = \frac{3}{4}\sin(\theta_0) - \frac{1}{4}\sin(\theta_0 + 2\theta). \tag{4.34}$$

This enables the investigation for the validity of these solutions. Hence, the family of C^+ characteristics in terms of the C^- yield the characteristic speed:

$$\lambda^+ = \frac{1}{3}\lambda^- + \frac{2}{3}\sin(\theta_0), \tag{4.35}$$

which is equivalent to:

$$\frac{dx}{dt} = \frac{1}{3}\frac{x}{t} + \frac{2}{3}\sin\theta_0,$$

and has the general solution $x(t) = ct^{1/3} + t\sin\theta_0$, where the unknown constant c is determined by matching with the solution for the undisturbed upstream state $x(t) = x_0 + \frac{1}{2}t\sin\theta_0$, which holds below the leftmost λ^- characteristic defined by

$$\frac{x}{t} \leq \min\lambda^- = \frac{1}{4}(\sin\theta_0 - 3).$$

It can be seen that both families of characteristics become parallel to each other when:

$$-\frac{3}{4}\sin(\theta_0 + 2\theta) + \frac{1}{4}\sin(\theta_0) = \frac{3}{4}\sin(\theta_0) - \frac{1}{4}\sin(\theta_0 + 2\theta),$$

at $\theta = -\theta_0$, where $\lambda^+ = \lambda^- = \sin(\theta_0)$ and the solution spreads down from the lock until $\frac{x}{t} = \sin(\theta_0)$. This defines the range of validity of the characteristics in $\theta \in \left[-\theta_0, \frac{\pi}{2} - \theta_0\right]$. Both families of characteristics are shown in figure 4.2a.

Downstream flow x>0

For the downstream region ($x > 0$), which is filled with the lighter fluid, the interfacial height is initially located at $\eta^+ = -1$ and the fluid is at rest $v^+ = 0$. Utilising $\eta = \sin(\theta)$ and $v = \sin(\phi)$, it can be deduced that $\theta = -\frac{\pi}{2}$ and $\phi = 0$. Then the Riemann invariant along the C^- characteristics which originate from

this state is

$$r^- = \phi - \theta = \frac{\pi}{2}, \tag{4.36a}$$

while the Riemann invariant propagating along C^+ is

$$r^+ = \phi + \theta = \frac{\pi}{2} + 2\theta, \tag{4.36b}$$

both of which are invariant along the respective characteristics. Using Eq. (4.36), velocity can be written as $v^+ = \sin\left(\frac{\pi}{2} - \theta\right) = \cos(\theta)$ or in terms of η as:

$$v = \sqrt{1 - \eta^2}. \tag{4.37}$$

Further, by Eq. (4.23) and using Eq. (4.36) the negative characteristic speed λ^- writes as:

$$\lambda^- = -\frac{3}{4}\cos(r^-) + \frac{1}{4}\cos(r^+) = -\frac{3}{4}\cos\left(\frac{\pi}{2} + 2\theta\right) = -\frac{3}{4}\sin(2\theta)\,. \tag{4.38}$$

Respectively, using Eq. (4.23) and relation Eq. (4.36b) one obtains:

$$\lambda^+ = \frac{3}{4}\cos(r^-) - \frac{1}{4}\cos(r^+) = -\frac{1}{4}\cos\left(\frac{\pi}{2} - 2\theta\right) = -\frac{1}{4}\sin(2\theta)\,. \tag{4.39}$$

The slope of the C^- characteristics in terms of C^+ is expressed as:

$$\lambda^- = \frac{1}{3}\lambda^+, \tag{4.40}$$

which defines the slope of the C^- characteristics as they cross the C^+ characteristics. This relation, when written in terms of x and t takes the form of an ODE $\frac{dx}{dt} = \frac{1}{3}\frac{x}{t}$ and defines the λ^- characteristics above the rightmost λ^+ characteristic, i.e. for $x \geq \frac{3}{4}t$. In this region, we have $x(t) = Ct^{1/3}$, where the unknown constant C is determined by matching with $x(t) = \text{const}$ for $0 \leq x \leq \frac{3}{4}t$ which corresponds to $\lambda_\pm = 0$ for the undisturbed downstream state. It is important to note that the solutions defined in the preceding section by Eq. (4.32)–Eq. (4.34) for the upstream flow overlap with the downstream solutions in the region $0 \leq \frac{x}{t} \leq \sin(\theta_0)$. Both families of characteristics are shown in figure 4.2a.

Downstream from the lock ($x > 0$), the characteristics obtain equal slope for $\lambda^+ = \lambda^-$ at $\theta = 0$ with $\theta_0 \in [0, \pi]$. This defines the range of validity of the characteristics in $\theta \in \left[-\frac{\pi}{2}, 0\right]$, where both families of characteristics intersect. Note that for $\theta_0 > 0$, solution Eq. (4.33) extends downstream from the lock up to $\frac{x}{t} = \sin\theta_0$, which corresponds to $\theta = -\theta_0$. Thus, this solution overlaps with Eq. (4.38) in the sector $0 \leq \frac{x}{t} \leq \sin\theta_0$ where both solutions are expected to be connected by a jump.

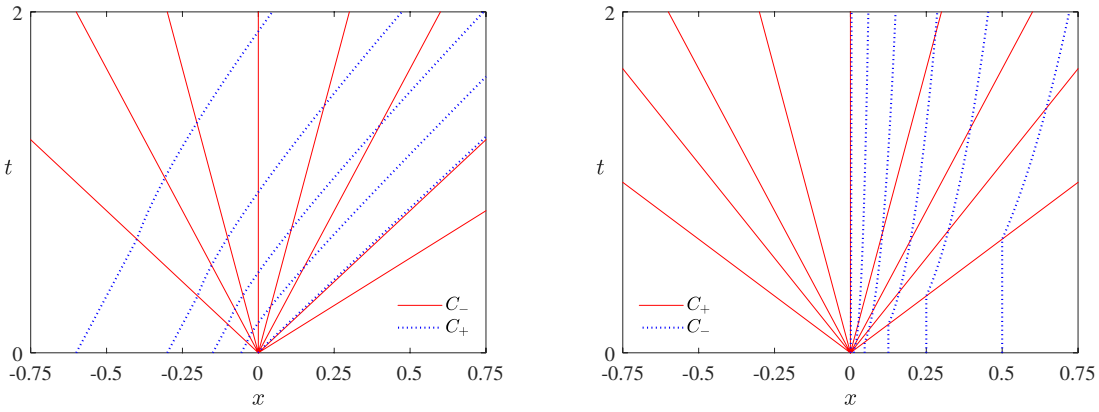

(a) Upstream ($x < 0$) region (b) Downstream ($x > 0$) region

FIGURE 4.2: Family of characteristics C^- and C^+ for the partial lock-exchange problem in the upstream and downstream regions and different initial interface heights η_0.

4.2.4 Jumps forming in the multivalued parts of the analytical solution

First, consider the jump in the upstream direction ($x < 0$), for which the state is defined as:

$$v^+ = 0 \quad \& \quad \eta^+ = \eta_0$$
$$v^- = v \quad \& \quad \eta^- = \eta$$

where the subscripts "+" and "−" indicate the state of the flow right and left of the jump respectively; and η_0 is the initial interfacial height. Then, Eq. (4.29) yields:

$$v^2 = \frac{\left(\eta^2 - \eta_0^2\right)(\eta - \eta_0)}{\eta^3 + \eta + \eta_0\left(1 - 3\eta^2\right)}. \tag{4.41}$$

which relates the shear velocity v with the initial interfacial height η_0 and the jump height η. As seen in §4.2.3, applicability of the upstream solution is restricted to $\theta \in \left[-\theta_0, \frac{\pi}{2} - \theta_0\right]$, above which it needs to be connected with the back jump velocity of propagation. As such, connecting Eq. (4.32) with Eq. (4.41) one obtains the following relation:

$$\frac{\left(\eta^2 - \eta_0^2\right)(\eta - \eta_0)}{\eta^3 + \eta + \eta_0\left(1 - 3\eta^2\right)} = \left(\eta_0\sqrt{1-\eta^2} - \eta\sqrt{1-\eta_0^2}\right)^2. \tag{4.42}$$

This equation has two possible roots, $\eta = 0$ and $\eta = \eta_0$. At this stage it will be assumed that $\eta = \eta_0 > 0$, corresponding to $\theta_0 \leq \frac{\pi}{2}$. Using the first root, it is possible to describe the jump from the mid-height ($\eta = 0$) up to the initial interfacial height ($\eta = \eta_0$). Further, at $\eta = 0$ by Eq. (4.41) the shear velocity is $v = \eta_0$. Using this information into the jump propagation speed Eq. (4.28a) yield the maximum propagation speed of the jump $\dot{\xi} = -\frac{1}{2}$ independently of the initial

height η_0. More interestingly, for $\eta = \eta_0 \leq 0$, corresponding to $\theta_0 > \frac{\pi}{2}$, the jump in the upstream direction vanishes because the solution of Eq. (4.33) ceases to be double valued which is confirmed by figure 4.3d.

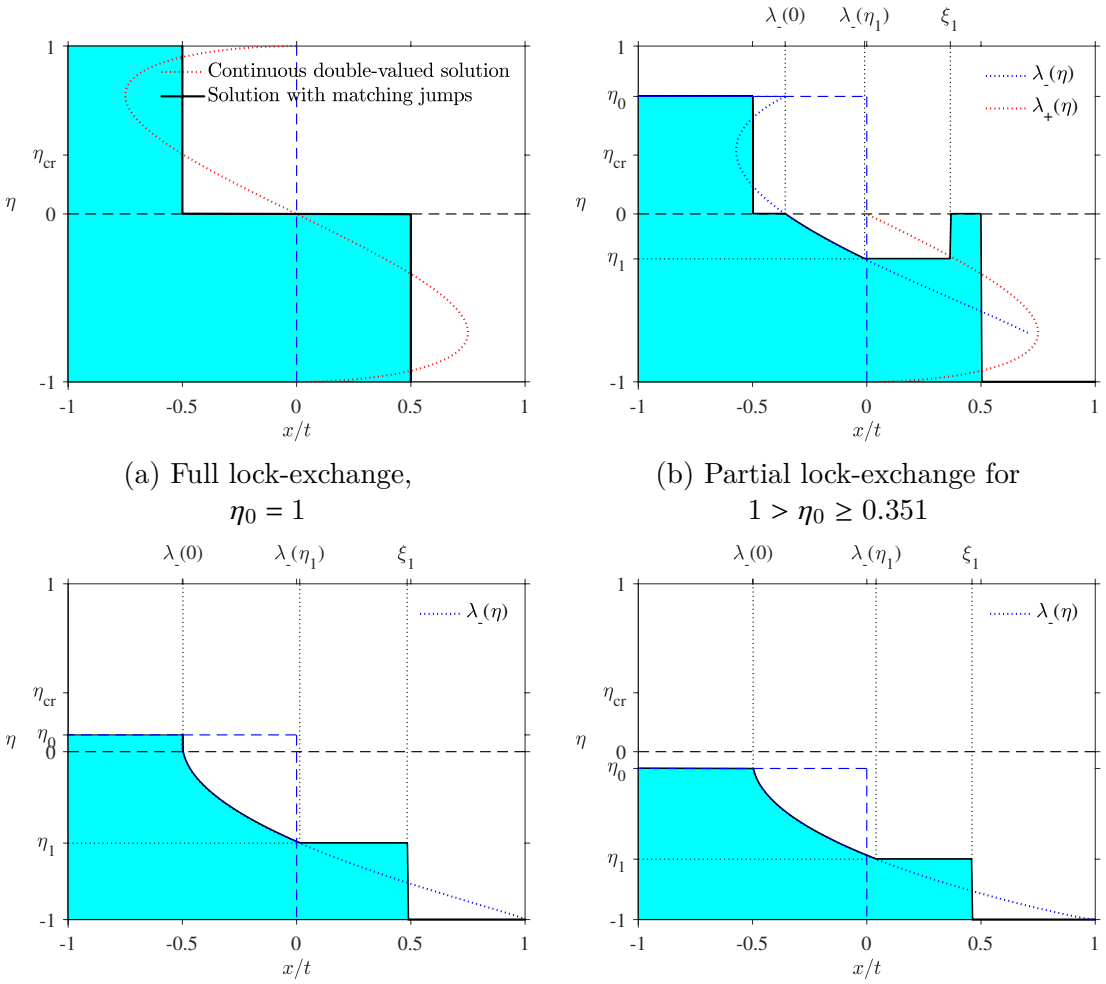

(a) Full lock-exchange, $\eta_0 = 1$

(b) Partial lock-exchange for $1 > \eta_0 \geq 0.351$

(c) Partial lock-exchange for $0.351 > \eta_0 \geq 0$

(d) Partial lock-exchange for $\eta_0 < 0$

FIGURE 4.3: Interface height versus the similarity variable x/t for the lock-exchange problem.

In the downstream region ($x > 0$), the states of the height and velocity on either side of the discontinuity are described as follows:

$$v^+ = 0 \qquad \eta^+ = -1,$$
$$v^- = v \qquad \eta^- = \eta,$$

where η^+ and v^+ are the known variables due to the jump propagating into a homogeneous state. Hence, from Eq. (4.29), we obtain a relation which describes the shear velocity depending on the interface height:

$$v^2 = \frac{1 - \eta^2}{-\eta^2 - 2\eta + 1}. \tag{4.43}$$

In this case the shear velocity defined by Eq. (4.43), has to match at the jump with shear velocity Eq. (4.37) defined by the Riemann invariant:

$$\frac{1-\eta^2}{-\eta^2-2\eta+1} = 1-\eta^2.$$

The possible interface heights at the jump are defined by $\eta\,(2+\eta)\left(1-\eta^2\right) = 0$. Out of the four possible solutions, only two are physically relevant and satisfy the energy dissipation condition Eq. (4.30). These are $\eta = 0$ and $\eta = -1$. The latter is just the original double-valued solution. The solution $\eta = 0$ admits a downstream shear velocity of $v = 1$ and corresponds to a jump propagation velocity of $\dot{\xi} = \frac{1}{2}(1-\eta)\vartheta = \pm\frac{1}{2}$, where only the positive solution , which describes a jump propagating downstream, satisfies the energy dissipation constraint Eq. (4.30).

This gives rise to a secondary -trailing- jump with downstream interface height $\eta = 0$. The front and back states of this jump are:

$$\begin{aligned} v^+ &= 1 \qquad & \eta^+ &= 0, \\ v^- &= v_1 \qquad & \eta^- &= \eta_1. \end{aligned}$$

Then, Eq. (4.29) yields the shear velocity behind the jump:

$$v_1 = \frac{1-\eta_1^2}{1+\eta_1^2}. \tag{4.44}$$

Matching with the upstream shear velocity defined by Eq. (4.32) enables us to link the final height preceding the trailing jump with the initial interfacial height as follows:

$$\frac{1-\eta_1^2}{1+\eta_1^2} = \eta_0\sqrt{1-\eta_1^2} - \eta_1\sqrt{1-\eta_0^2}$$

which is equivalent to:

$$\vartheta_1 = \cos(\theta_1+\theta_0) = \frac{1-\sin^2\theta_1}{1+\sin^2\theta_1}, \tag{4.45}$$

which relates θ_1 behind the jump with $\theta_0 = \arccos\eta_0$ defined by the state upstream of the lock. Analytical solutions for the interface height behind the jump, $\eta_1 = \sin\theta_1$, and its velocity of propagation

$$\dot{\xi}_1 = \frac{\eta_1\left(\eta_1^2-3\right)}{2\left(\eta_1^2+1\right)}, \tag{4.46}$$

are plotted in figure 4.4b along the characteristic velocity $\lambda^-(\eta_1)$ against η_0.

Upon decreasing η_0 the trailing jump velocity of propagation $\dot{\xi}_1$ attains the velocity of the leading edge which as seen in figure 4.4a can never propagate faster than $\dot{\xi} = \frac{1}{2}$. Solving Eq. (4.46) with $\dot{\xi}_1 = \frac{1}{2}$ the only physically meaningful

solution is $\eta_1 = 1 - \sqrt{2}$. At this critical height, both edges merge, destroying the head-block. Using Eq. (4.45) it is found that this critical upstream interface height is $\eta_c = 0.351$, as illustrated in figure 4.3c.

Consequently, for $\eta_0 \leq \eta_c$, the solution Eq. (4.33) has to connect directly to the downstream state $\eta^+ = -1$ and $v^+ = 0$ which is at rest. Combining the downstream shear velocity obtained in Eq. (4.43) with the upstream state $v^- = \cos(\theta + \theta_0)$ and $\eta_0 = \sin(\theta)$ yields:

$$v_1 = \cos(\theta_1 + \theta_0) = \frac{\cos\theta_1}{\sqrt{\cos^2\theta_1 - 2\sin\theta_1}}, \tag{4.47}$$

which is analogous to Eq. (4.44). The parameters of the downstream jump resulting from the solution of Eq. (4.47) are plotted in figure 4.4a. Figure 4.3c and figure 4.3d, illustrating the interface height versus the similarity variable x/t, correspond to two interface configurations in the case where $\eta_0 \leq \eta_c$. The first configuration for an initial interface height $0 \leq \eta_0 \leq \eta_c$ is illustrated in figure 4.3c, where an upstream jump from η_0 is connected to the mid-height $\eta = 0$ analogously to the head-block in the downstream state. Figure 4.3d delineates the second configuration $\eta_0 \leq 0$ where there is no more an upstream jump and the solution connects directly to the upstream initial interface height at $\eta = \eta_0$ as specified by the second root of Eq. (4.42). In this case, similarly to the single-layer dam-break problem, the upstream state can connect directly with $\eta = -1$ at $\theta = -\frac{\pi}{2}$ without a leading jump. However, as seen in figure 4.4a, an infinitesimal perturbation would result in a non-zero front height, which in turn would halt the propagation of the heavier fluid along the bottom, thus, leading to an increasing perturbation where the upstream state propagates faster than the front. Therefore, this alternative solution is inherently unstable with respect to the height perturbation of the leading edge.

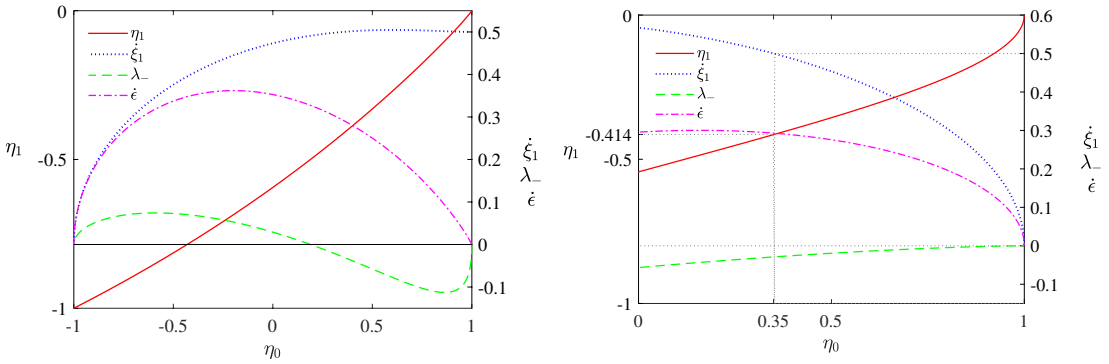

(a) Leading jump. (b) Trailing head-block jump.

FIGURE 4.4: Jump propagation speed $\dot{\xi}$ along with the associated energy $\dot{\epsilon}$, the characteristics $\dot{\lambda}$ and the the interface height η_1, for all possible initial interfacial heights η_0.

4.2.5 Numerical solution of conservative SW equations

In the present section the analytical solutions previously obtained for the Boussinesq lock-exchange problem are verified by solving the lock-exchange problem numerically using the 1D Lax-Wendroff method. For comparison, in addition to the momentum and mass conservation equations defined by Eqs. (4.14) and (4.19b), the alternative system in which Eq. (4.19b) is replaced by the circulation conservation law Eq. (4.18) is also solved.

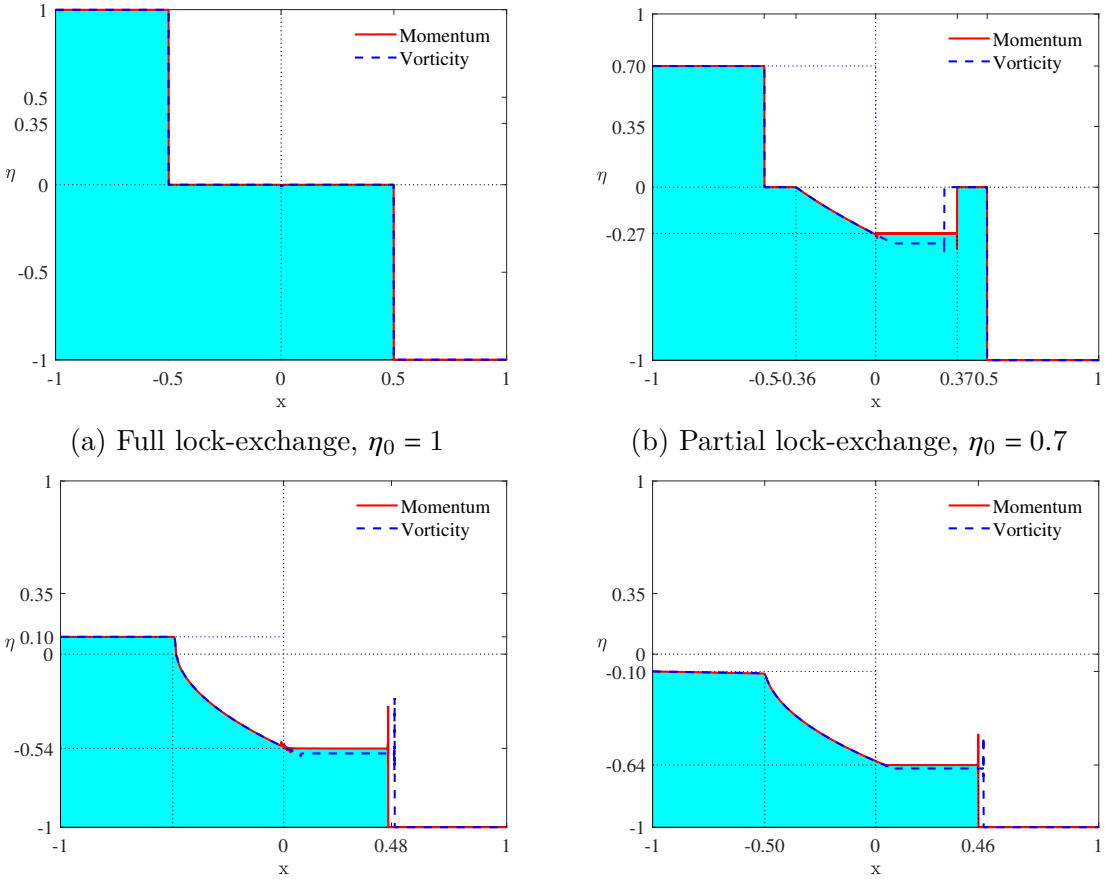

(a) Full lock-exchange, $\eta_0 = 1$

(b) Partial lock-exchange, $\eta_0 = 0.7$

(c) Partial lock-exchange, $\eta_0 = 0.1$

(d) Partial lock-exchange, $\eta_0 = -0.1$

FIGURE 4.5: Interface height at the time instant $t = 1$ after opening the lock with upstream heights $\eta_0 = 1$ (a), 0.7 (b), 0.1(c) and -0.1(d) obtained using momentum and circulation conservation laws with the Lax-Wendroff method. The time step is $dt = 10^{-3}$ and the spatial step is $dx = 5 \times 10^{-4}$ (a,b) and $dx = 10^{-2}$ (c,d).

In contrast to the circulation equation Eq. (4.5), numerical integration of the momentum equation Eq. (4.19b) suffers from large numerical errors when η is close to zero. In an attempt to eliminate this numerical uncertainty in the flux term of the momentum equation L'Hopital's rule was used. However this did not resolve this numerical uncertainty. Bringing in mind the product $w = \eta v$, which connects the momentum equation with the circulation equation, a hybrid

approach was employed. Whenever η happens to be close to zero, the momentum conservation equation is replaced with the vorticity one. This approach was found to produce numerical results in good agreement with the analytical solution for a range of lock heights, as illustrated in figure 4.5.

The exact solution for the full lock-exchange, illustrated in figure 4.5a, is reproduced using equal time and space steps. This is an optimal choice which renders the scheme marginally stable and ensures that the front advances one full grid step in one time step. In general, such marginally stable schemes are known to reduce spurious oscillations at the jumps Lerat and Peyret (1974). The scheme becomes unstable at larger time steps, which violate the CFL condition, whereas spurious oscillations arise at smaller time steps. In both cases, the solution for the full lock-exchange breaks down.

Using the same time step and grid size as for the full lock-exchange, the exact solution for a range of partial lock-exchange flows was able to be reproduced. The numerical solutions for the lock height $\eta_0 = 0.7$ is shown in figure figure 4.5b. In this case, spurious oscillations appear behind the head block because the respective jump advances less than a grid step per time step. As the head block becomes progressively thinner with lowering η_0, there is a range of lock heights $0.1 \lesssim \eta_0 \lesssim 0.7$ for which it was not possible to find a numerically stable solution. The stable numerical solution that re-emerges at $\eta_0 \approx 0.1$ has no elevated head block but just the downstream and upstream jumps and can be seen in figure 4.5c. This upstream jump vanishes when the lock is lower than the channel mid-height ($\eta_0 \leq 0$), as seen in figure 4.5d. In this case, the numerical solution produces a finite front height as predicted by the analytical solution. A smooth analytical solution akin to the single-layer dam-break solution is in principle possible. However, as argued above, such a smooth solution is unstable and thus unobservable in the two-layer system.

It is worth noting that the qualitative behaviour of the numerical solution of our system is similar, with respect to the appearance of the headblock, to the one studied by Esler and Pearce (2011), where the next order weakly non-hydrostatic approximation is investigated.

For reasons that are still not fully understood, there exists a range of initial height values (η_0) for which numerical solutions require extremely careful selection of the spatial and temporal discretisation. A number of *Total-Variation-Diminishing*, *Flux-Limiting* and higher order schemes were employed in an attempt to overcome this issue. For the most part the investigation proved unsuccessful as the considered algorithms partly or completely suppressed the front

headblock and modified the speed of the jump. On the contrary, the LWLF4 composite scheme in which three steps of Lax-Wendroff scheme are followed by a step of Lax-Friedrichs scheme, Liska and Wendroff (1998) provides a good approximation to the exact analytical solution. This composition significantly reduces spurious oscillations around the jumps, which are typical to the Lax-Wendroff scheme, without introducing excessive numerical diffusion which is typical to the Lax-Friedrichs scheme.

Chapter 5

Derivation of fully-nonlinear SW electric potential equation

In this chapter a fully nonlinear electric potential equation, based on the long-wave approximation, is derived. This differs form these presented in Bojarevics (1998) and Zikanov et al. (2000) and is applicable in modelling of large amplitude shallow-water waves.

5.1 Derivation

The perturbation of the cryolite-aluminium interface results in a spatial variation in the interfacial potential and the magnitude of the current flow across the interface. Consequently, this gives rise to a loop of perturbation current in the cell, which nevertheless, will not penetrate the cathode-block. The current loops will close in the aluminium, where the conductivity is much higher, and be uniformly distributed across the layer. Assumptions regarding the difference of conductivities between the layers enable the derivation of boundary conditions at the interface of each layer.

The side walls of the cell as well as the upper cryolite surface around the anode are considered to be electrical insulators. However, the anode block, where the current enters the electrolyte, is assumed to be perfectly conducting relative to the electrolyte, which means that it is effectively equipotential. Since the electric potential is defined up to an additive constant, the boundary condition is given by:

$$\varphi^{-}|_{z=H} = 0. \tag{5.1}$$

The boundary conditions of the electric potential at the interface fall from the continuity of the normal component of the current as follows:

$$\begin{cases} \mathbf{j}_n^+|_{z=h_+} = -\sigma_+ \, \partial_n \varphi^+|_{z=h_+} = j_n^+, & \text{(5.2a)} \\ \qquad\qquad\qquad\qquad \text{where} \quad \sigma_+ \, \partial_n \varphi^+|_{z=h_+} \equiv \sigma_- \, \partial_n \varphi^-|_{z=h_+} \\ \mathbf{j}_n^-|_{z=h_+} = -\sigma_- \, \partial_n \varphi^-|_{z=h_+} = j_n^-, & \text{(5.2b)} \end{cases}$$

In contrast, the cathode-block is effectively insulating with respect to the current perturbations, which means that the current density at the bottom is fixed

$$\sigma_+ \, \partial_z \varphi^+|_{z=0} = j_0 = \text{constant}, \tag{5.3}$$

In the above the subscript $\mathbf{n}$ denotes the unit normal to the interface:

$$\mathbf{n} = \frac{\mathbf{e}_z - \nabla h}{(1 + |\nabla h|^2)^{\frac{1}{2}}} \approx \mathbf{e}_z - \nabla h + O(\epsilon^2) \quad \text{and} \quad n_z = \mathbf{e}_z \ , \ h = 1 + O(\epsilon^2), \tag{5.4}$$

Since $z/L \sim H/L = \epsilon \ll 1$, the potential distribution in the bottom layer can be approximated by a power series expansion about a small quantity of vertical surface height z (Bojarevics and Romerio, 1994) as follows:

$$\varphi^+(\mathbf{r}) = \phi^+(\mathbf{x}) + z \, \partial_z \phi^+(\mathbf{x}) + \frac{z^2}{2} \, \partial_z^2 \phi^+(\mathbf{x}) + O(\epsilon^3), \tag{5.5}$$

where $\partial_z^k \phi^+ = \partial_z^k \varphi^+|_{z=0}$ and the vector $\mathbf{x}$ defines $\mathbf{x} = \mathbf{r} - z\mathbf{e}_z = x\mathbf{e}_x + y\mathbf{e}_y$. Therefore, with the expansion applied to the boundary condition at the interface, the normal current Eq. (5.2a) writes as:

$$\partial_n \varphi^+|_{z=h_+} = \mathbf{n} \ \nabla \varphi^+|_{z=0} = (\mathbf{e}_z - \nabla h) \, \nabla \varphi^+|_{z=h_+} = \partial_z \phi^+ + h_+ \, \partial_z^2 \phi^+ - \nabla h_+ \ \nabla \phi^+ + O(\epsilon^2)$$

Hence,

$$\partial_z \phi^+ + h_+ \, \partial_z^2 \phi^+ - \nabla h_+ \ \nabla \phi^+ = -\sigma_+^{-1} \ j_n^+,$$

where by using Eq. (5.3) after a few rearrangements it writes as:

$$h_+ \, \partial_z^2 \phi^+ - \nabla h_+ \ \nabla \phi^+ = -\sigma_+^{-1} \left(j_n^+ + j_0 \right).$$

In consideration of the conservation of charge Eq. (2.22) and Ohm's law the Laplacian of the electric potential leads to

$$\nabla^2 \phi = -\partial_z^2 \phi, \tag{5.6}$$

where ∇^2 horizontal component of the Laplacian. Consequently, this lead to the governing equation for the two-dimensional potential perturbation in the bottom

layer being read as:

$$-h_+ \nabla^2\phi^+ - \nabla h_+ \nabla\phi^+ = -\sigma_+^{-1}\left(j_n^+ + j_0\right) \Rightarrow$$
$$\nabla\left(h_+ \nabla\phi^+\right) = \sigma_+^{-1}\left(j_n^+ + j_0\right). \tag{5.7}$$

In turn, to determine the normal current j_n^+ of Eq. (5.7), the potential distribution in the top layer has been considered. This is sought similarly to that in the bottom layer. The expansion for the potential in upper layer writes as:

$$\varphi^-(\mathbf{r}) = \phi^-(\mathbf{x}) + (z-H)\,\partial_z\phi^-(\mathbf{x}) + \frac{(z-H)^2}{2}\partial_z^2\phi^-(\mathbf{x}) + O(\epsilon^3), \tag{5.8}$$

where $\partial_z^k\phi^- = \partial_z^k\varphi^-|_{z=H}$. By virtue of Eq. (5.6) and the boundary condition Eq. (5.1) the first and last term of Eq. (5.8) are eliminated due to:

$$\phi_-^{(0)} = \phi_-^{(2)} = 0. \tag{5.9}$$

Owing to the large difference in conductivities between the top and bottom layer, an equipotential surface is formed and the potential of the upper layer Eq. (5.2b) is expressed as:

$$\varphi^-|_{z=h_+} = (h_+ - H)\;\partial_z\phi^- + O(\epsilon^3) = -h_-\,\partial_z\phi^- + O(\epsilon^3) \equiv \varphi_0,$$

where $h_- = H - h_+$ is the top layer depth. Therefore,

$$j_n|_{z=h_+} = \frac{j_z}{n_z} \equiv j_z + O(\epsilon^2) \approx -\sigma_-\partial_z\varphi|_{z=H} = \sigma_-\frac{\varphi_0}{h_-}. \tag{5.10}$$

Finally, substituting Eq. (5.10) into Eq. (5.7), we obtain up to $O(\varepsilon^2)$ terms:

$$\sigma_+\nabla\cdot(h_+\nabla\phi_+) = j_0 + \sigma_-\frac{\varphi_0}{h_-}. \tag{5.11}$$

The unknown potential of the bottom layer, φ_0, is determined by the solvability condition of this equation, which is due to the Neumann boundary condition at the insulating side walls, where we have:

$$\partial_n\varphi_+ = \partial_n\phi_+^{(0)} + O(\varepsilon^2) = 0. \tag{5.12}$$

Integrating Eq. (5.11) over the horizontal cross-sectional area S and using this boundary condition, we obtain:

$$\int_S (j_0 + \sigma_-\varphi_0 h_-^{-1})\,\mathrm{d}^2\mathbf{x} = 0,$$

which is the solvability condition of Eq. (5.11). This condition, which requires the constancy of the total current $j_0 S = I_0$, defines the potential of the bottom layer as:

$$\varphi_0 = -\sigma_-^{-1} I_0 / \int_S h_-^{-1}\mathrm{d}^2\mathbf{x}.$$

Substituting this expression into Eq. (5.11), we obtain:

$$\sigma_+ \nabla \cdot (h_+ \nabla \phi_+^{(0)}) = j_0 \left(1 - S h_-^{-1} / \int_S h_-^{-1} \mathrm{d}^2\mathbf{x}\right), \tag{5.13}$$

which is the final form of electric potential equation. Note that this equation is fully non-linear and thus it is valid not only for small-amplitude perturbations but also for arbitrary large long-wave interface perturbations.

The distribution of the electric potential in the bottom layer Eq. (5.5) indicates that the respective electromagnetic force

$$\mathbf{j}_+ \times \mathbf{B_0} = \sigma_+ \mathbf{B_0} \times \nabla \phi_+^{(0)}(\mathbf{x}) + O(\varepsilon^2)$$

is depth-invariant up to $O(\varepsilon^2)$. Thus, the curl of this force has zero horizontal components which means that it preserves zero horizontal vorticity of the flow. Therefore, the electromagnetic force is compatible with the conservation of the depth-invariance similarly to the depth-invariance of the horizontal velocity, $\partial_z \mathbf{u} \equiv 0$, in the shallow-water approximation. Additionally, as shown in Eqs. (5.8,5.9), the horizontal component of the current perturbation in the top layer is $O(\varepsilon)$. Thus, the associated electromagnetic force is negligible in the leading-order approximation and the conservation of the depth-invariance holds also for the top layer.

Chapter 6

Linear stability analysis

In this chapter the linear stability of the shallow-water magnetohydrodynamic system is investigated. It is assumed that the perturbation has a characteristic longitudinal length scale L which is much larger than the layer depth H and focus on the interfacial waves of small amplitude:

$$\eta(\mathbf{x},t) = h(\mathbf{x},t) - \bar{h}_+ \ll H. \tag{6.1}$$

This means that the non-linear terms in the governing equations are higher-order small relative to the linear terms. After the linearisation, Eqs. (2.39a) and (2.39b) take the form:

$$\begin{cases} \partial_t \eta = \mp \bar{h}_\pm \nabla \cdot \mathbf{u}_\pm, & \text{(6.2a)} \\ \varrho_\pm \Big((\mathbf{u}_\pm)_t + g \nabla \eta \Big) = -\nabla \Pi + \mathbf{j} \times \mathbf{B}. & \text{(6.2b)} \end{cases}$$

The difference of the momentum equations for the respective layers reads as:

$$[\varrho \mathbf{u}]_t + g\,[\varrho]\,\nabla\eta = [\mathbf{j}] \times \mathbf{B}. \tag{6.3}$$

Taking the divergence while bearing in mind that $\nabla \cdot (\mathbf{j} \times \mathbf{B}) = 0$ yields:

$$[\varrho \nabla \cdot \mathbf{u}]_t + g\,[\varrho]\,\nabla^2\eta = 0,$$

where applying Eq. (6.2a) rewrites as:

$$-\partial_t^2 \eta \left\{ \frac{\varrho}{\bar{h}} \right\} + g\,[\varrho]\,\nabla^2\eta = 0.$$

Therefore, a pure interfacial gravity wave equation is obtained in the form:

$$\partial_t^2 \eta = c^2 \nabla^2 \eta.$$

where $c^2 = g\,[\varrho]\left\{\frac{\varrho}{\bar{h}}\right\}^{-1}$ is the wave propagation speed. Likewise, linearisation of Eq. (2.45), where friction is considered, results in:

$$\partial_t^2\eta + \gamma\partial_t\eta - c^2\nabla^2\eta = 0$$

where $\gamma = \left\{\frac{\varrho\gamma}{\bar{h}}\right\}\left\{\frac{\varrho}{\bar{h}}\right\}^{-1}$.

The impermeability condition requires that the normal component of velocity on Γ is $\mathbf{u}_n = 0$, which for Eq. (6.3) translates into the following condition for the interfacial height η:

$$\mathbf{n}\cdot(g\,[\varrho]\,\nabla\eta = \mathbf{j}\times\mathbf{B}) \quad \text{on} \quad \Gamma,$$

which rewrites as

$$\partial_n\eta = \beta\partial_\tau\phi,$$

where ∂_τ is the derivative in the direction tangential to the boundary and β is the Sele parameter defined in Eq. (2.42).

After linearisation, that is applying

$$\begin{aligned} h_+ &= \bar{h}_+ + \eta \approx \bar{h}_+, \\ h_-^{-1} &= (\bar{h} - \eta)^{-1} \approx \bar{h}_-^{-1} + \eta\bar{h}_-^{-2}, \end{aligned}$$

and taking into account that $\int_s \eta\,\mathrm{d}^2\vec{x} = 0$ due to the mass conservation, the potential equation (5.13), reduces to

$$\nabla^2\phi_+^{(0)} = -\frac{j_0\eta}{\sigma_+\bar{h}_+\bar{h}_-}, \tag{6.4}$$

which satisfies the solvability condition automatically owing to the mass conservation. Changing to dimensionless variables by using $L = \sqrt{L_xL_y} = S^{1/2}$, $\tau_0 = L/c$ and $\phi_0 = I_0/(\sigma_+\bar{h}_+)$ as the length, time and electric potential scales, respectively, yields the following nondimensional set of equations. The equation (5.13) of the electric potential reads as:

$$\nabla^2\phi = -\eta,$$

with the insulating boundary walls of the cell requiring that:

$$\partial_n\phi = 0 \quad \text{on} \quad \Gamma,$$

where ϕ is the dimensionless counterpart of $\phi_+^{(0)}$. Accordingly, the dimensionless governing equations for a uniform and purely vertical magnetic field are:

$$\begin{cases} \partial_t^2\eta = \nabla^2\eta - \gamma\partial_t\eta, & \partial_n\eta = \beta\partial_\tau\phi|_\Gamma, \qquad (6.5a) \\ \nabla^2\phi = -\eta, & \partial_n\phi|_\Gamma = 0. \qquad (6.5b) \end{cases}$$

The linear system of Eq. (6.5) can be treated as an eigenvalue problem. Solutions to the eigenvalue problem are sought in the form of travelling waves. Owing to the stationarity of the base state, small-amplitude disturbances of the interface height η and the associated electric potential ϕ can be sought as the normal modes:

$$\{\eta, \phi\}(\mathbf{x}, t) = \left\{\hat{\eta}, \hat{\phi}\right\}(y) e^{i(kx-\omega t)}, \tag{6.6}$$

with a real wave number k, a generally complex frequency ω, and the y-dependent amplitude distributions $\hat{\eta}(y)$ and $\hat{\phi}(y)$. Applying the equation Eq. (6.6) onto Eq. (6.5) while omitting the friction term $\gamma = 0$ results into a system of ODEs:

$$\begin{cases} -\omega^2\hat{\eta} = \hat{\eta}'' - k^2\hat{\eta}, & \hat{\eta}' = ik\beta\hat{\phi} \ \text{ on } \ \Gamma, \qquad (6.7a) \\ -\hat{\eta} = \hat{\phi}'' - k^2\hat{\phi}, & \hat{\phi}' = 0 \ \text{ on } \ \Gamma. \qquad (6.7b) \end{cases}$$

6.1 Semi-infinite domain

Following Lukyanov et al. (2001) the simplest geometry considered is that of a single wall, i.e. $[0 \le y < \infty] \times [-\infty < x < \infty]$. The general solution of Eq. (6.7) can be written as:

$$\begin{cases} \hat{\eta}(y) = \hat{\eta}_- e^{-i\kappa y} + \hat{\eta}_+ e^{i\kappa y}, \qquad (6.8a) \\ \hat{\phi}(y) = \hat{\phi}_0 e^{-ky} + \omega^{-2}\hat{\eta}(y), \qquad (6.8b) \end{cases}$$

where the corresponding boundary conditions write as:

$$\begin{cases} \hat{\phi}'(0) = 0 \ \text{ on } \ \Gamma, \qquad (6.9a) \\ \hat{\eta}'(0) = ik\beta\hat{\phi}(0) \ \text{ on } \ \Gamma. \qquad (6.9b) \end{cases}$$

The $\hat{\eta}_\pm$ and $\hat{\phi}_0$ are unknown constants and $\kappa = \sqrt{\omega^2 - k^2}$.

There are two types of solution possible. The first is defined by real κ and describes pure gravity waves with real frequency ω. The genuinely unstable mode, missed by Lukyanov et al. (2001) and considered first by Morris and Davidson (2003), is defined by complex frequencies ω. These are in turn examined in the ensuing subsections.

6.1.1 Pure gravity waves

The first solution describing pure gravity waves with real frequency $\omega = \pm\sqrt{k^2 + \kappa^2}$, is obtained by substituting Eqs. (6.8) and (6.9) in Eq. (6.7) and reads as:

$$\hat{\phi}_0 = -i\frac{\kappa}{k}\frac{\hat{\eta}_+ - \hat{\eta}_-}{\omega^2}. \tag{6.10}$$

For this solution, the boundary conditions Eq. (6.9) yield:

$$\hat{\eta}'(0) = ik\beta\hat{\phi}(0),$$

where utilising the information obtained in Eq. (6.10) yields:

$$\frac{\hat{\eta}_+ - \hat{\eta}_-}{\hat{\eta}_+ + \hat{\eta}_-} = -\frac{k}{\kappa}\frac{\beta}{(\omega^2 - i\beta)}. \tag{6.11}$$

It can be deduced, that if no electromagnetic interaction exists, i.e. $\beta = 0$, then $\hat{\eta}_+ = \hat{\eta}_-$. This results in a broken symmetry between the incident and the reflected gravity waves, such that no instability arise. Morris and Davidson (2003) question this claim by Lukyanov et al. (2001) and Molokov et al. (2011) that wave reflections from the wall lead to instability. The stability of the system is defined by the frequency of eigenmode which consists of a superposition of incident and reflected gravity waves. These are coupled by the reflection condition Eq. (6.11) and can be swapped owing to the time inversion symmetry for this problem. The respective frequency is purely real, which means that the eigenmode is neutrally stable, i.e. neither growing nor decaying.

6.1.2 Edge waves

For a complex $\kappa := i\kappa$ the exponential functions Eq. (6.8) descibe either a growing or a decaying disturbance. The resulting dispersion relation takes the form:

$$\omega^2 = k^2 - \kappa^2. \tag{6.12}$$

Consequently, the general solution of Eq. (6.7) is:

$$\begin{cases} \hat{\eta}(y) = \hat{\eta}_0 e^{-\kappa y}, & \text{(6.13a)} \\ \hat{\phi}(y) = \hat{\phi}_0 e^{-ky} + \dfrac{\hat{\eta}(y)}{\omega^2}. & \text{(6.13b)} \end{cases}$$

Similarly to Eq. (6.10) the boundary condition on the electric potential yields:

$$\hat{\phi}_0 = -\frac{\kappa}{k}\frac{\hat{\eta}_0}{\omega^2}, \tag{6.14}$$

while, in using Eq. (6.9) the respective boundary condition on the interface elevation is:

$$\hat{\eta}'(0) = ik\beta\hat{\phi}(0). \tag{6.15}$$

This relates the wavenumbers as follows:

$$\frac{\kappa}{k} = -\frac{1}{2} \pm \sqrt{\frac{1}{4} - i\frac{\beta}{k^2}}. \tag{6.16}$$

Accordingly, the dispersion relation Eq. (6.12) takes the form:

$$\frac{\omega^2}{k^2} = \frac{1}{2} + i\beta \pm \sqrt{\frac{1}{4} - i\frac{\beta}{k^2}}, \tag{6.17}$$

where complexity of frequency for $\beta \neq 0$ implies instability. For $\beta \ll k^2$, the last term can be expanded as:

$$\sqrt{\frac{1}{4} - i\frac{\beta}{k^2}} \approx \frac{1}{2} - \frac{i\beta}{k^2} + \frac{\beta^2}{k^4} + \frac{2i\beta^3}{k^6} + \dots \tag{6.18}$$

For a real positive-part of the wavenumber $\Re(\kappa) > 0$, which is required for the perturbation to be bounded far away from the wall, the expression Eq. (6.18) simplifies to:

$$\frac{\kappa}{k} \approx -\frac{i\beta}{k^2} + \frac{\beta^2}{k^4} + \frac{2i\beta^3}{k^6}, \tag{6.19}$$

while the expression for the frequency becomes:

$$\pm\frac{\omega}{k} \approx 1 + \frac{1}{2}\left(\frac{\beta}{k^2}\right)^2 + i\left(\frac{\beta}{k^2}\right)^3. \tag{6.20}$$

Therefore, Eq. (6.20) describes weakly-destabilised waves with $\Im(\omega) \propto \frac{\beta^3}{k^5}$, shown in figure 6.1, which according to Eq. (6.19) are nearly transverse $\Im(\kappa) \propto -\frac{\beta}{k}$ and slowly decaying from the edge at the rate $\Re(\kappa) \propto \frac{\beta^2}{k^3}$.

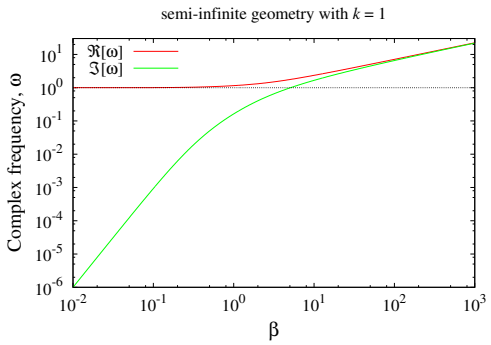

FIGURE 6.1: Edge-wave growth rate in function of the electromagnetic interaction parameter.

6.2 Finite-width channel

Suppose the fluids occupy the domain $[-1 \leq y \leq 1] \times [-\infty < x < \infty]$, which corresponds to the case of a finite-width channel first considered by Davidson and Lindsay (1998) and further studied in the context of hydromagnetic edge waves by Morris and Davidson (2003) and Molokov et al. (2011).

Then Eq. (6.7a), with the use of the dispersion relation, writes as $\hat{\eta}'' - \kappa^2\hat{\eta} = 0$. Hence, the solution to this ODE is of the form:

$$\hat{\eta} = C_1 e^{i\kappa y} + C_2 e^{-i\kappa y}.$$

Replacing the complex exponential terms with their respective trigonometric functions $e^{\pm ia} = \cos a \pm i \sin a$, yields:

$$\hat{\eta} = \hat{\eta}_+ \cos(\kappa y) + \hat{\eta}_- \sin(\kappa y), \tag{6.21}$$

where $\hat{\eta}_+$ and $\hat{\eta}_-$ are $\hat{\eta}_+ = C_1 + C_2$ and $\hat{\eta}_- = i\,(C_2 - C_1)$. Accordingly, the general solution of Eq. (6.7b) can be written as:

$$\hat{\phi} = \hat{\phi}_+ \cosh(ky) + \hat{\phi}_- \sinh(ky) + \frac{\hat{\eta}}{\omega^2}. \tag{6.22}$$

The boundary conditions for the channel are:

$$\begin{cases} \hat{\phi}'(\pm 1) = 0 \quad \text{and} & \text{(6.23a)} \\ \hat{\eta}'(\pm 1) = ik\beta\hat{\phi}(\pm 1) \quad \text{on} \quad \Gamma. & \text{(6.23b)} \end{cases}$$

The coefficients of Eq. (6.22) are defined by Eq. (6.23) as:

$$\hat{\phi}_+ = \frac{\hat{\eta}_+ \kappa \sin(\kappa)}{\omega^2 k \sinh(k)} \qquad \text{and} \qquad \hat{\phi}_- = -\frac{\hat{\eta}_- \kappa \cos(\kappa)}{\omega^2 k \cosh(k)}. \tag{6.24}$$

Consequently, substituted in Eq. (6.21) and Eq. (6.22) for the boundary conditions described in Eq. (6.23) leads to the dispersion relation:

$$\frac{\kappa}{k}\left(\frac{\omega^4}{\beta^2} + 1\right) - \frac{k}{\kappa} = \tan(\kappa)\coth(k) - \cot(\kappa)\tanh(k). \tag{6.25}$$

Rearranging Eq. (6.25), yields:

$$\beta = \frac{\omega^2}{\sqrt{\frac{k}{\kappa}\left(\frac{k}{\kappa} + \tan(\kappa)\coth(k) - \cot(\kappa)\tanh(k)\right) - 1}}, \tag{6.26}$$

which implicitly defines the spectrum of admitted κ values for given k and β. For $\beta = 0$, Eq. (6.25) reduces to $\sin 2\kappa = 0$, which defines the standard discrete eigenvalue spectrum of wave modes fitting in across the channel width: $\kappa_n = n\pi/2$, $n = 0, 1, 2, \ldots$ As seen in figure 6.2, where β defined by Eq. (6.25) is plotted against κ for various k,the increase of β just modifies the spectrum of the wave modes admitted by the electromagnetic reflection condition Eq. (6.23).

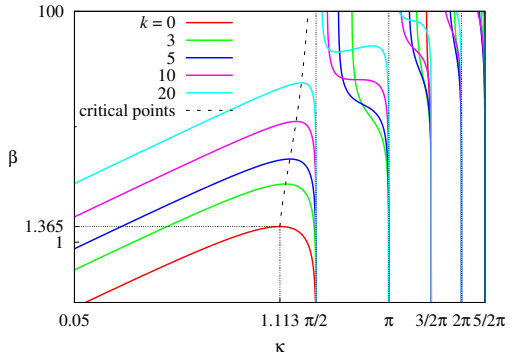

FIGURE 6.2: The electromagnetic interaction parameter β versus the admissible transverse wavenumber κ for various longitudinal wavenumbers k.

The modes remain pure gravity waves defined by the dispersion relation with real wavenumbers up to the point where two branches of κ merge together. At this point, a complex conjugate pair of wavenumbers emerges and thus the instability sets in as the frequency becomes complex (see figure 6.3).

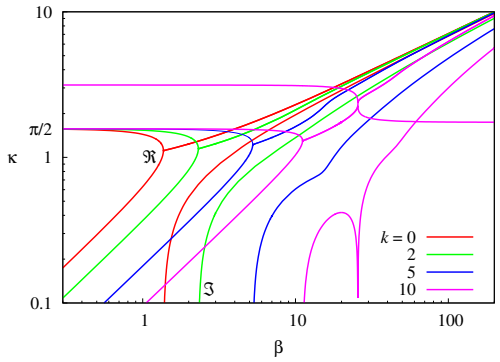

(a) Wavenumber κ as a function of β.

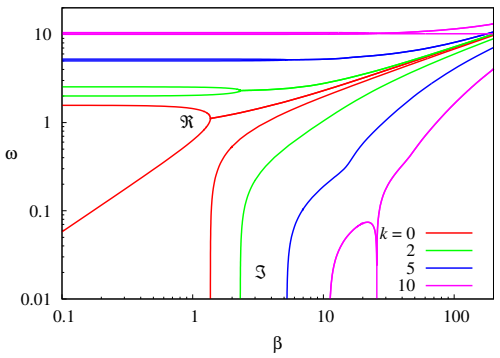

(b) Frequency ω as a function of β.

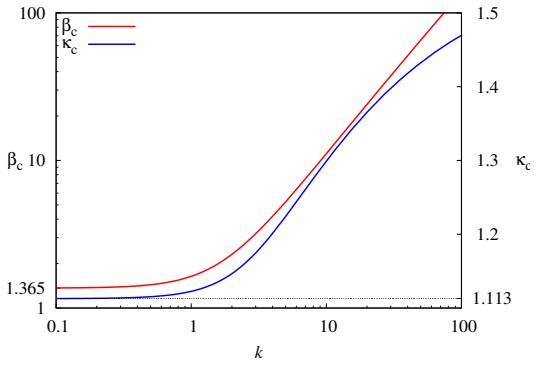

(c) The critical β and wavenumber κ as a function of k.

FIGURE 6.3: Real ($\mathfrak{R}$) and imaginary ($\mathfrak{I}$) parts of the first three transverse wavenumbers κ (a) and the respective frequencies ω (b) versus the electromagnetic interaction parameter β for various longitudinal wavenumbers k as well as (c) the critical β and transverse wavenumbers κ as functions of the longitudinal wavenumbers k.

As shown by Morris and Davidson (2003), who use the reciprocal of β as the control parameter, this happens first in the limit $k \to 0$, yielding:

$$\beta = \frac{\kappa^2}{\sqrt{\frac{\tan(\kappa)}{\kappa} - 1}}, \tag{6.27}$$

which attains a maximum $\beta_c \approx 1.365$ when two purely longitudinal gravity wave modes with $\kappa_c = 1.113$ merge. It is of note that, counter to the gravity wave modes predicted by the semi-infinite model which are transverse and emerging at $\beta_c = 0$, this critical mode is longitudinal and emerges at a finite β_c. In the channel geometry, the mode corresponding to the semi-infinite model, is recovered in the short-wave limit $k \gg 1$, which is of little practical significance as the most unstable are the long-wave modes.

6.2.1 Short-wave limit

The short-wave limit is in turn considered, with respect to the length scale but sufficiently long with respect to the height, maintaining consistency in terms of the shallow water approximation. For a complex $\kappa := i\kappa$ following the analogous procedure as in Eq. (6.25) results into:

$$\frac{\kappa}{k}\left(\frac{\omega^4}{\beta^2} + 1\right) + \frac{k}{\kappa} = \tanh(\kappa)\coth(k) + \coth(\kappa)\tanh(k). \tag{6.28}$$

The RHS of Eq. (6.28) for $k \gg 1$ simplifies into $\tanh(\kappa) + \coth(\kappa) = 2\coth(2\kappa)$ where for $\Re(\kappa) \gg 1$ the $\coth(2\kappa) = 1$. Substituting $\frac{\kappa}{k} = \chi$ and $\tilde{\beta} = \frac{\beta}{k^2}$ the dispersion relation simplifies to:

$$\chi^2\left(1 + \frac{(1-\chi^2)^2}{\tilde{\beta}^2}\right) + 1 = 2\chi, \tag{6.29}$$

the solution of which is:

$$\chi = -\frac{1}{2} \pm \sqrt{\frac{1}{4} \pm i\tilde{\beta}} \tag{6.30}$$

Ensuring a decaying spatial growth rate, i.e. $\Re(\chi) > 0$, Eq. (6.30) reads as:

$$\chi = -\frac{1}{2} + \sqrt{\frac{1}{4} \pm i\tilde{\beta}} \tag{6.31}$$

The frequency writes as:

$$\omega^2 = k^2 - \kappa^2 = k^2\left(1 - \frac{1}{2} \mp i\tilde{\beta} + \sqrt{\frac{1}{4} \pm i\tilde{\beta}}\right)$$

Using the Taylor expansion Eq. (6.18) for small values of $|\tilde{\beta}| \ll 1$ while retaining imaginary leading order terms, the frequency ω is:

$$\omega = \pm k\sqrt{1+\tilde{\beta}^2 \mp 2i\tilde{\beta}^3} \approx \pm k\left(1+\frac{\tilde{\beta}^2}{2} \mp i\tilde{\beta}^3 + O(\tilde{\beta}^4)\right). \tag{6.32}$$

analogously to Eq. (6.20).

For short waves, the marginal interaction parameter and the respective transverse wavenumber can be seen in figure 6.3c to scale as $\beta \sim k$ and $\kappa \sim 1$. The interaction parameter based on the wave length, which is the relevant horizontal length scale in this limit, then scales as $\tilde{\beta} \sim k^{-1} \to 0$.

6.2.2 Long-wave limit

Considering the long-wave limit for a purely complex κ the RHS Eq. (6.28) hyperbolic trigonometric terms are approximated using a Taylor expansion:

$$\tanh(k) = \left(k - \frac{k^3}{3}\right) + O(k^5) \quad \text{and} \quad \coth(k) = \left(\frac{1}{k} + \frac{k}{3}\right) + O(k^3).$$

Consequently, Eq. (6.28) is approximated by

$$\frac{\omega^4}{\beta^2} \approx -\frac{k^4}{3\kappa^2}\left(-2\frac{\kappa^2}{k^2} + \frac{\kappa^4}{k^4} + 1\right).$$

Using $\chi = \frac{\kappa}{k}$ and $\tilde{\beta} = \frac{\beta}{k^2}$, the expression above rewrites into:

$$\frac{\left(1-\chi^2\right)^2}{\tilde{\beta}^2} = -\frac{1}{3}k^2\chi^{-2}\left(-2\chi^2 + \chi^4 + 1\right),$$

the solution of which is:

$$\kappa = \pm i\frac{\beta}{\sqrt{3}}$$

Therefore, for $\beta \sim k \ll 1$, the frequency becomes:

$$\omega^2 = k^2 - \kappa^2 = k^2 + \frac{\beta^2}{3}. \tag{6.33}$$

6.3 Linear stability analysis of a rectangular cell

A more realistic model of a rectangular cell laterally bounded by four side walls and of aspect ratio $\alpha = L_x/L_y$ is now considered. Using the eigenvalue perturbation method, it is shown that, in the inviscid limit, rectangular cells whose aspect ratio squared equals the ratio of any two odd numbers can be destabilised by an infinitesimally weak electromagnetic interaction, while cells of other aspect ratios

have finite instability thresholds. The unstable aspect ratios form a discontinuous dense set of points which intersperse aspect ratios with finite stability thresholds.

6.3.1 Eigenvalue perturbation solution for $\beta \ll 1$

In this case, the problem does not appear to be solvable exactly but it can be approximately solved using the classical eigenvalue perturbation method (Hinch, 1991, Sec. 1.6) for small β. Namely, the eigenmode of the form:

$$\{\eta, \phi\}(\mathbf{x}, t) = \{\hat{\eta}, \hat{\phi}\}(\mathbf{x}) e^{-i\omega t} + \text{c.c.} \tag{6.34}$$

is sought by expanding the eigenvalue, which in this case is ω^2, and the amplitude distribution in the power series of β as follows:

$$\omega^2 = \lambda^{(0)} + \beta\lambda^{(1)} + \dots,$$
$$\{\hat{\eta}, \hat{\phi}\}(\mathbf{x}) = \{\hat{\eta}, \hat{\phi}\}^{(0)}(\mathbf{x}) + \beta\{\hat{\eta}, \hat{\phi}\}^{(1)}(\mathbf{x}) + \dots$$

At the leading order, which corresponds to $\beta = 0$, Eq. (6.5) reduces to

$$\lambda^{(0)}\hat{\eta}^{(0)} + \nabla^2\hat{\eta}^{(0)} = 0,\ \partial_n\hat{\eta}^{(0)}\Big|_\Gamma = 0,$$
$$\hat{\eta}^{(0)} + \nabla^2\hat{\phi}^{(0)} = 0,\ \partial_n\hat{\phi}^{(0)}\Big|_\Gamma = 0.$$

The solution of this problem is:

$$\lambda^{(0)}_{\mathbf{k}} = \mathbf{k}^2, \tag{6.35}$$
$$\{\hat{\eta}, \hat{\phi}\}^{(0)}(\mathbf{x}) = \{\mathbf{k}^2, 1\}\hat{\phi}^{(0)}_{\mathbf{k}}\Psi_{\mathbf{k}}(\mathbf{x}), \tag{6.36}$$

where

$$\Psi_{\mathbf{k}}(\mathbf{x}) = \cos(xk_x)\cos(yk_y) \tag{6.37}$$

is the gravity wave mode for the wave vector

$$\mathbf{k} = (k_x, k_y) = \pi(m/\sqrt{\alpha}, n\sqrt{\alpha}),\ \ m, n = 0, 1, 2, \dots \tag{6.38}$$

The first-order correction $\{\hat{\eta}, \hat{\phi}\}^{(1)}$ to the leading-order solution with the eigenvalue Eq. (6.35), is sought as an expansion in the leading-order eigenmodes. These may be a superposition of several eigenmodes Eq. (6.36) with the wave vectors satisfying $\mathbf{k}'^2 = \mathbf{k}^2$:

$$\{\hat{\eta}, \hat{\phi}\}^{(0)}(\mathbf{x}) = \sum_{\mathbf{k}'^2=\mathbf{k}^2} \{\hat{\eta}, \hat{\phi}\}^{(0)}_{\mathbf{k}'}\Psi_{\mathbf{k}'}(\mathbf{x}),$$

when the frequency happens to be degenerate. Consequently, the first-order correction is sought as an expansion in the leading-order eigenmodes:

$$\{\hat{\eta},\hat{\phi}\}^{(1)}(\mathbf{x}) = \sum_{\mathbf{k}} \{\hat{\eta},\hat{\phi}\}^{(1)}_{\mathbf{k}} \Psi_{\mathbf{k}}(\mathbf{x}).$$

Substituting this expansion into Eq. (6.5a) and applying the solvability condition by projecting it onto $\Psi_{\mathbf{k}}$, after a few rearrangements one obtains:

$$\lambda^{(1)}_{\mathbf{k}} \left\langle \Psi^2_{\mathbf{k}} \right\rangle k^2 \hat{\phi}^{(0)}_{\mathbf{k}} = \sum_{\mathbf{k}'^2=\mathbf{k}^2} F_{\mathbf{k},\mathbf{k}'} \hat{\phi}^{(0)}_{\mathbf{k}'}. \tag{6.39}$$

The angle brackets denote the integral over $S = L_x \times L_y$: $\left\langle \Psi^2_{\mathbf{k}} \right\rangle = \int_S \Psi^2_{\mathbf{k}} \,\mathrm{d}^2\mathbf{x} = c^{-1}_{k_x} c^{-1}_{k_y}$, where $c_0 = 1$ and $c_k = 2$ for $k \neq 0$. The RHS of Eq. (6.39) results from Green's first identity:

$$\left\langle \Psi_{\mathbf{k}} \nabla^2 \hat{\eta}^{(1)} + \nabla\Psi_{\mathbf{k}} \cdot \nabla\hat{\eta}^{(1)} \right\rangle = \oint_{\Gamma} \Psi_{\mathbf{k}} \partial_n \hat{\eta}^{(1)} \mathrm{d}\Gamma,$$

where the boundary integral can be transformed using Eq. (6.5b) and Green's theorem as follows:

$$\oint_{\Gamma} \Psi_{\mathbf{k}} \partial_\tau \hat{\phi}^{(0)} \mathrm{d}\Gamma = -\left\langle \mathbf{e}_z \cdot \nabla\Psi_{\mathbf{k}} \times \nabla\hat{\phi}^{(0)} \right\rangle.$$

This results in the electromagnetic interaction matrix

$$F_{\mathbf{k},\mathbf{k}'} = \langle \mathbf{e}_z \cdot \nabla\Psi_{\mathbf{k}} \times \nabla\Psi_{\mathbf{k}'} \rangle = G_{\mathbf{k},\mathbf{k}'} - G_{\mathbf{k}',\mathbf{k}}, \tag{6.40}$$

where $G_{\mathbf{k},\mathbf{k}'} = H_{k_x,k'_x} H_{k'_y,k_y}$ and

$$H_{k_m,k_n} = k_m \langle \sin(xk_m)\cos(xk_n) \rangle = \frac{2m^2}{m^2-n^2} \mathrm{mod}(m+n,2). \tag{6.41}$$

The anti-symmetric nature of Eq. (6.40) means that there is no electromagnetic back-reaction on separate gravity wave modes, i.e., $F_{\mathbf{k},\mathbf{k}} = 0$. Thus, for a single (non-degenerate) mode, this is construed as:

$$\lambda^{(1)}_{\mathbf{k}} \left\langle \Psi^2_{\mathbf{k}} \right\rangle k^2 \hat{\phi}_{\mathbf{k}} = F_{\mathbf{k},\mathbf{k}} \hat{\phi}_{\mathbf{k}} = 0,$$

which means no electromagnetic effect of order β. For a degenerate mode consisting of a superposition of two eigenmodes with the same frequency:

$$\lambda^{(0)}_{\mathbf{k}} = \mathbf{k}_1^2 = \mathbf{k}_2^2, \tag{6.42}$$

Equation (6.39) takes the form:

$$\lambda_{\mathbf{k}}^{(1)} k^2 \begin{pmatrix} \left\langle \Psi_{\mathbf{k}_1}^2 \right\rangle \hat{\phi}_{\mathbf{k}_1} \\ \left\langle \Psi_{\mathbf{k}_2}^2 \right\rangle \hat{\phi}_{\mathbf{k}_2} \end{pmatrix} = \begin{pmatrix} 0 & F_{\mathbf{k}_1,\mathbf{k}_2} \\ -F_{\mathbf{k}_1,\mathbf{k}_2} & 0 \end{pmatrix} \begin{pmatrix} \hat{\phi}_{\mathbf{k}_1} \\ \hat{\phi}_{\mathbf{k}_2} \end{pmatrix}. \tag{6.43}$$

The solution of this matrix eigenvalue problem yields:

$$\lambda_{\mathbf{k}}^{(1)} k^2 \sqrt{\left\langle \Psi_{\mathbf{k}_1}^2 \right\rangle \left\langle \Psi_{\mathbf{k}_2}^2 \right\rangle} = \pm i F_{\mathbf{k}_1,\mathbf{k}_2}, \tag{6.44}$$

signifying an imaginary $\lambda_{\mathbf{k}}^{(1)}$ and thus, an instability in the system if $F_{\mathbf{k}_1,\mathbf{k}_2} \neq 0$. According to Eq. (6.41), this is the case only if both components of wave vectors $\mathbf{k_1} = \pi(m_1/\sqrt{\alpha}, n_1\sqrt{\alpha})$ and $\mathbf{k_2} = \pi(m_2/\sqrt{\alpha}, n_2\sqrt{\alpha})$ have opposite parities; namely, $m_1 \pm m_2$ and $n_1 \pm n_2$ are odd numbers. Then the degeneracy condition from Eq. (6.42) yields:

$$\alpha_c^2 = -\frac{(m_1 - m_2)(m_1 + m_2)}{(n_1 - n_2)(n_1 + n_2)} = \frac{m}{n},$$

where m and n are odd numbers. It means that all cells with aspect ratios squared equal to the ratio of two odd numbers are inherently unstable, i.e., they become unstable at infinitesimal $\beta > \beta_c = 0$.

For a square cell, which corresponds to $\alpha^2 = 1$, the unstable wave numbers are $m_1 = l$, $n_1 = 0$ and $m_2 = 0$, $n_2 = l$, where n is an odd number. In this case, Eq. (6.44) yields $\lambda_l^{(1)} = \pm i8/(l\pi)^2$ and thus

$$\Im[\omega_n^{(1)}] = \pm \frac{4}{(n\pi)^3}, \tag{6.45}$$

which means that the most unstable is the mode with $n = 1$. For general $\alpha^2 = m/n$ with odd m and n, the lowest unstable wavenumbers are:

$$m_{(3\mp1)/2} = (m \pm 1)/2, \tag{6.46}$$

$$n_{(3\pm1)/2} = (n \pm 1)/2. \tag{6.47}$$

In this case, Eq. (6.44) yields $\lambda_{m,n}^{(1)} = \pm i8 c_{m-1}^{1/2} c_{n-1}^{1/2}/(\pi^2\sqrt{mn})$ which respectively designates:

$$\Im[\omega_{m,n}^{(1)}] = \pm \frac{8}{\pi^3} \left(\frac{c_{m-1} c_{n-1}}{(m+n)(1+mn)\sqrt{mn}} \right)^{1/2}, \tag{6.48}$$

which reduces to Eq. (6.45) with $l = 1$ when $m = n = 1$.

For an aspect ratio α sufficiently close to the critical value $\alpha_c = \sqrt{m/n}$, the stability of system can be expected to be determined by the interaction of two modes with the wave numbers Eqs. (6.46) and (6.47) which correspond to the

wavenumbers

$$\mathbf{k}_{(3\mp1)/2} = \frac{\pi}{2}\left((m \pm 1)/\sqrt{\alpha}, (n \mp 1)\sqrt{\alpha}\right).$$

Then ω^2 is defined by the following second-order matrix eigenvalue problem:

$$\begin{pmatrix} (\omega^2 - \mathbf{k}_1^2)\mathbf{k}_1^2 & \beta F_{\mathbf{k}_1,\mathbf{k}_2} c_{n-1} \\ -\beta F_{\mathbf{k}_1,\mathbf{k}_2} c_{m-1} & (\omega^2 - \mathbf{k}_2^2)\mathbf{k}_2^2 \end{pmatrix} \begin{pmatrix} \hat{\phi}_{\mathbf{k}_1} \\ \hat{\phi}_{\mathbf{k}_2} \end{pmatrix} = \mathbf{0}, \tag{6.49}$$

where $F_{\mathbf{k}_1,\mathbf{k}_2} = \frac{2(m+n)(mn+1)}{mn}$. Note that Eq. (6.49) reduces to Eq. (6.43) when $\alpha \to \alpha_c$ and $\beta \to 0$. As before, for the system to be stable, the eigenvalue ω^2 has to be real, which is the case if $\beta \le \beta_{m,n}$, where

$$\begin{aligned} \beta_{m,n} =& \frac{\pi^4}{16} \frac{\left|\alpha_c^2/\alpha^2 - 1\right| mn^2}{(m+n)(mn+1)} \\ &\times \left(\frac{(m^2-1)^2 + \alpha^4(n^2-1)^2 + 2\alpha^2((m+n)^2 + (mn+1)^2)}{c_{m-1}c_{n-1}} \right)^{1/2}. \end{aligned} \tag{6.50}$$

As shown in the next section, this approximate analytical solution agrees very well with the numerical solution of the full eigenvalue problem.

6.3.2 Numerical solution of the matrix eigenvalue problem

For general β, Eq. (6.34) leads to

$$\lambda\hat{\eta} + \nabla^2\hat{\eta} = 0, \qquad \partial_n\hat{\eta}|_\Gamma = \beta\, \partial_\tau\hat{\phi}\big|_\Gamma, \tag{6.51}$$

$$\hat{\eta} + \nabla^2\hat{\phi} = 0, \qquad \partial_n\hat{\phi}\big|_\Gamma = 0, \tag{6.52}$$

which is an eigenvalue problem for $\lambda = \omega^2 + \mathrm{i}\gamma$, where γ is the friction coefficient. The problem can be discretised using Galerkin method with the gravity wave modes Eq. (6.37) as basis functions (Sneyd and Wang, 1994), which leads to the generalisation of Eq. (6.39):

$$(\lambda - \mathbf{k}^2)\mathbf{k}^2 \left\langle \Psi_{\mathbf{k}}^2 \right\rangle \hat{\phi}_{\mathbf{k}} = \beta \sum_{\mathbf{k}'} F_{\mathbf{k},\mathbf{k}'} \hat{\phi}_{\mathbf{k}'},$$

with the electromagnetic interaction matrix on the RHS defined by Eq. (6.40). This is a matrix eigenvalue problem of size $(M+1)^2 \times (N+1)^2$, where M and N are the cut-off limits of the x and y components of the wave vectors Eq. (6.38). Alternatively, Eq. (6.51) and Eq. (6.52) can be discretised using the Chebyshev collocation method. For more information on the Chebyshev collocation method refer to (Boyd, 2013).

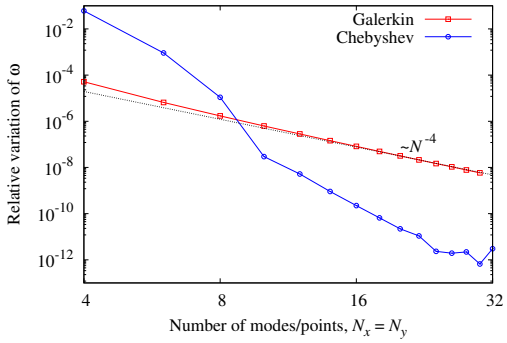

FIGURE 6.4: The relative variation of the complex frequency with the largest imaginary part ($\omega = 3.14455 + \mathrm{i}0.12889$) versus the number of modes and nodes used in the Galerkin and Chebyshev approximations for $\alpha = \beta = 1$.

As seen in figure 6.4, the Chebyshev collocation method has a significantly faster convergence rate than $\sim N^{-4}$ achieved by the Galerkin approximation with N modes in each direction. As the relative accuracy of Chebyshev collocation approximation saturates at $\approx 10^{-11} \cdots 10^{-12}$ when $N \gtrsim 24$, in the following analysis $16 \cdots 24$ collocation points have been used in each direction.

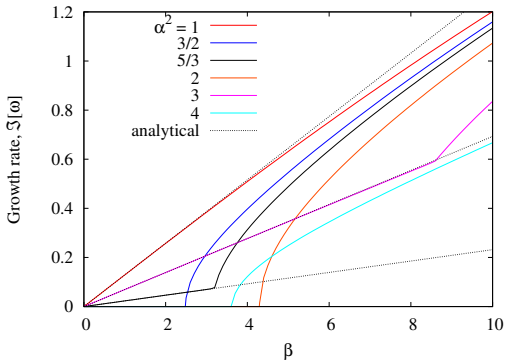

FIGURE 6.5: The largest growth rate $\Im[\omega]$ depending on the interaction parameter β for various aspect ratios α computed by the Chebyshev collocation method with $N_x = N_y = 16$ points. For α equal ratio of two odd numbers, numerical results are compared with the approximate analytical solution Eq. (6.48).

The largest growth rate $\omega_i = \Im[\omega]$, which is computed using Chebyshev collocation method with $N_x = N_y = 16$ points and plotted in figure 6.5 against the interaction parameter β for various aspect ratios α, confirms the eigenvalue perturbation solution obtained in the previous section. Namely, for α^2 equal to the ratio of two odd numbers, the growth rate becomes positive at $\beta > \beta_c = 0$ whereas for other aspect ratios this happens at finite β_c. The dependence of the instability threshold β_c on the aspect ratio squared is shown in figure 6.6 for various viscous friction coefficients γ. Without friction ($\gamma = 0$), which for numerical reasons is modelled by setting $\gamma = 10^{-5}$, the stability diagram is very rugged containing

both small and large scale regular patterns. The key feature are the dips in β_c which can be seen to occur at α_c^2 equal to ratio of odd numbers as predicted by the eigenvalue perturbation analysis in the previous section.

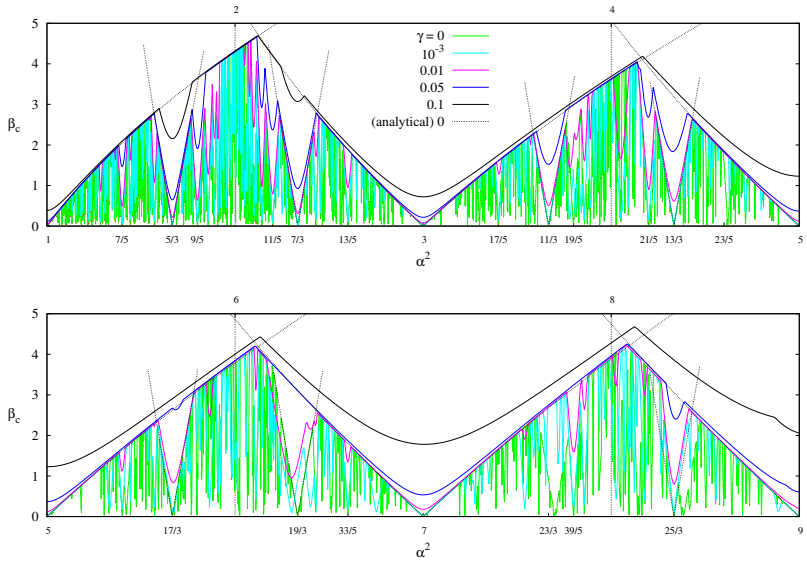

FIGURE 6.6: Instability threshold β_c depending on the aspect ratio squared (α^2) computed for various viscous friction coefficients γ using Chebyshev collocation method with $N_x = N_y = 16 \cdots 24$ points. Analytical solution Eq. (6.50) is plotted for the dominant critical points α_c^2 equal to odd numbers and their thirds.

The increase of the friction coefficient gradually smooths out the dependence of β_c on α, especially at small scales and larger aspect ratios. However, the main feature of the stability diagram, which is the location of minima and maxima of β_c in the vicinity of odd and even values of α^2, respectively, persists with the increase of γ. It is remarkable that the approximate solution Eq. (6.50) for the dominant critical points closely reproduces numerical results obtained with $N_x = N_y = 24$ collocation points up to $\alpha^2 \approx 5$. The slight deviation of the numerical results from the theoretical predictions, which emerges at $\alpha^2 \gtrsim 5$, especially in the vicinity of higher order critical points, is due to the reduced numerical resolution as the collation grid becomes stretched out at large aspect ratios.

Chapter 7

Simulation of the nonlinear interfacial-wave instability

In this chapter the numerical results of the two-layer system of equations are presented, the analysis of which is carried out in three stages. First, notwithstanding the excellent agreement of the numerical and the theoretical results, presented in §4.2.3 for discontinuous initial states, the stability properties of the 1D hydrodynamic scheme, presented in §2.9 are further examined with particular attention to the long term evolution and the dependence of dissipation on the relevant control parameters. In turn, these results are contrasted with the ones obtained by the corresponding non-conservative 2D scheme, presented in §3.1, for which the interface has been cosinusoidally excited with a single 1D gravity wave-mode along either of the horizontal directions as well as an analogous 2D perturbance. Lastly, the behaviour of the 2D bilayer MHD system is explored for various parameters and a discussion is made in regards to cause and manner upon which the break-down of the solution occurs.

7.1 1D code verification for smooth initial data

In the presence of discontinuous/sharp interface heights, such as the ones investigated in §4.2.3, the two-layer system was studied with the use of the conservative equations Eq. (4.14) and Eq. (4.18) – Eq. (4.20). As it has been discussed though in §4.2.3, that set of equations is equivalent to Eq. (4.7) as long as the solution is continuous. Nevertheless, aiming towards providing a benchmark to the 2D system which is in non-conservative form, the analogous 1D frictionless set of equations is used.

Provided a smooth initial interface perturbation, the 1D bilayer system has been numerically investigated using the non-conservative momentum Eq. (4.7)

and the 1D Lax-Wendroff scheme. In the 1D system, the pressure gradient which was previously eliminated in Eq. (4.18) – Eq. (4.20), is now replaced in the momentum conservation equation for each layer with an explicit but non-conservative expression resulting from the sum of momentum conservation equations. This provides an explicit solution for the pressure gradient which is equivalent to that produced by the respective Poisson solver. This approach is used to validate the Poisson solver. The latter is subsequently used to solve the respective 2D problem for which the pressure gradient cannot be eliminated as in the 1D case.

7.1.1 Two layers with equal thicknesses

In this section the thicknesses of the respective layers are set to be equal, which means that the interface oscillates about the mid-plane $z = 0$.

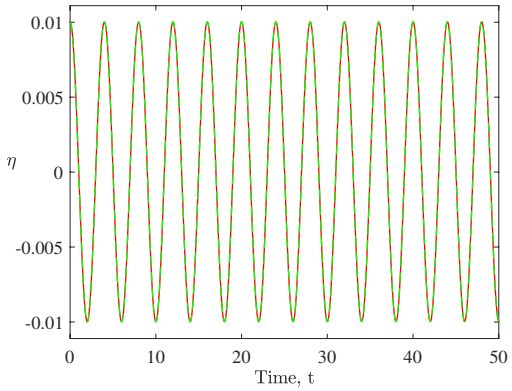

(a) Zoom in of figure 7.1b.

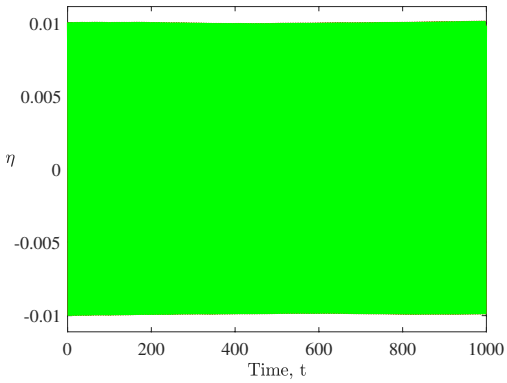

(b) Evolution of the interface height.

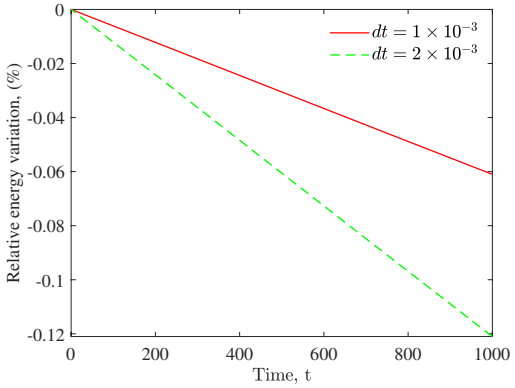

(c) Relative energy dissipation.

FIGURE 7.1: Relative energy and interface height for an initial perturbation of amplitude $A = 0.01$ using $n_x = 100$ grid points.

The numerical simulation run with two temporal discretisations $dt = 10^{-3}$ and $dt = 2 \cdot 10^{-3}$, which allows an investigation of the energy conservation and its dependence on the scheme's time-stepping parameter. Figure 7.1 illustrates the long-time evolution of the interface height at the grid's fixed position $x = 0$ as well as the relative energy variation $E(t)/E(0) - 1$, for an initial gravity wave $A\cos(\pi x)$ of amplitude $A = 0.01$. The results indicate that for a smooth and small initial perturbation the system manifests a non-increasing modulating wave amplitude. The evolution of the amplitude is practically indistinguishable for the two different temporal discretisations, the effect of which though on the energy dissipation can be seen in figure 7.1c whereupon decreasing the time step results in a lower energy dissipation.

The aforementioned observations are more profound in figure 7.2 where the amplitude is set at $A = 0.1$. In this case, owing to the increased amplitude the effect of the non-linear terms on the evolution becomes relevant in figure 7.2b. However, the flow still exhibits a stable behaviour with a gradual decay of the total amplitude due to the scheme's intrinsic numerical dissipation.

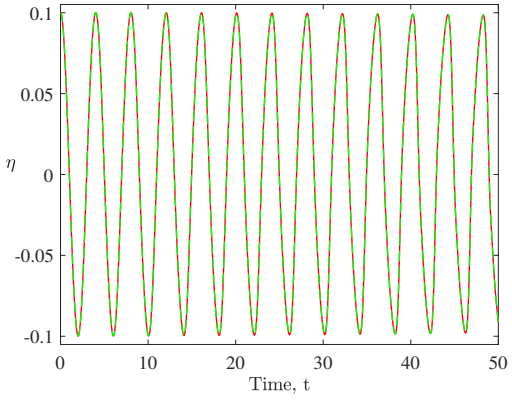

(a) Zoom in of figure 7.2b.

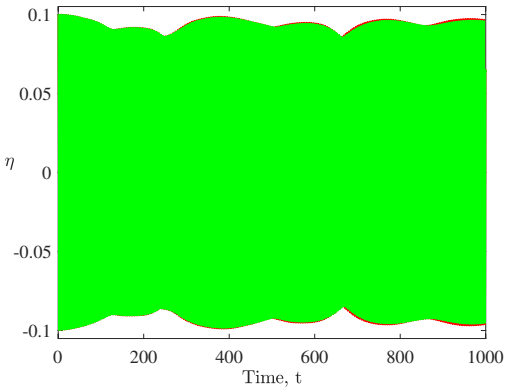

(b) Evolution of the interface height.

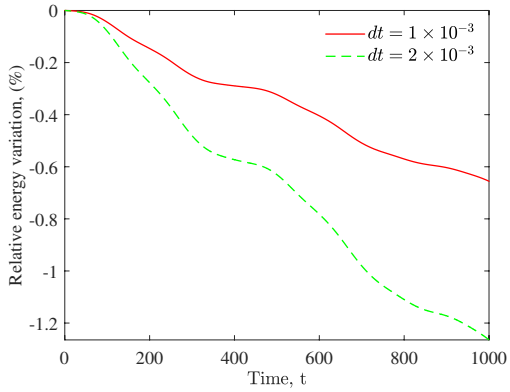

(c) Relative energy dissipation.

FIGURE 7.2: The evolution for an initial perturbation of amplitude $A = 0.1$ using $n_x = 100$ spatial grid-points.

The effects on the energy dissipation become clear for a large initial amplitude of $A = 0.5$. In this case the wave steepens quickly resulting in huge energy losses as illustrated in figure 7.3.

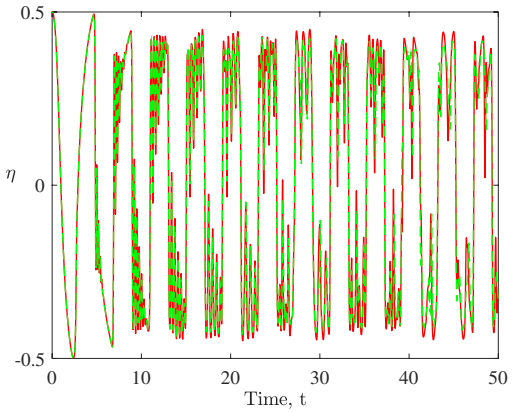

(a) Zoom in of figure 7.3b.

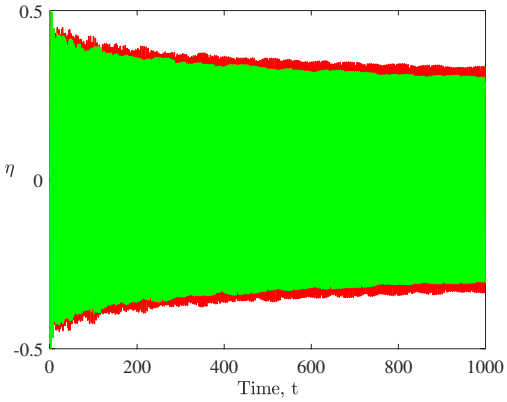

(b) Evolution of the interface height.

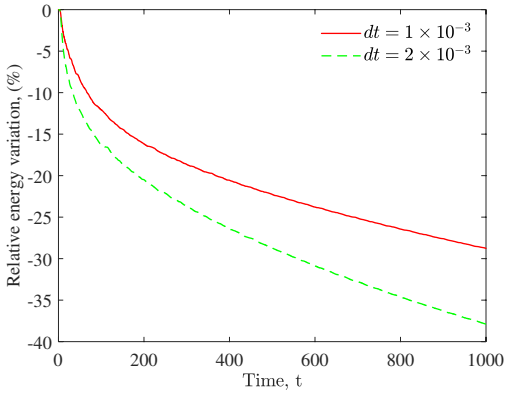

(c) Relative energy dissipation.

FIGURE 7.3: The evolution for an initial perturbation of amplitude $A = 0.5$ using $n_x = 100$ spatial grid-points.

For layers of equal thickness figures 7.1 and 7.2 show no wave breaking for small amplitudes is expected to take long time to develop, if at all. On the other hand, increasing the initial wave amplitude, as shown in figure 7.3, demonstrates clearly the energy dissipation setting in rather abruptly as expected for the wave breaking.

7.1.2 Two layers with unequal thicknesses

The system exhibits a significantly different behaviour when the liquid layers have different average thicknesses. For comparison, the Lax-Wendroff scheme is used to solve the semi-conservative momentum equation involving pressure Eq. (4.7) as well as the conservative equations of circulation Eq. (4.18) and momentum Eq. (4.19b).

In figure 7.4, where the thicknesses of the layers are different, even for a small amplitude of $A = 0.01$ the system exhibits to steepened waves almost straight away with considerable energy dissipation. The evolution of waves in figure 7.4b, where the lower layer occupies 1/4 of the total height, are vertically mirrored in figure 7.4c, where the lower layer occupies 3/4 of the height, while both cases have the same energy dissipation.

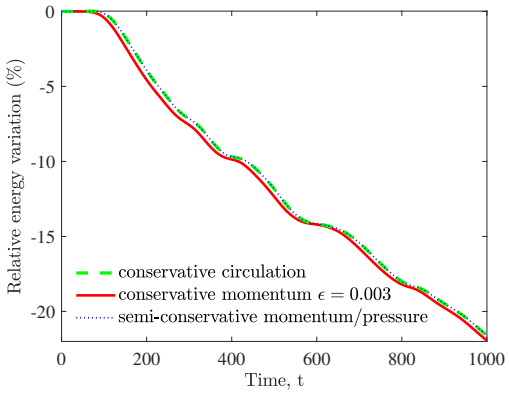

(a) Energy variation.

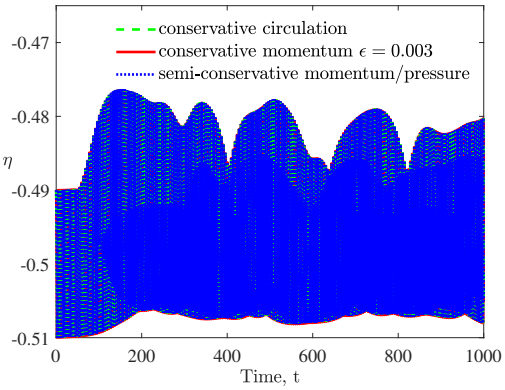

(b) Average interface location $z = -0.5$.

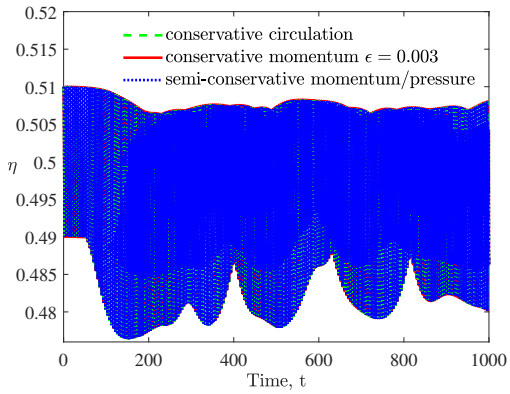

(c) Average interface location $z = +0.5$.

FIGURE 7.4: The time evolution of unequal thickness for an initial perturbation of amplitude $A = 0.01$ using a spatial resolution $n_x = 100$.

In figure 7.5, illustrating an initial amplitude of $A = 0.1$, the steepened waves become even more radical, introducing spurius oscillations from the onset of the simulation, and thus resulting in to noticeable energy dissipation.

Nevertheless, it should be noted that all three numerical solutions produce almost identical results for smooth small-amplitude initial perturbations. However, for larger ones, as seen in figure 7.5a, although the results are still comparable, there is a small but noticeable difference. This difference is likely due to the fact that the equation referred to as *semi-conservative momentum/pressure* is not fully conservative and hence cannot adequately model steep waves.

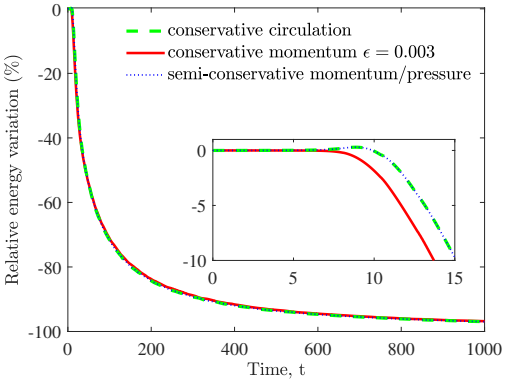

(a) Energy variation.

(b) Interface location $z = -0.5$.

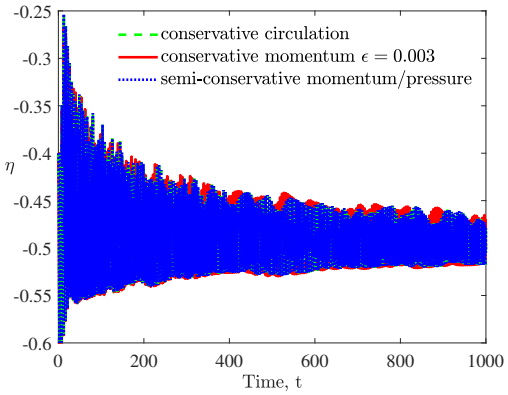

(c) Interface location $z = +0.5$.

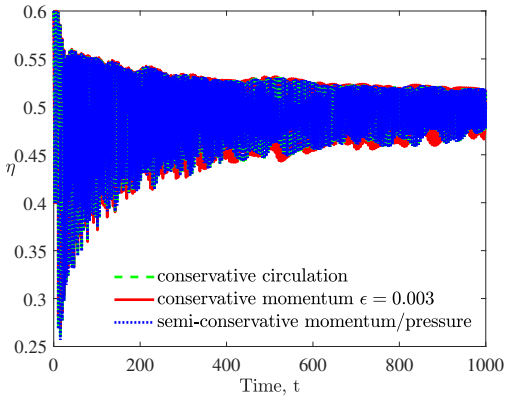

FIGURE 7.5: The evolution for layers unequal thicknesses with an initial perturbation amplitude $A = 0.1$ using $n_x = 100$ equally-spaced grid-points.

On the other hand, as discussed in §4.2.3, the circulation conservation law is not likely to produce physical solutions for such waves because of not satisfying the momentum balance. Moreover, it is not currently obvious how to formulate fully conservative 2D circulation and momentum conservation laws.

7.2 Validation of the 2D codes using 1D solutions

In this section, a comparison is made between the 1D and the 2D codes, for the gravity waves $A\cos(xk_x)\cos(yk_y)$ of mode $(0,1)$, $(1,0)$ and $(1,1)$. In contrast to the 1D problem, in the 2D case the pressure gradient cannot be found directly without solving the respective Poisson equation. This is because, in 2D the mass flux in each layer has one more degree of freedom, the direction, which precludes explicit relation between these fluxes resulting from the mass conservation as in 1D. Namely, zero divergence of the sum of two 2D mass fluxes just means

that this sum is a solenoidal field which is not necessarily a constant field as in 1D. Such an assumption is too constrictive and in general incompatible with the irrotationality of the 2D pressure gradient. This is the principal difference from the 1D case which makes the solution of the Poisson equation in 2D necessary. The 2D Poisson equation requires an explicit solution using the DCT-TDMA algorithm, presented in §3.2.3, on Eq. (2.41).

The numerical results of the interface motion presented in figure 7.6 are computed for $N_x \times N_y = 48 \times 48$ points ($N_x = 48$ in 1D) and a temporal discretisation of $dt = 10^{-2}$ for an initial amplitude of $A = 0.1$.

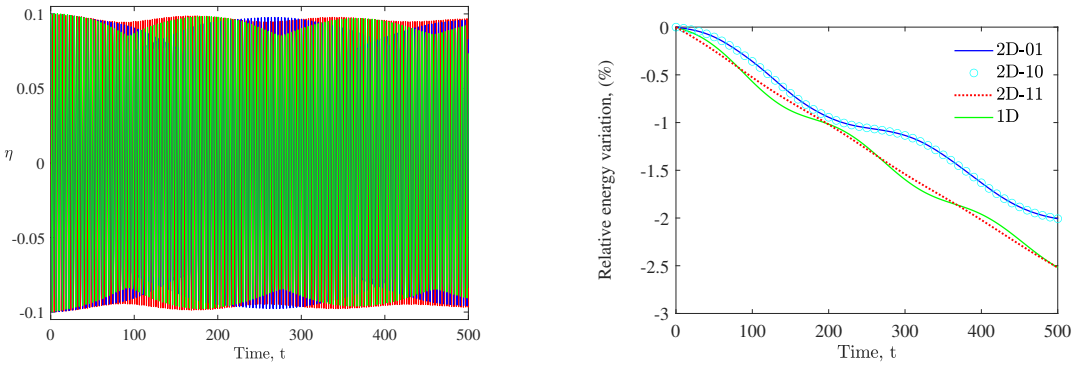

(a) Height (b) Energy

FIGURE 7.6: The 2D numerical solution of gravity waves obtained with $N_x \times N_y = 48 \times 48$; $dt = 10^{-2}$ for the wave modes $(0,1)$, $(1,0)$ and $(1,1)$ cosinusoidally with initial amplitude $A = 0.1$.

The energy dissipation shown in figure 7.6b for the modes $(0,1)$, $(1,0)$ and $(1,1)$ for the 2D scheme is contrasted with the dissipation exhibited by the 1D scheme. It is evident that the mode $(0,1)$ yields identical results to $(1,0)$. Moreover, the $(1,1)$ wave mode, presented for comparison purposes, follows closely. More importantly, the energy dissipated both by the 2D scheme as well as the 1D scheme is comparable while all remain within the bounds of their initial amplitude. This modulation of the wave amplitude is not as profound for small amplitude waves. However, for larger amplitude waves there exists an energy exchange between the wave modes which is gradually transferred onto the higher frequency modes.

7.3 2D simulation of the MHD interfacial-wave instability

In this section, numerical results, obtained using the 2D nonlinear two-layer shallow-water model are presented to demonstrate the evolution of electromagnetically driven interfacial wave instability. In figure 7.7, results concerning a square cell of aspect ratio $Lx/Ly = 1$ are plotted.

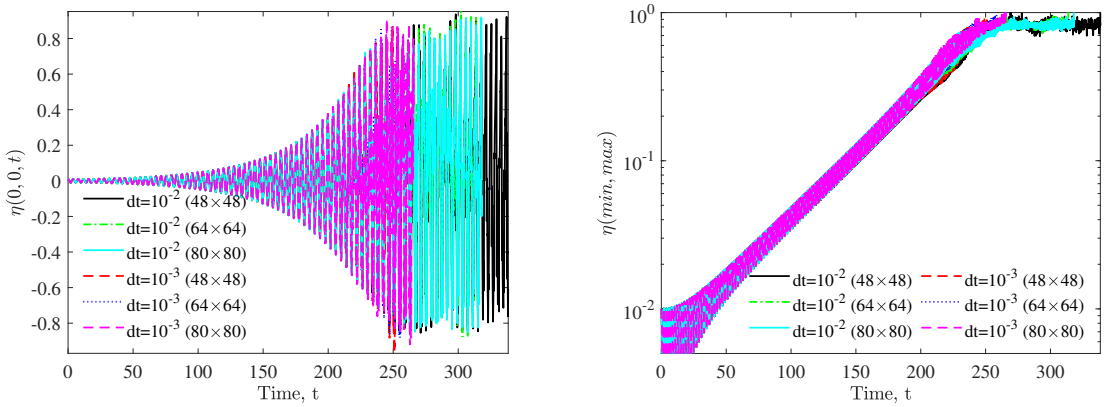

(a) Interface height

(b) The extrema of height

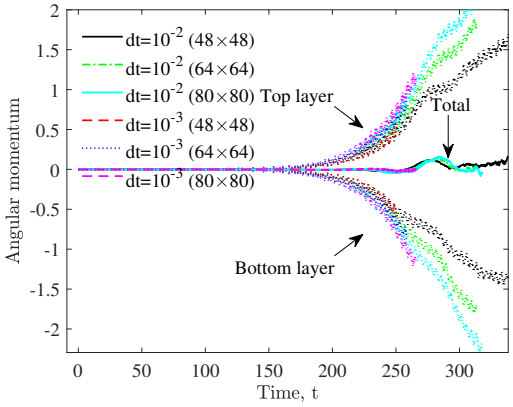

(c) Angular momentum

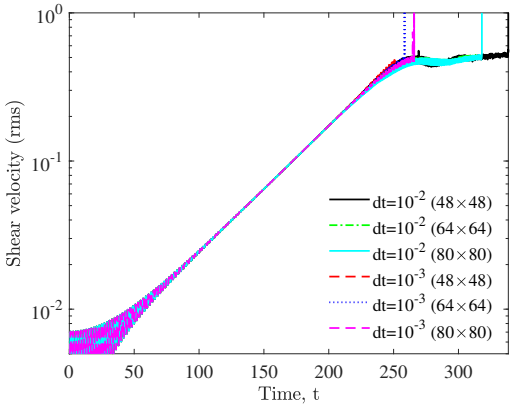

(d) Shear velocity

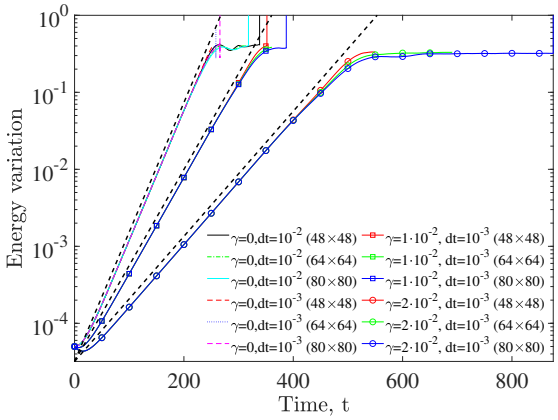

(e) Energy variation

FIGURE 7.7: The MHD problem with $\beta = 0.075$, the interface centred at $z = 0$ and an initial amplitude of $A = 0.01$.

As shown in §6.3, the square geometry is unstable for nonzero β. In the following, the EM parameter is set to $\beta = 0.075$, and numerical solutions for three different grid sizes as well as two temporal discretisations are compared. This allows us to assess the effect of numerical parameters on the solution. Figure 7.7e shows the energy of an unstable perturbation against the time for an interface initially located at the midplane and perturbed by a gravity wave mode $(0, 1)$ with the dimensionless amplitude $A = 0.01$. The variation of the interface height at the corner point $(x, y) = (0, 0)$ is shown in figure 7.7a. Without viscous friction, the instability, which initially grows exponentially, appears to saturate as the interfacial waves approaches the top and bottom boundaries.

The simulation breaks down when the interface reaches either the top or bottom boundary. The breakdown is related to the intensifying shear velocity, $\int_s (\mathbf{u}_+ - \mathbf{u}_-)^2 \, dS$, which develops between the two fluids as seen in figure 7.7d. The rotating interfacial-wave that is generated due to to the Lorentz force drives the fluids into a counter-rotating motion between the top and bottom layers, as seen in figure 7.7c, where there is a separation of the angular momentum, $e_z \cdot \int_s \mathbf{r} \times \mathbf{u} \; dS$, of the two layers. This spinning motion leads to the development of an overcritical shear velocity that escalates towards the critical value of 1 which marks the limit of hyperbolicity in 1D systems (Stewart and Dellar, 2013), at which a Kelvin-Helmoltz-type of instability develops. In figure 7.7e in addition to the frictionless case, the solutions shown are for non-zero, and equal, linear friction coefficients . The results for the linear friction $\gamma_\pm = 0.01$ and $\gamma_\pm = 0.02$ are plotted in figure 7.7e where, as anticipated, an increase of the frictional forces dissipate energy. Additionally, a coarser discretisation (either temporal or spatial) results in an increase of the numerical dissipation which in turn dampens the motion allowing the system to run longer before breaking down. Within the same grid sizes the solution for smaller timestep always breaks down sooner. This is shown in figure 7.7a, where for $N_x \times N_y = 80 \times 80$ the run of the simulation with time-step $dt = 10^{-3}$ breaks down sooner than the other case for $dt = 10^{-2}$.

When the interface located at $z = 0.5$ as shown in figure 7.8 is perturbed with a gravity wave mode $(0, 1)$ with amplitude of $A = 0.01$, the motion changes drastically and at a faster rate compared to the midplane case shown in figure 7.7. Compared to figure 7.7a, the interfacial amplitude in figure 7.8a is significantly dampened due to the sharp interface motion which augments the energy dissipation as seen in figure 7.8e. Additionally, figure 7.8c shows the total angular momenta of both layers emerge earlier but of lower magnitude than in the symmetric case shown in figure 7.7c.

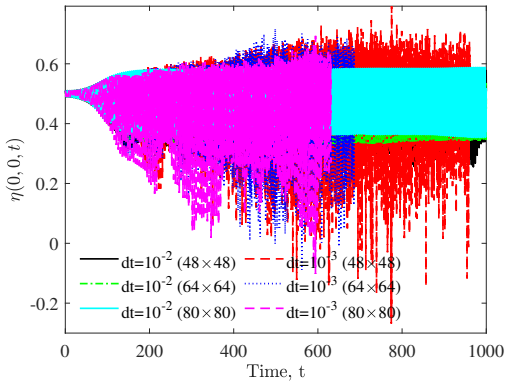

(a) Interface height

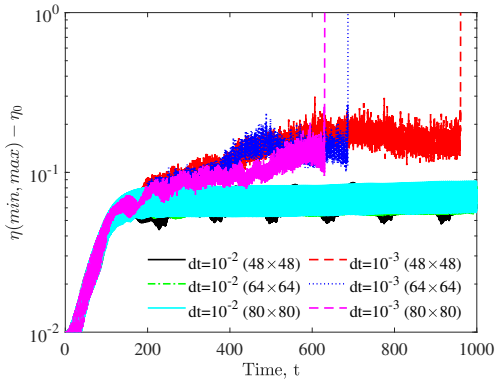

(b) The extrema of height

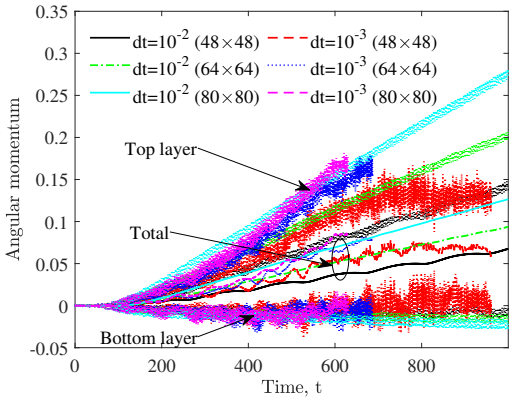

(c) Angular momentum

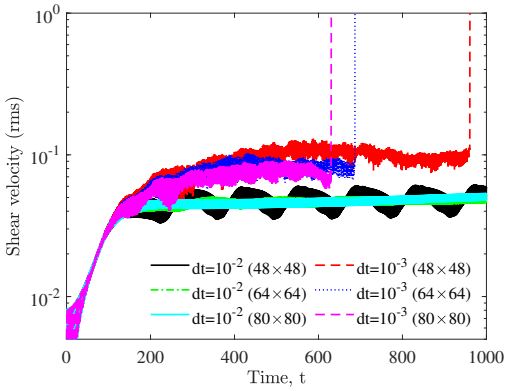

(d) Shear velocity

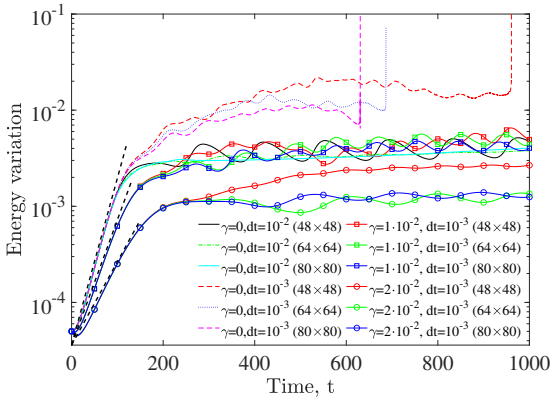

(e) Energy variation

FIGURE 7.8: The MHD problem with $\beta = 0.075$, the interface centred at $z = 0.5$ and an initial amplitude of $A = 0.01$.

Along with the results of the symmetric and asymmetric thicknesses, shown in figures 7.7 and 7.8, the corresponding linear stability growth rates for energy are plotted in figures 7.7e and 7.8e. Due to the different scalings used in the nondimensionalisation of the linear and nonlinear parts in this study the imaginary part of frequency, given by Eq. (6.45), must be scaled with $\tau = L/C$ where $C = \sqrt{2gH\left[\varrho\right]/\{\varrho\}}$. Thus, a simple expression can be obtained for the growth rate curves proportional to $8\beta/\left(\pi^3\left(\bar{h}_+\bar{h}_-\right)^{1/2}\right) - \gamma$. This is illustrated in figures

7.7e and 7.8e by the dashed black lines. The results of the numerical simulation,

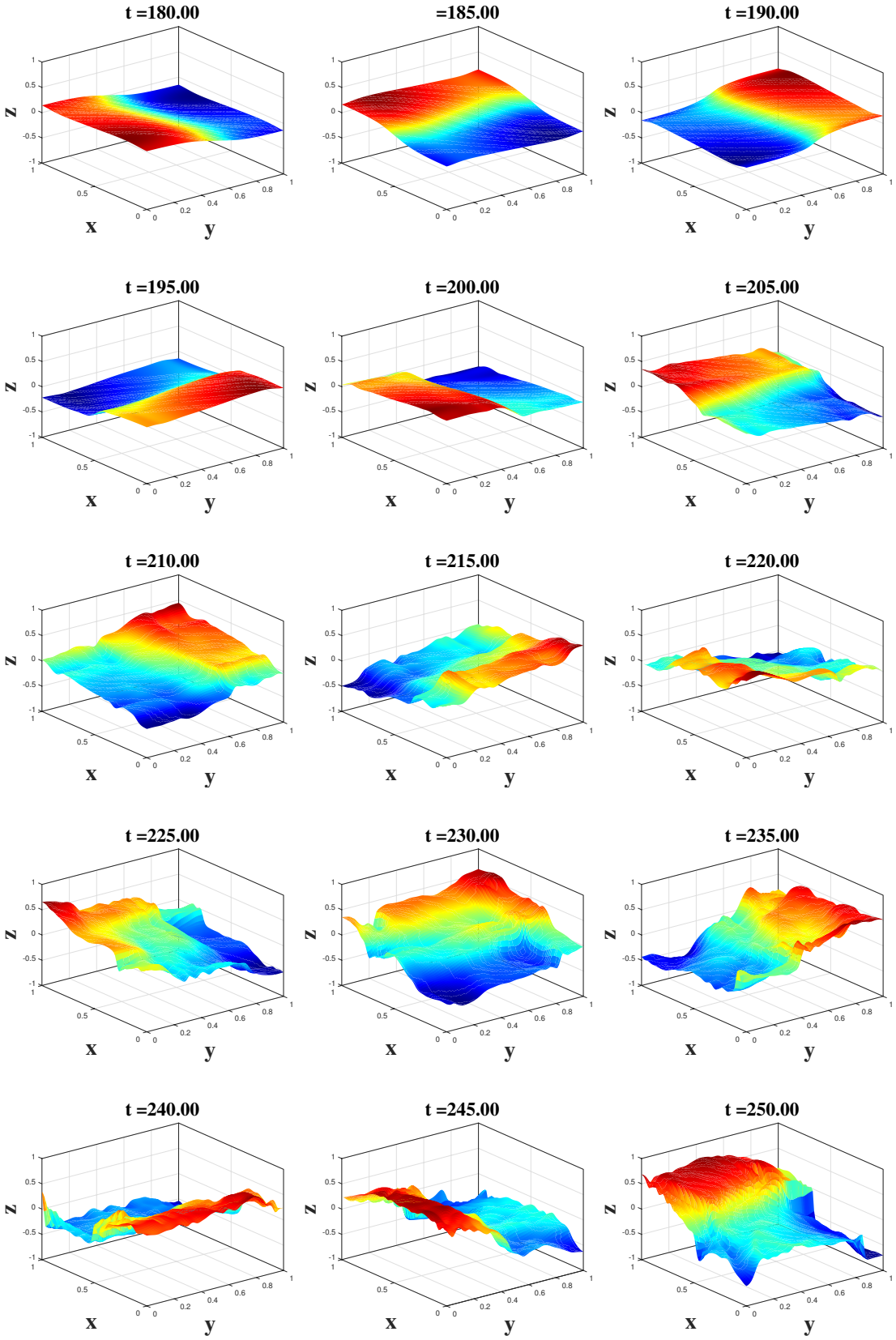

FIGURE 7.9: Interface snapshots for $\beta = 0.075$ and the interface centred at $z = 0.0$ for an initial amplitude of $A = 0.01$ for the gravity wave mode $(0, 1)$.

for electromagnetically destabilised small-amplitude interfacial waves, can be seen to be in good agreement with the growth rates produced by the linear stability.

The rotating interfacial motion of a $(0, 1)$ gravity wave mode is illustrated in figure 7.9, where the sequence of frames shown correspond to the grid size $N_x \times N_y = 80 \times 80$ with the time-step $dt = 10^{-3}$. The evolution of the interface is shown to develop short-wave instabilities when exceeding a certain critical value of the the shear velocity, which is plotted in figure 7.7d. This leads to a Kelvin-Helmholtz-type instability which eventually causes the interface to break down, prior to the interface reaching the upper or lower boundaries.

Figure 7.10 shows the energy evolution of a square cell initially perturbed with a gravity wave mode $(1, 1)$ for the same range of parameters seen in figure 7.7. As mentioned in §6, the cancellation of separate gravity modes up to first order of β suppress the electromagnetic effects. Thus, as seen in figure 7.10 this leads to a stably oscillating interface at initial times. The shear instability leads to oscillations at later stages of the simulation where the energy is seen to exponentially increase. Nevertheless, the sudden energy increase may still reach a plateau-like state, as seen in figure 7.10b, where it grows at a lower rate.

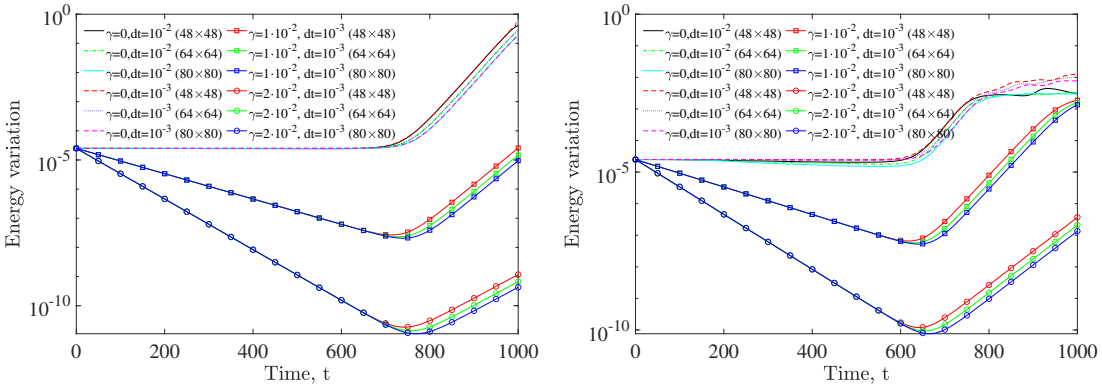

(a) Energy variation $z = 0$ (b) Energy variation $z = 0.5$

FIGURE 7.10: The energy variation for a rectangular cell with $\beta = 0.075$ and a $(1, 1)$ gravity wave mode with an initial amplitude of $A = 0.01$.

The numerical results concerning a rectangular cell of aspect ratio $L_x/L_y = 2$ are plotted in figures 7.11–7.13 for a range of the parameter β and an initial $(1, 0)$ mode perturbance of amplitude $A = 0.01$. Figure 7.11 shows the stable evolution of a slowly increasing interface motion for a small but finite value of β. In contrast to square cells where instabilities develop for $\beta > 0$, it can be seen that for $\beta = 0.5$ the interface height and energy variation for both the symmetric and asymmetric layer depths gradually evolve in absence of strong instabilities.

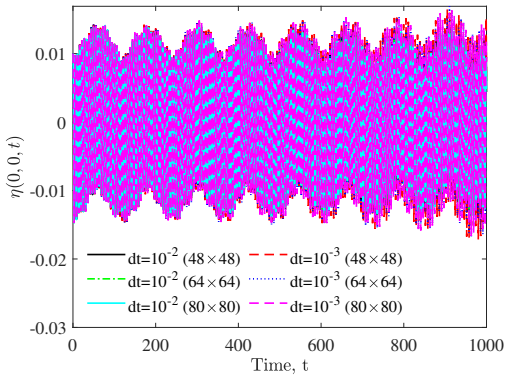

(a) Interface centred at $z = 0$

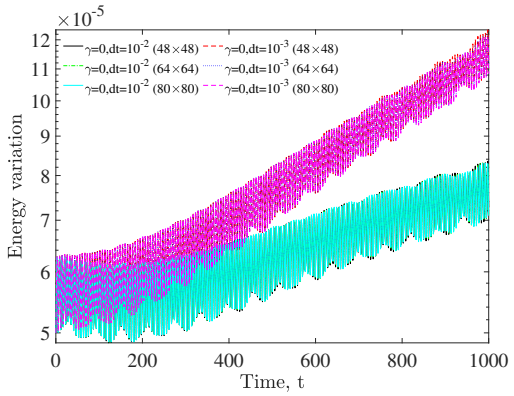

(b) Energy variation for an interface centred at $z = 0$

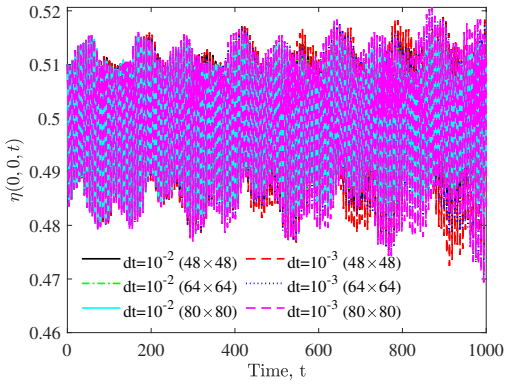

(c) Interface centred at $z = 0.5$

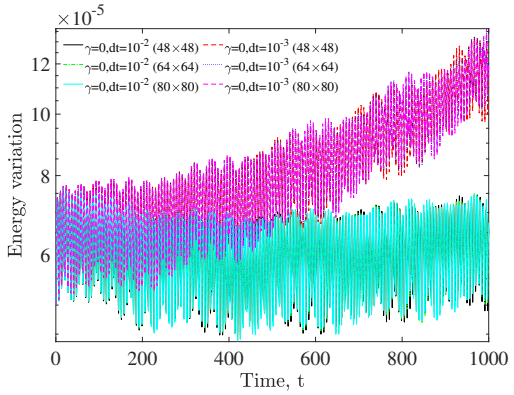

(d) Energy variation for an interface centred at $z = 0.5$

FIGURE 7.11: The evolution of the interfacial amplitude and energy variation for $\beta = .5$ of a rectangular cell of aspect ratio $L_x/L_y = 2$ for a $(1, 0)$ gravity mode with an initial amplitude of $A = 0.01$.

In a rectangular cell with layers of equal thickness, a significantly higher, compared to the square cell, electromagnetic parameter is permitted. In figure 7.12a the duration of the simulation prior to the break down is longer than figure 7.7a while the electromagnetic parameter is set to $\beta = 0.9$ as opposed to 0.075. The effect of numerical dissipation, discussed in the preceding paragraphs, is clearly demonstrated throughout figure 7.12 where a coarser discretisation results in longer simulation times. The results plotted in figure 7.12c does not provide definite answer in regards to the separation of the top and bottom momenta but in view of figure 7.12d the shear velocity is seen to increase, thus leading to the development of short-wave shear instability. Similarly to figure 7.10, figure 7.12e, demonstrates an initially slowly increasing energy variation which for $\gamma = 0$ eventually explodes.

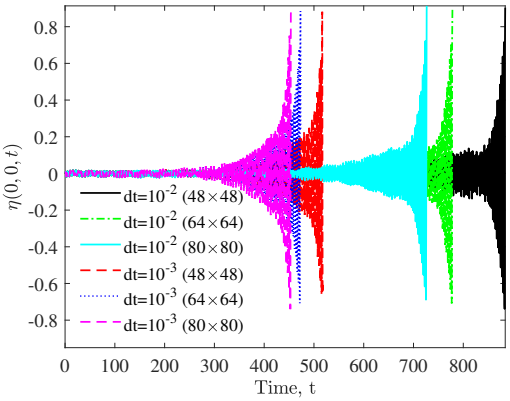

(a) Interface height

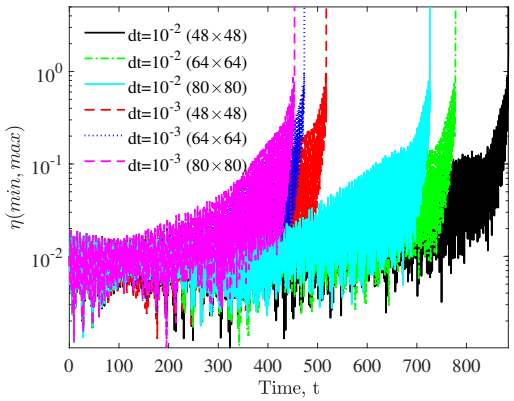

(b) The extrema of height

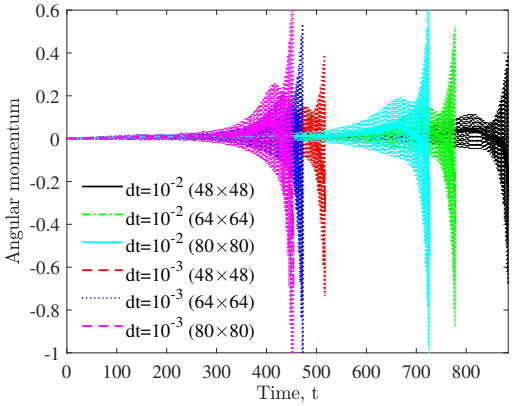

(c) Angular momentum

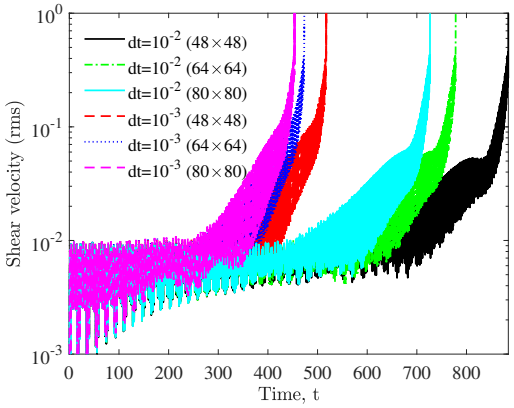

(d) Shear velocity

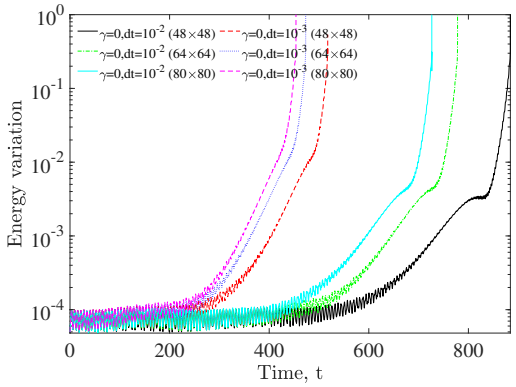

(e) Energy variation

FIGURE 7.12: The MHD problem with $\beta = 0.9$, the interface centred at $z = 0$ and an initial amplitude of $A = 0.01$ for a rectangular cell of aspect ratio $Lx/Ly = 2$.

Note that, unlike to the results for a square cell plotted in figure 7.8, in a rectangular cell of aspect ratio $L_x/L_y = 2$ with unequal layer depths, the simulation breaks down much sooner due to a rapid increase of the interfacial amplitude as shown in figure 7.13a. The angular momentum of the lower layer, shown in figure 7.13c, is larger than the one of the upper layer which appears to oscillate about zero, and thus induces an increase of the shear velocity as it may be seen in

figure 7.13d. Consequently, an instability arises in early stages of the simulation resulting into an exponential increase of energy as shown in figure 7.13.

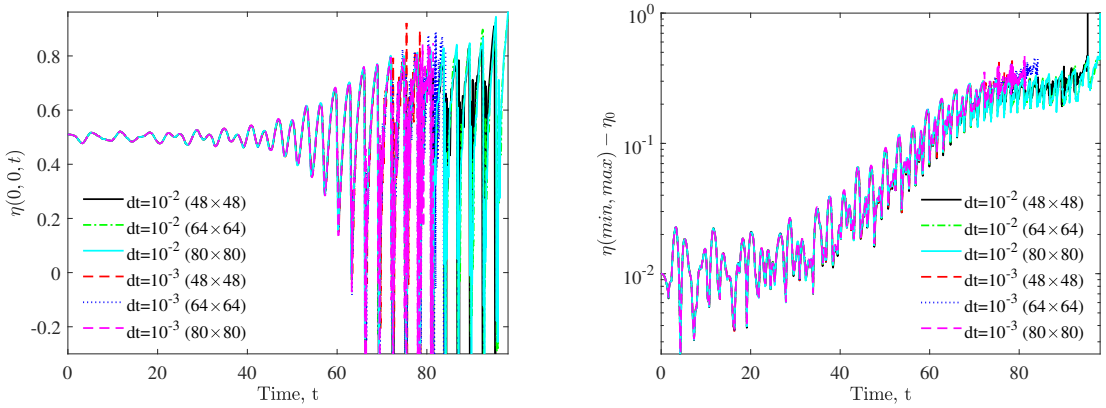

(a) Interface height

(b) The extrema of height

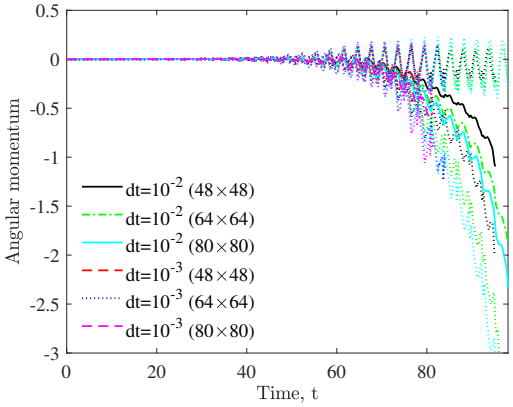

(c) Angular momentum

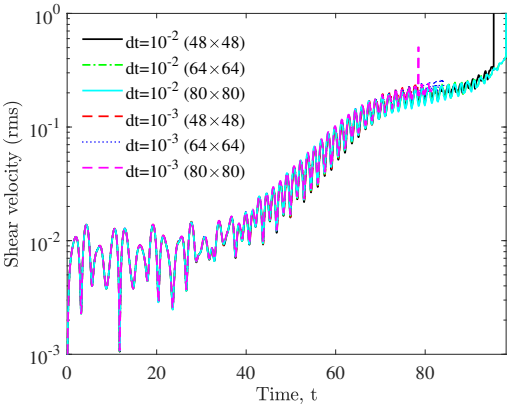

(d) Shear velocity

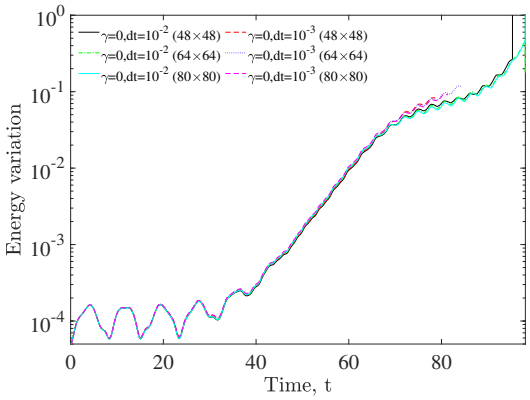

(e) Energy variation

FIGURE 7.13: The MHD problem with $\beta = 0.9$, the interface centred at $z = 0.5$ and an initial amplitude of $A = 0.01$ for a rectangular cell of aspect ratio $Lx/Ly = 2$.

Conclusions and further work

This thesis is concerned with the numerical modelling of large-amplitude interfacial waves produced by metal pad roll instability in the aluminium reduction cells. This system was studied with the use of the two-layer rigid-lid model, for conducting fluid layers under the influence of a uniform magnetic field. The semi-conservative 2D shallow-water model derived in §2.7 includes a novel fully nonlinear equation for the electric potential, derived in §5. The approximation of small density variation between the fluids permitted the exact 1D solution of the equations and a straightforward implementation of the 2D scheme and algorithms. The commonly encountered linear damping term, discussed in §2.7.4, was utilised in the investigation of both the linear stability analysis, in §6, as well as the numerical implementation of the 2D MHD shallow-water equations in §7.3, and it is shown to adequately stabilise the system.

The method of characteristics was used to obtain a novel exact solution of the two-layer lock-exchange problem where the initially piecewise interface height is released and the slightly heavier fluid is driven into the slightly lighter one. The results obtained show four different interface shapes dependent on the initial interface height. The suitability of the 1D Lax-Wendroff scheme in the presence of discontinuities was verified via the numerical solution of the lock-exchange problem, for the previously mentioned interface shapes, with a good agreement in the results.

The validation of the Lax-Wendroff scheme for discontinuous flows motivated the extension of the scheme to 2D. Furthermore, a new scheme was developed based on the 2D Richtmyer-Lax-Wendroff scheme by consideration of the finite volume formulation on a set of staggered rhombic grids. This scheme was then coupled with the newly developed and efficient fast Poisson solver which utilises a combination of the discrete cosine transforms and the tridiagonal matrix Thomas algorithm for the solution of the interface pressure and electric potential. The performance of the newly developed 2D scheme coupled with the DCT-TDMA algorithm, was benchmarked with reference to the purely hydrodynamic 1D two-layer model for smooth initial data.

The linear stability analysis of the magnetohydrodynamic system under the influence of an external uniformly vertical magnetic field for the half-plane and the finite width channel geometries was revisited in §6. This was followed by the analysis of the rectangular geometry laterally bounded by four walls. This analysis revealed the instability threshold dependence on the aspect ratio of the cell. These new analytic results were obtained using an eigenvalue perturbation method and verified by numerical solution of the linear stability problem, where the aspect ratios for which the cells become unstable at arbitrary weak electromagnetic effect, were found to be equal to the ratio of two odd numbers.

The nonlinear evolution of electromagnetic interfacial-wave instability was numerically investigated in §7.3 for the square cell which is inherently unstable. The interface positions considered were that of equal thickness layers as well as the case where their thickness ratio is $1:3$. The numerical results obtained from the 2D two-layer shallow-water model at initial times were in excellent agreement with the growth rates predicted by the linear stability analysis. Furthermore, it was shown that the nonlinear effects result in the slowdown of the growth of large-amplitude waves leading to a quasi-equilibrium state in certain cases. However, it was found that the rotating interfacial wave by the nonlinear streaming effect induces a global counter-circulation in the top and bottom layers, whereby exceeding a critical value of the shear velocity leads to the Kelvin-Helmholtz-type instability which causes the interface to break down.

The models and algorithms designed and utilised in this work employed a series of simplifications in order to reduce the complexity in the problem. In order to model aluminium reduction cells in a more realistic framework, extensions may be required in terms of the perturbation of the electric field induced by the flow across the magnetic field. Furthermore, a more realistic model of the problem could be constructed by considering non-uniform magnetic fields, known to be present in aluminium reduction cells Bojarevics and Romerio (1994).

Although effects of linear friction were briefly considered in terms of a linear friction term, incorporation of more refined viscous terms similarly to Zikanov (2018) or turbulent stresses could potentially enable a more adequate modelling of the viscous effects. Furthermore, the hydrodynamic analysis and numerical investigation of magnetohydrodynamic instabilities beyond the Boussinesq approximation pose an interesting aspect of the problem being natural extensions of the present work. Additionally, the thickness of the respective layers should be further investigated as it has a critical role on the stability of a cell. In future work, the discussed reduction of simplifications presently made, could enable

verification against real data of aluminium reduction cells.

Bibliography

Abbott, M. B. (1961). 'On the spreading of one fluid over another'. In: *La Houille Blanche* 6, pp. 827–856 (cit. on p. 10).

Abgrall, R. and S. Karni (2009). 'Two-layer shallow water system: a relaxation approach'. In: *SIAM Journal on Scientific Computing* 31.3, pp. 1603–1627 (cit. on p. 10).

Ahmed, N., T. Natarajan and K. R. Rao (1974). 'Discrete cosine transform'. In: *IEEE transactions on Computers* 100.1, pp. 90–93 (cit. on p. 44).

Armi, L. (1986). 'The hydraulics of two flowing layers with different densities'. In: *Journal of Fluid Mechanics* 163, pp. 27–58 (cit. on p. 10).

Audusse, E. (2005). 'A multilayer Saint-Venant model: derivation and numerical validation'. In: *Discrete & Continuous Dynamical Systems-B* 5.2, p. 189 (cit. on p. 29).

Baines, P. (1995). *Topographic effects in stratified flows*. Cambridge University Press (cit. on pp. 10, 57).

Baines, P. G. (1984). 'A unified description of two-layer flow over topography'. In: *Journal of Fluid Mechanics* 146, pp. 127–167 (cit. on p. 52).

Barré de Saint-Venant, A. (1871). 'Théorie et équations générales du mouvement non permanent des eaux courantes'. In: *Comptes Rendus des séances de l'Académie des Sciences, Paris, France, Séance* 17.73, pp. 147–154 (cit. on p. 9).

Barros, R. (2006). 'Conservation laws for one-dimensional shallow water models for one and two-layer flows'. In: *Mathematical Models and Methods in Applied Sciences* 16.01, pp. 119–137 (cit. on p. 10).

Batchelor, G. (2000). *An Introduction to Fluid Dynamics*. Cambridge University Press (cit. on p. 53).

Batchelor, G., H. K. Moffatt and M. Worster (2000). *Perspectives in fluid dynamics: a collective introduction to current research*. Cambridge University Press (cit. on p. 1).

Benjamin, T. (1968). 'Gravity currents and related phenomena'. In: *Journal of Fluid Mechanics* 31.2, pp. 209–248 (cit. on p. 11).

Benney, D. (2006). 'Conservation laws associated with long surface waves'. In: *J. Comput. Appl. Math.* 190.1-2, pp. 136–141 (cit. on p. 10).

Bojarevics, V. (1998). 'Nonlinear waves with electromagnetic interaction in aluminum electrolysis cells'. In: *Progress in Astronautics and Aeronautics* 182, pp. 833–848 (cit. on pp. 7, 29, 71).

Bojarevics, V. and K. Pericleous (2008). 'Shallow water model for aluminium electrolysis cells with variable top and bottom'. In: *Light Metals*. Vol. 2008. TMS, p. 403 (cit. on pp. 2, 29).

Bojarevics, V. and M. V. Romerio (1994). 'Long wave instability of liquid metal-electrolyte interface in aluminum electrolysis cells: a generalization of Sele's criterion'. In: *European Journal of Mechanics - B/Fluids* 13, p. 33 (cit. on pp. 2, 7, 9, 27, 72, 108).

Boris, J. P. and D. L. Book (1973). 'Flux-corrected transport. I. SHASTA, a fluid transport algorithm that works'. In: *Journal of computational physics* 11.1, pp. 38–69 (cit. on p. 13).

— (1976). 'Solution of continuity equations by the method of flux-corrected transport'. In: *Controlled Fusion*, pp. 85–129 (cit. on p. 13).

Boyd, J. P. (2013). *Chebyshev and Fourier Spectral Methods: Second Revised Edition*. New York: Dover Publications. ISBN: 9780486141923 (cit. on p. 87).

Burstein, S. Z. (1967). 'High Order Accurate Difference Methods in Hydrodynamics††Work supported by U.S. Atomic Energy Commission under Contract No. AT (30–l)–1480.' In: *Nonlinear Partial Differential Equations*. Ed. by A. W.F. Academic Press, pp. 279–290. ISBN: 978-1-4831-9647-3 (cit. on p. 41).

Cavanie, A. (1969). 'On the genesis and propagation of internal waves in a two-layered medium'. In: *Oceanographic Papers* 9, pp. 831–843 (cit. on p. 57).

Chakravarthy, S. and S. Osher (1983). 'High resolution applications of the Osher upwind scheme for the Euler equations'. In: *6th Computational Fluid Dynamics Conference Danvers*, p. 1943 (cit. on p. 13).

Chorin, A. J. (1968). 'Numerical solution of the Navier-Stokes equations'. In: *Mathematics of computation* 22.104, pp. 745–762 (cit. on p. 42).

Courant, R. and K. O. Friedrichs (1948). *Supersonic flow and shock waves*. Interscience (cit. on p. 9).

Davidson, P. (2001). *An Introduction to Magnetohydrodynamics*. Cambridge Texts in Applied Mathematics. Cambridge University Press (cit. on pp. 1, 21).

Davidson, P. and R. Lindsay (1998). 'Stability of interfacial waves in aluminium reduction cells'. In: *Journal of Fluid Mechanics* 362, pp. 273–295 (cit. on pp. 7–9, 28, 79).

Davidson, P. (2000). 'Overview Overcoming instabilities in aluminium reduction cells: a route to cheaper aluminium'. In: *Materials science and technology* 16.5, pp. 475–479 (cit. on p. 1).

Debnath, L. (2011). *Nonlinear partial differential equations for scientists and engineers*. Springer Science & Business Media (cit. on p. 59).

Dong, S. and J. Shen (2012). 'A time-stepping scheme involving constant coefficient matrices for phase-field simulations of two-phase incompressible flows with large density ratios'. In: *Journal of Computational Physics* 231.17, pp. 5788–5804 (cit. on p. 43).

Durran, D. R. (2010). *Numerical methods for fluid dynamics: With applications to geophysics*. Vol. 32. Springer Science & Business Media (cit. on p. 34).

Eilon, B., D. Gottlieb and G. Zwas (1972). 'Numerical stabilizers and computing time for second-order accurate schemes'. In: *Journal of computational Physics* 9.3, pp. 387–397 (cit. on p. 41).

Engquist, B. and S. Osher (1981). 'One-sided difference approximations for nonlinear conservation laws'. In: *Mathematics of Computation* 36.154, pp. 321–351 (cit. on p. 13).

Esler, J. and J. Pearce (2011). 'Dispersive dam-break and lock-exchange flows in a two-layer fluid'. In: *Journal of Fluid Mechanics* 667, pp. 555–585 (cit. on pp. 12, 57, 68).

Gerbeau, J.-F., C. Le Bris and T. Lelièvre (2006). *Mathematical methods for the magnetohydrodynamics of liquid metals*. Clarendon Press (cit. on pp. 18, 20, 22, 28).

Gerbeau, J.-F. and B. Perthame (2001). 'Derivation of Viscous Saint-Venant System for Laminar Shallow Water; Numerical Validation'. In: *Discrete and Continuous Dynamical Systems-Series B* 1.1, pp. 89–102 (cit. on p. 29).

Gill, A. E. (1983). *Atmosphere—ocean dynamics*. Elsevier (cit. on p. 24).

Godlewski, E. and P.-A. Raviart (2013). *Numerical approximation of hyperbolic systems of conservation laws*. Vol. 118. Springer Science & Business Media (cit. on p. 30).

Godunov, S. K. (1959). 'A difference scheme for numerical solution of discontinuous solution of hydrodynamic equations'. Trans. by J. 7. (US Joint Publ. Res. Service. In: *Matematicheskii Sbornik* 47, pp. 271–306 (cit. on p. 12).

Grjotheim, K. and H. Kvande (1993). *Introduction to aluminium electrolysis*. Aluminium-Verlag (cit. on pp. 1, 20).

Harten, A. (1983). 'High resolution schemes for hyperbolic conservation laws'. In: *Journal of computational physics* 49.3, pp. 357–393 (cit. on pp. 12, 13, 34).

— (1984). 'On a class of high resolution total-variation-stable finite-difference schemes'. In: *SIAM Journal on Numerical Analysis* 21.1, pp. 1–23 (cit. on p. 12).

Harten, A. and S. Osher (1987). 'Uniformly high-order accurate non-oscillatory schemes. I'. In: *SIAM Journal on Numerical Analysis* 24.2, pp. 279–309 (cit. on p. 13).

Hasbestan, J. J. and I. Senocak (Nov. 2018). 'PittPack: Open-Source FFT-Based Poisson's Equation Solver for Computing With Accelerators'. In: vol. Volume 7: Fluids Engineering. ASME International Mechanical Engineering Congress and Exposition, V007T09A021. DOI: 10.1115/IMECE2018-87697. eprint: https://asmedigitalcollection.asme.org/IMECE/proceedings-pdf/IMECE2018/52101/V007T09A021/2504543/v007t09a021-imece2018-87697.pdf. URL: https://doi.org/10.1115/IMECE2018-87697 (cit. on p. 46).

— (Sept. 2019). 'PittPack: An Open-Source Poisson's Equation Solver for Extreme-Scale Computing with Accelerators'. In: *arXiv e-prints*. arXiv: 1909.05423 [physics.comp-ph] (cit. on pp. 46, 47).

Herreman, W. et al. (2019). 'Perturbation theory for metal pad roll instability in cylindrical reduction cells'. In: *Journal of Fluid Mechanics* 878, pp. 598–646 (cit. on p. 2).

Hesthaven, J. S. (2017). *Numerical methods for conservation laws: From analysis to algorithms*. SIAM (cit. on p. 35).

Hinch, E. J. (1991). *Perturbation Methods*. Cambridge University Press (cit. on p. 84).

Hirsch, C. (2007). *Numerical computation of internal and external flows: The fundamentals of computational fluid dynamics*. Elsevier (cit. on pp. 13, 14).

Horstmann, G. M., N. Weber and T. Weier (2018). 'Coupling and stability of interfacial waves in liquid metal batteries'. In: *Journal of Fluid Mechanics* 845, pp. 1–35 (cit. on p. 2).

Hou, T. Y. and P. G. LeFloch (1994). 'Why nonconservative schemes converge to wrong solutions: error analysis'. In: *Mathematics of computation* 62.206, pp. 497–530 (cit. on p. 32).

Huppert, H. E. and J. E. Simpson (1980). 'The slumping of gravity currents'. In: *J. Fluid Mech.* 99.4, pp. 785–799 (cit. on p. 11).

Johnson, R. S. (1997). *A modern introduction to the mathematical theory of water waves*. Vol. 19. Cambridge university press (cit. on p. 24).

Keller, J. J. and Y.-P. Chyou (1991). 'On the hydraulic lock-exchange problem'. In: *Zeitschrift für Angewandte Mathematik und Physik* 42.6, pp. 874–910 (cit. on p. 11).

Keulegan, G. (1957). 'An experimental study of the motion of saline water from locks into fresh water channels'. In: *Nat. Bur. Stand. Rept. Technical Report* 5168 (cit. on pp. 10, 11).

Klemp, J., R. Rotunno and W. Skamarock (1994). 'On the dynamics of gravity currents in a channel'. In: *Journal of Fluid Mechanics* 269, pp. 169–198 (cit. on pp. 10–12).

— (1997). 'On the propagation of internal bores'. In: *Journal of Fluid Mechanics* 331, pp. 81–106 (cit. on p. 11).

Kurenkov, A. et al. (2004). 'Stability of aluminum reduction cells with mean flow'. In: *Magnetohydrodynamics* 40.2, pp. 203–212 (cit. on p. 8).

Lax, P. and B. Wendroff (1960). 'Systems of conservation laws'. In: *Communications on Pure and Applied mathematics* 13.2, pp. 217–237 (cit. on pp. 13, 32).

Lax, P. D. (1954). 'Weak solutions of nonlinear hyperbolic equations and their numerical computation'. In: *Communications on pure and applied mathematics* 7.1, pp. 159–193 (cit. on p. 14).

Lerat, A. and R. Peyret (1974). 'Noncentered schemes and schock propagation problems'. In: *Computers and Fluids* 2.1, pp. 35–52 (cit. on p. 68).

LeVeque, R. (2002) (cit. on pp. 10, 13, 14, 34, 35).

Liska, R. and B. Wendroff (1998). 'Composite schemes for conservation laws'. In: *SIAM Journal on Numerical Analysis* 35.6, pp. 2250–2271 (cit. on p. 69).

Long, R. R. (1954). 'Some aspects of the flow of stratified fluids: II. Experiments with a two-fluid system'. In: *Tellus* 6.2, pp. 97–115 (cit. on p. 10).

— (1956a). 'Long waves in a two-fluid system'. In: *Journal of Meteorology* 13.1, pp. 70–74 (cit. on pp. 10, 11).

— (1956b). 'Solitary Waves in the One-and Two-Fluid Systems'. In: *Tellus* 8.4, pp. 460–471 (cit. on pp. 52, 57).

Lowe, R. J., J. W. Rottman and P. F. Linden (2005). 'The non-Boussinesq lock-exchange problem. Part 1. Theory and experiments'. In: *J. Fluid Mech.* 537, pp. 101–124 (cit. on p. 11).

Lukyanov, A., G. El and S. Molokov (2001). 'Instability of MHD-modified interfacial gravity waves revisited'. In: *Physics Letters A* 290.3-4, pp. 165–172 (cit. on pp. 2, 8, 77, 78).

Lympany, S., J. Evans and R. Moreau (1982). 'Magnetohydrodynamic effects in aluminium reduction cells'. In: *Metallurgical Applications of Magnetohydrodynamics, Proceedings of a Symposium of the International Union of the Theoretical and Applied Mechanics, Cambridge, UK*, pp. 6–10 (cit. on pp. 6, 29).

MacCormack, R. (1969). 'The Effect of Viscosity in Hypervelocity Impact Cratering'. In: *AIAA Paper* 69.354 (cit. on p. 13).

Marche, F. (2007). 'Derivation of a new two-dimensional viscous shallow water model with varying topography, bottom friction and capillary effects'. In: *European Journal of Mechanics-B/Fluids* 26.1, pp. 49–63 (cit. on p. 29).

Maxwell, J. C. (1861). 'On physical lines of force'. In: *The London, Edinburgh, and Dublin Philosophical Magazine and Journal of Science* 21.141, pp. 338–348 (cit. on p. 17).

— (1865). 'A dynamical theory of the electromagnetic field'. In: *Philosophical transactions of the Royal Society of London* 155, pp. 459–512 (cit. on p. 17).

Milewski, P. (2004). 'Nonlinear stability of two-layer flows'. In: *Communications in Mathematical Sciences* 2.3, pp. 427–442 (cit. on p. 52).

Milewski, P. and E. Tabak (2015). 'Conservation law modelling of entrainment in layered hydrostatic flows'. In: *Journal of Fluid Mechanics* 772, pp. 272–294 (cit. on pp. 12, 56, 57).

Miura, R. (1974). 'Conservation laws for the fully nonlinear long wave equations'. In: *Studies in Applied Mathematics* 53.1, pp. 45–56 (cit. on p. 10).

Molokov, S., G. El and A. Lukyanov (2011). 'Classification of instability modes in a model of aluminium reduction cells with a uniform magnetic field'. In: *Theoretical and Computational Fluid Dynamics* 25.5, pp. 261–279 (cit. on pp. 8, 20, 28, 78, 79).

Montgomery, P. and T. Moodie (2001). 'On the number of conserved quantities for the two-layer shallow-water equations'. In: *Studies in Applied Mathematics* 106.2, pp. 229–259 (cit. on p. 10).

Moreau, R. and J. W. Evans (1984). 'An analysis of the hydrodynamics of aluminum reduction cells'. In: *Journal of the Electrochemical Society* 131.10, pp. 2251–2259 (cit. on pp. 6, 29).

Moreau, R. and D. Ziegler (1988). 'The Moreau-Evans hydrodynamic model applied to actual Hall-Héroult cells'. In: *Metallurgical Transactions B* 19.5, pp. 737–744 (cit. on pp. 6, 7).

Moreau, R. J. (1990). *Magnetohydrodynamics*. Vol. 3. Springer Science & Business Media (cit. on pp. 18, 22).

Morris, S. and P. Davidson (2003). 'Hydromagnetic edge waves and instability in reduction cells'. In: *Journal of Fluid Mechanics* 493, pp. 121–130 (cit. on pp. 77–79, 82).

Ovsyannikov, L. (1979). 'Two-layer shallow water model'. In: *Journal of Applied Mathematics and Mechanics* 20.2, pp. 127–135 (cit. on pp. 10, 11, 57).

Pedlosky, J. (1979). *Geophysical fluid dynamics*. Springer (cit. on pp. 24, 29, 52).

Potter, D. (1973). *Computational physics*. Wiley-Interscience publication. J. Wiley. ISBN: 9780471695554 (cit. on pp. 34, 35, 38).

Press, W. H., S. A. Teukolsky, W. T. Vetterling and B. P. Flannery (2007). *Numerical recipes 3rd edition: The art of scientific computing*. Cambridge university press (cit. on p. 46).

Priede, J. (2018). 'Self-contained two-layer shallow water theory of strong internal bores'. In: *arXiv e-prints*, arXiv:1806.06041v3 (cit. on pp. 51, 53, 59).

Richtmyer, R. D. (1962). *A survey of difference methods for non-steady fluid dynamics*. Vol. 63. National Center for Atmospheric Research Boulder, Colorado (cit. on pp. 14, 32, 34, 37).

Richtmyer, R. D. and K. Morton (1967). 'Difference methods for initial-value problems'. In: (cit. on pp. 33, 34, 37, 38, 41).

Ritter, A. (1892). 'Die Fortpflanzung der Wasserwellen'. In: *Zeitschrift des Vereines Deutscher Ingenieure* 36.33, pp. 947–954 (cit. on p. 9).

Roe, P. L. (1981). 'Approximate Riemann solvers, parameter vectors, and difference schemes'. In: *Journal of computational physics* 43.2, pp. 357–372 (cit. on p. 13).

— (1985). 'Some Contributions to the Modeling of Discontinuous Flows'. In: *Proceedings of 1985 AMS-SIAM Summer Seminar on Large Scale Computing in Fluid Mechanics, Lectures in Applied Mathematics* 22, pp. 143–193 (cit. on p. 13).

— (1986). 'Characteristic-based schemes for the Euler equations'. In: *Annual review of fluid mechanics* 18.1, pp. 337–365 (cit. on p. 13).

Rottman, J. W. and J. E. Simpson (1983). 'Gravity currents produced by instantaneous releases of a heavy fluid in a rectangular channel'. In: *Journal of Fluid Mechanics* 135, pp. 95–110 (cit. on pp. 11, 12).

Salmon, R. (1998). *Lectures on geophysical fluid dynamics*. Oxford University Press (cit. on p. 24).

Sandstrom, H. and C. Quon (1993). 'On time-dependent, two-layer flow over topography. I. Hydrostatic approximation'. In: *Fluid dynamics research* 11.3, pp. 119–137 (cit. on pp. 52, 57).

Sele, T. (1977). 'Instabilities of the metal surface in electrolytic cells'. In: *Paper from Light Metals 1977*. 1 (cit. on pp. 5, 7, 8, 28).

Sharma, V. (2010). *Quasilinear hyperbolic systems, compressible flows, and waves*. CRC Press (cit. on p. 59).

Shin, J., S. Dalziel and P. Linden (2004). 'Gravity currents produced by lock exchange'. In: *Journal of Fluid Mechanics* 521, pp. 1–34 (cit. on pp. 10, 11).

Simpson, J. E. and R. E. Britter (1979). 'The dynamics of the head of a gravity current advancing over a horizontal surface'. In: *J. Fluid Mech.* 94.3, pp. 477–495 (cit. on p. 10).

Sneyd, A. (1992). 'Interfacial instabilities in aluminium reduction cells'. In: *Journal of Fluid Mechanics* 236, pp. 111–126 (cit. on p. 6).

Sneyd, A. and A. Wang (1994). 'Interfacial instability due to MHD mode coupling in aluminium reduction cells'. In: *Journal of Fluid Mechanics* 263, pp. 343–360 (cit. on pp. 2, 7–9, 87).

Sneyd, A. D. (1985). 'Stability of fluid layers carrying a normal electric current'. In: *Journal of Fluid Mechanics* 156, pp. 223–236 (cit. on pp. 6, 7).

Stewart, A. L. and P. J. Dellar (2013). 'Multilayer shallow water equations with complete coriolis force. part 3. hyperbolicity and stability under shear'. In: *Journal of Fluid Mechanics* 723, pp. 289–317 (cit. on p. 99).

Stoker, J. J. (1957). 'Water waves: the mathematical theory with applications'. In: (cit. on pp. 9, 10, 59).

Sun, H., O. Zikanov and D. P. Ziegler (2004). 'Non-linear two-dimensional model of melt flows and interface instability in aluminum reduction cells'. In: *Fluid Dynamics Research* 35.4, p. 255 (cit. on pp. 2, 9).

Swarztrauber, P. N. (1977). 'The methods of cyclic reduction, Fourier analysis and the FACR algorithm for the discrete solution of Poisson's equation on a rectangle'. In: *Siam Review* 19.3, pp. 490–501 (cit. on p. 46).

— (1986). 'Symmetric FFTs'. In: *Mathematics of Computation* 47.175, pp. 323–346 (cit. on p. 46).

Tan, W. Y. (1992). *Shallow water hydrodynamics: Mathematical theory and numerical solution for a two-dimensional system of shallow-water equations*. Vol. 55. Elsevier (cit. on pp. 24, 29).

Thomas, L. H. (1949). 'Elliptic problems in linear difference equations over a network'. In: *Watson scientific computing laboratory, Columbia University, New York* 1 (cit. on p. 45).

Toro, E. F. (2001). *Shock-capturing methods for free-surface shallow flows*. John Wiley (cit. on pp. 34, 35).

Ungarish, M. (2009). *An introduction to gravity currents and intrusions*. CRC Press (cit. on p. 12).

Urata, N. (1985). 'Magnetics and metal pad instability'. In: *Light Metals* (cit. on pp. 7, 8).

Vallis, G. K. (2017). *Atmospheric and oceanic fluid dynamics*. Cambridge University Press (cit. on p. 24).

Van Leer, B. (1973). 'Towards the ultimate conservative difference scheme I. The quest of monotonicity'. In: *Proceedings of the Third International Conference on Numerical Methods in Fluid Mechanics*. Springer, pp. 163–168 (cit. on p. 13).

— (1974). 'Towards the ultimate conservative difference scheme. II. Monotonicity and conservation combined in a second-order scheme'. In: *Journal of computational physics* 14.4, pp. 361–370 (cit. on p. 13).

— (1977). 'Towards the ultimate conservative difference scheme. IV. A new approach to numerical convection'. In: *Journal of computational physics* 23.3, pp. 276–299 (cit. on p. 13).

— (1979). 'Towards the ultimate conservative difference scheme. V. A second-order sequel to Godunov's method'. In: *Journal of computational Physics* 32.1, pp. 101–136 (cit. on p. 13).

Vesely, F. J. (2001). *Computational Physics*. Springer (cit. on pp. 34, 38).

Vreugdenhil, C. B. (1994). *Numerical methods for shallow-water flow*. Vol. 13. Springer Science & Business Media (cit. on p. 24).

Weber, N. et al. (2017). 'Metal pad role instability in liquid metal batteries'. In: *Magnetohydrodynamics* 53.1, pp. 3–13 (cit. on p. 2).

Weier, T. et al. (2017). 'Liquid metal batteries-materials selection and fluid dynamics'. In: *IOP Conference Series: Materials Science and Engineering*. Vol. 228. 1. IOP Publishing, p. 012013 (cit. on p. 2).

Whitham, G. (1975). *Linear and nonlinear waves*. Modern Book Incorporated (cit. on pp. 9, 10, 12, 58, 59).

Wilhelmson, R. B. and J. H. Ericksen (1977). 'Direct solutions for Poisson's equation in three dimensions'. In: *Journal of Computational Physics* 25.4, pp. 319–331. ISSN: 0021-9991. DOI: https://doi.org/10.1016/0021-9991(77)90001-8. URL: http://www.sciencedirect.com/science/article/pii/0021999177900018 (cit. on p. 46).

Wilson, J. (1972). 'Stability of Richtmyer type difference schemes in any finite number of space variables and their comparison with multistep Strang schemes'. In: *IMA Journal of Applied Mathematics* 10.2, pp. 238–257 (cit. on p. 41).

Wood, I. and J. Simpson (1984). 'Jumps in layered miscible fluids'. In: *Journal of Fluid Mechanics* 140, pp. 329–342 (cit. on pp. 11, 52).

Yih, C.-S. (1947). 'A study of the characteristics of gravity waves at a liquid interface'. In: (cit. on p. 10).

— (1965). *Dynamics of Nonhomogeneous fluids*. Macmillan (cit. on pp. 10, 11).

Yih, C.-S. and C. Guha (1955). 'Hydraulic jump in a fluid system of two layers'. In: *Tellus* 7.3, pp. 358–366 (cit. on p. 11).

Zhang, D., C. Jiang, D. Liang and L. Cheng (2015). 'A review on TVD schemes and a refined flux-limiter for steady-state calculations'. In: *Journal of Computational Physics* 302, pp. 114–154 (cit. on p. 35).

Zikanov, O. (2018). 'Shallow water modeling of rolling pad instability in liquid metal batteries'. In: *Theoretical and Computational Fluid Dynamics* 32.3, pp. 325–347 (cit. on p. 108).

Zikanov, O., A. Thess, P. Davidson and D. P. Ziegler (2000). 'A new approach to numerical simulation of melt flows and interface instability in Hall-Heroult cells'. In: *Metallurgical and Materials Transactions B* 31.6, pp. 1541–1550 (cit. on pp. 2, 8, 9, 29, 71).

Zwas, G. (1972). 'On two step Lax-Wendroff methods in several dimensions'. In: *Numerische Mathematik* 20.5, pp. 350–355 (cit. on p. 41).

Appendix A

Algorithms

A.1 Thomas algorithm

Algorithm 1 The Thomas Type-I algorithm factorisation and solver

Comment: Factorization of the tridiagonal matrix: [1-d,1; 1,-d,1; ...; 1,1-d]
Input: n (vector size), a (reserved matrix), d (main diagonal element)
Output: a (Thomas algorithm factors)

```
1: function TDFCT1(n, a, d)
2:     if d == 2 then                                  ▷ Singular case
3:         a(1 : n) = 1
4:     else
5:         a(1) = 1/(d − 1)
6:         for i = 2 to n − 1 do
7:             a(i) = 1/(d − a(i − 1))
8:         end for
9:         a(n) = 1/(a(n − 1) − (d − 1))
10:    end if
11: end function
```

Comment: Solution using the factorised matrix a(n) to solve f(1, n)
Input: n (vector size), a (Thomas algorithm factors), f (Poisson RHS)
Output: f (Solution)

```
1: function TDSLV1(n, a, f)
2:     for i = 1 to n − 1 do
3:         f(1, i + 1) = f(1, i + 1) + f(1, i) ∗ a(i)      ▷ Forward sweep
4:     end for
5:     f(1, n) = f(1, n) ∗ a(n)
6:     for i = n − 1 to 1 do
7:         f(1, i) = (f(1, i + 1) − f(1, i)) ∗ a(i)        ▷ Backward sweep
8:     end for
9: end function
```

Algorithm 2 The Thomas Type-II algorithm factorisation and solver

Comment: Factorization of the tridiagonal matrix: [-d,2; 1,-d,1; ...; 2,-d]
Input: n (vector size), a (reserved matrix), d (main diagonal element)
Output: a (Thomas algorithm factors)

function TDFCT2(n, a, d)
  if $d == 2$ **then** ▷ Singular case
    $a(1 : n+1) = 1$
  else
    $a(1) = 2/d$
    for $i = 2$ to n **do**
      $a(i) = 1/(d - a(i-1))$
    end for
    $a(n) = 1/(a(n-1) - d/2))$
  end if
end function

Comment: Solution using the factorised matrix a(n+1) to solve f(1, n+1)
Input: n (vector size), a (Thomas algorithm factors), f (Poisson RHS)
Output: f (Solution)

function TDSLV2(n, a, f)
  for $i = 1$ to n **do**
    $f(1, i+1) = f(1, i+1) + f(1, i) * a(i)$ ▷ Forward sweep
  end for
  $f(1, n+1) = f(1, n+1) * a(n+1)$
  for $i = n$ to 1 **do**
    $f(1, i) = (f(1, i+1) - f(1, i)) * a(i)$ ▷ Bacward sweep
  end for
end function

Algorithm 3 The tridiagonal system coefficients for GRID-0 & GRID-1

Comment: Factorization of the tridiagonal matrix: [1-d,1; 1,-d,1; ...; 1,1-d]
Input: nx (Matrix rows), ny (Matrix columns), dx, dy (Spatial discretisation)
Output: CF (Thomas algorithm coefficients)

for $i = 0$ to nx **do**
  $CF(:, i+1, 1)$ = tdfct2$(ny, CF(:, i+1, 1), 2 + 4 * (sin(pi * i/nx/2) * dy/dx)^2)$
  $CF(:, i+1, 2)$ = tdfct1$(ny, CF(:, i+1, 2), 2 + 4 * (sin(pi * i/nx/2) * dy/dx)^2)$
end for

A.2 The 2D Poisson solver

Algorithm 4 The 2D Poisson solver

Input: k (2x1 constant vector defining the switch of grids), n (2x1 vector containing the matrix dimensions), dy (spatial discr.), CF (factors), f (Reserved matrix)

Output: f (Solution)

1: **function** PSN2D(k, n, do)
2: $i = 1 : n(1) + 1 - k(1)$ ▷ Indices declaring the necessary points
3: $j = 1 : n(2) + 1 - k(2)$
4: $f(i, j) = \text{dct}(f(i, j), [], 1, 'Type', k(1) + 1)$ ▷ Apply DCT
5: **for** $it = 0$ to $n(1) - k(1)$ **do** ▷ Thomas algorithm solution
6: **if** $k(2) == 0$ **then**
7: $f(it + 1, j) = \text{tdslv0}(n(2), CF(j, it + 1, 1), f(it + 1, j))$
8: **end if**
9: **if** $k(2) == 1$ **then**
10: $f(it + 1, j) = \text{tdslv1}(n(2), CF(j, it + 1, 2), f(it + 1, j))$
11: **end if**
12: **end for**
13: $f(i, j) = \text{idct}(f(i, j), [], 1, 'Type', k(1) + 1)$ ▷ Apply inverse DCT
14: **end function**

A.3 Code structure

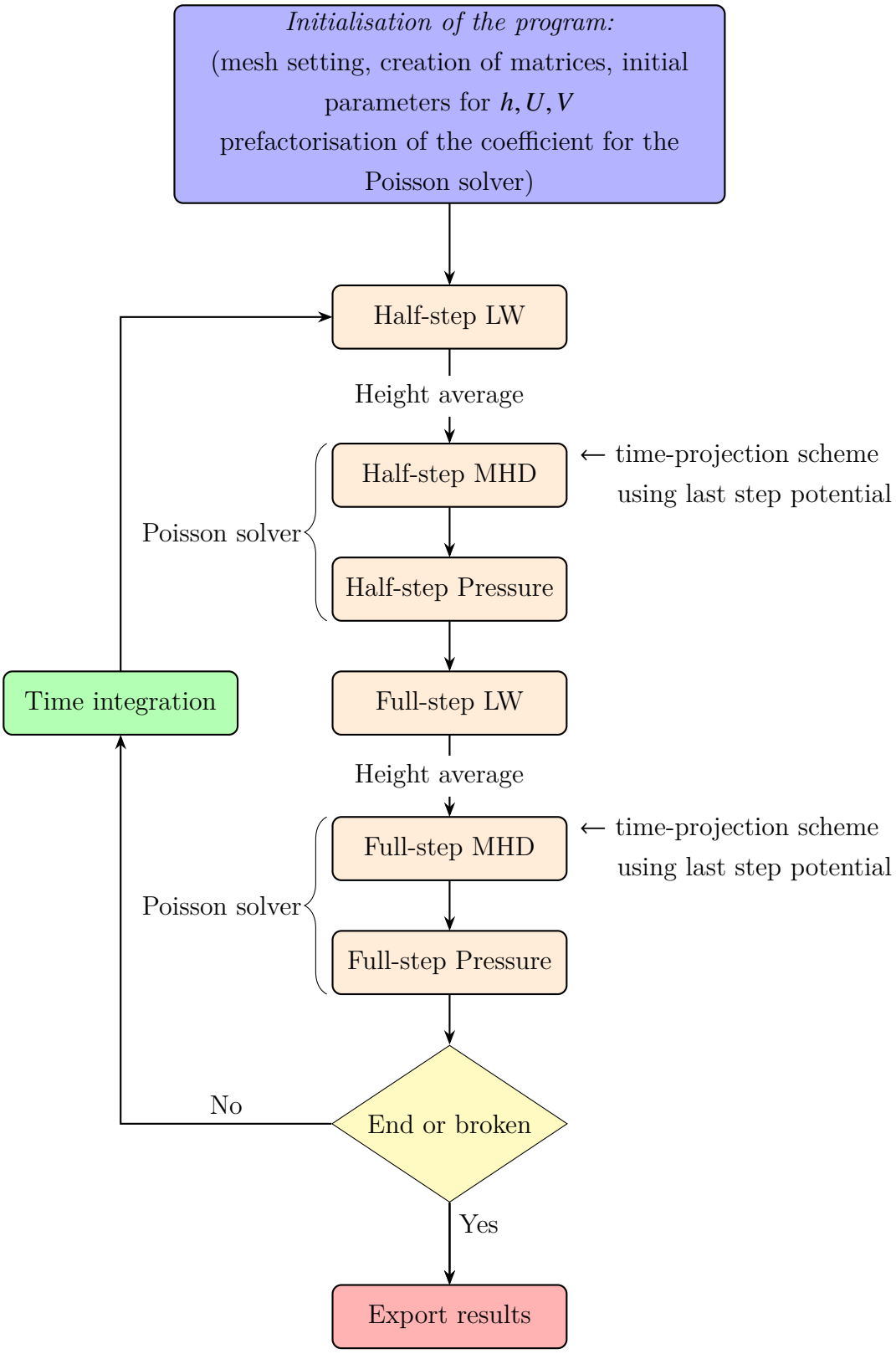

FIGURE A.1: Code logic diagram.